Numerical simulation of gas–liquid two-phase flow by a semi-Lagrangian–Lagrangian approach

Dissertation by
Van Luc Nguyen

Submitted in Partial Fulfilment of the Requirements
for the Degree of Doctor of Philosophy
in Information Science

名古屋大学
NAGOYA UNIVERSITY

Graduate School of Information Science
Nagoya University

September 2019

Abstract

Gas–liquid two-phase flows around rigid obstacles are observed widely in engineering applications, such as shell and tube heat exchangers, steam generators, and condensers. A comprehensive understanding of the phenomena of gas–liquid two-phase flows around obstacles would allow for improved design and control of related engineering devices. This has attracted the attention of many scientific and engineering researchers. In the era of digital development, numerical simulation is an effective tool for discovering knowledge about the characteristics of bubbly two-phase flow. In computational fluid dynamics, there are three different approaches that have been used to simulate the bubbly two-phase flows around obstacles, namely, Eulerian–Eulerian; Eulerian–Lagrangian; Lagrangian–Lagrangian. Here, a semi-Lagrangian–Lagrangian approach composed of a vortex-in-cell method for the liquid phase and a Lagrangian description of the gas phase was developed for the simulation of a bubbly flow around a rigid obstacle. The superior abilities of the semi-Lagrangian–Lagrangian approach to analyze the vortex structure of the flow and supply physical details of bubble dynamics were proved. Moreover, the characteristics of the bubbles and the induced-liquid flow of an annular bubble plume, the interaction between a vortex ring and a bubble plume, and the bubbly flow around a cylinder were clarified.

Acknowledgements

I would like to thank my supervisor Prof. Tomomi Uchiyama for giving me opportunities to learn, to enjoy in the field of Computational Fluid Dynamics. I wish to sincerely thank my co-examiners Prof. Takashi Watanabe and Prof. Masahiro Ohka for the precious suggestions on my dissertation.

Special thanks to my mother, who always loves, prays and encourages me. I regret that my father is not alive to share this accomplishment with me. I would to express my gratitude to brothers and sister in my family for their care and encouragements.

I would like to thank Dr. Tomohiro Degawa for professional suggestions and Dr. Kotaro Takamure for 'nice' discussions. I would also like to thank my lab members, and Vietnamese friends at Nagoya University, Tuan (Dr.), Tuan, Thuan, Truong, Son, Hung and Tung, for their contributions and encouragements. Many thanks to Priest MinhMan Hoang and Catholic Gotanjo Parish Choir for their encouragements and giving my life more enjoyable.

I wish to sincerely thank the MEXT (Monbukagakusho) program of Japanese government for the financial support through this course.

Last but not least, special thanks to HangTran for her patience, care, and companion.

In memory of my father

Contents

Chapter 1

Introduction

1.1 Literature review of numerical methods for gas–liquid two-phase flow

Gas–liquid two-phase flows are observed widely in both environmental processes and engineering applications such as fermentation devices, bubble reactors, boilers, and nuclear reactors (Milgram, 1983; Alam and Arakeri, 1993; Fraga et al., 2016; Uchiyama and Kusamichi, 2013). Comprehensive understanding of the interaction between gas phase and liquid phase is important for improving design and controlling engineering devices related to the bubbly two-phase flow phenomena. This has attracted the attention of many scientific and engineering researchers (Chen et al., 2014). In the era of digital development, numerical simulation is an effective tool for discovering knowledge about the characteristics of bubbly two-phase flow. In computational fluid dynamics, there are four different approaches that have been used to simulate the bubbly two-phase flows, namely, Eulerian–Eulerian (E–E); Eulerian–Lagrangian (E–L); Lagrangian–Lagrangian (L–L); and semi-Lagrangian–Lagrangian (semi-L–L). A literature survey on these approaches will be given.

1.1.1 Eulerian–Eulerian approach

In the E–E approach, the gas and liquid phases are treated mathematically as continuous phases that penetrate each other. Examples of investigations using this approach are Schwarz and Turner (1988), Torvik and Svendsen (1990), Socolofsky et al. (2008), Sokolichin and Eigenberger (1997, 1999), Druzhinin and Elghobashi (1998), Tabib et al. (2008), Krause et al. (2010), Elrais et al. (1992), Daniel et al. (1994), Troshko and Hassan (2001), Tabi et al. (2008), and Dhotre et al. (2013). This approach can be classified into several broad branches as two-fluid model, fluid-dynamic model and multi-phase plume integral model.

Two-fluid model

In two-fluid model, the continuity, momentum and energy equations are solved for both phases. A general form of the continuity and momentum equations for two phases is

written in the Eulerian frame as Troshko and Hassan (2001), Tabi et al. (2008), Dhotre et al. (2013)

$$\frac{\partial}{\partial t}(\rho_k \alpha_k) + \nabla \cdot (\rho_k \alpha_k \boldsymbol{u}_k) = 0 \tag{1.1}$$

$$\frac{\partial}{\partial t}(\rho_k \alpha_k \boldsymbol{u}_k) + \nabla \cdot (\rho_k \alpha_k \boldsymbol{u}_k \boldsymbol{u}_k) = -\nabla \cdot (\alpha_k \tau_k) - \alpha_k \nabla p + \alpha_k \rho_k \boldsymbol{g} + \boldsymbol{F}_{I,k} \tag{1.2}$$

where $\boldsymbol{u}$, ρ, and α are the velocity, density, and volume fraction, respectively. The subscripts $k = l, g$ indicate the liquid and gas phases, respectively. The gas volume fraction relates to the liquid volume fraction as

$$\alpha_l + \alpha_g = 1 \tag{1.3}$$

The stress tensor of the phase k is expressed as

$$\tau_k = -\mu_{eff,k}\Big(\nabla \boldsymbol{u}_k + (\nabla \boldsymbol{u}_k)^T - \frac{2}{3}\boldsymbol{I}(\nabla \boldsymbol{u}_k)\Big) \tag{1.4}$$

where effective viscosity of the liquid phase, μ_{eff}, is composed of laminar viscosity, μ_l, eddy viscosity, $\mu_{t,l}$ and turbulence viscosity induced by the bubble motion, $\mu_{BI,l}$.

$$\mu_{eff,l} = \mu_l + \mu_{t,l} + \mu_{BI,l} \tag{1.5}$$

The effective viscosity of the gas phase is calculated from that of the liquid phase as

$$\mu_{eff,g} = \frac{\rho_g}{\rho_l}\mu_{eff,l} \tag{1.6}$$

The $\mu_{BI,l}$ was proposed by Sato and Sekoguchi (1975), and it was described as

$$\mu_{BI,l} = \rho_l C_{\mu,BI} \alpha_g d_b |\boldsymbol{u}_g - \boldsymbol{u}_l| \tag{1.7}$$

The $\boldsymbol{F}_{I,k}$ in Eq. (1.2) is the momentum exchange (total inter-facial force (Tabi et al., 2008)) between two phases, and it is computed as

$$\boldsymbol{F}_{I,g} = -\boldsymbol{F}_{I,l} = \boldsymbol{F}_D + \boldsymbol{F}_L + \boldsymbol{F}_{VM} + \boldsymbol{F}_{TD} \tag{1.8}$$

where $\boldsymbol{F}_D$, $\boldsymbol{F}_L$, $\boldsymbol{F}_{VM}$, and $\boldsymbol{F}_{TD}$ are drag, lift, virtual-mass (added-mass), and turbulent dispersion forces, respectively, acting on the bubble, and they are shown as

$$\begin{cases} \boldsymbol{F}_D = \dfrac{1}{2} C_D \rho_l \left(\dfrac{\pi d_b^2}{4}\right) |\boldsymbol{u}_g - \boldsymbol{u}_l| \big(\boldsymbol{u}_g - \boldsymbol{u}_l\big) \\ \boldsymbol{F}_L = -C_L \rho_l V_b \big(\boldsymbol{u}_g - \boldsymbol{u}_l\big) \times (\nabla \times \ \boldsymbol{u}_l) \\ \boldsymbol{F}_{VM} = C_V \rho_l V_b \Big(\dfrac{D\boldsymbol{u}_l}{Dt} - \dfrac{d\boldsymbol{u}_g}{dt}\Big) \\ \boldsymbol{F}_{TD} = C_{TD} \rho_l k \nabla \epsilon_l \end{cases} \tag{1.9}$$

The force $\boldsymbol{F}_{TD}$ expresses the turbulent diffusion of the bubbles due to the effects of the vortices (Dhotre et al., 2013). The k and ϵ_l are the turbulent kinetic energy and its dissipation rate, respectively. The term $\mu_{t,l}$ in Eq. (1.5) can be obtained using $k - \epsilon$ turbulence models.

Fluid-dynamic model

In the fluid-dynamic model, the continuity and momentum equations is written in the term of the gas–liquid mixture. The dispersed phase assumed is small and the momentum of the bubble phase can be neglected (Sokolichin and Eigenberger, 1997, 1999). The conservation form of Navier–Stokes equation can be applied for the mixture and written as

$$\frac{\partial \rho}{\partial t} + \nabla \cdot (\rho \boldsymbol{u}) = 0 \tag{1.10}$$

$$\frac{\partial (\rho \boldsymbol{u})}{\partial t} + \nabla \cdot (\rho \boldsymbol{u}\boldsymbol{u}) = -\nabla p + \nabla \cdot \tau + \rho \boldsymbol{g} \tag{1.11}$$

where $\boldsymbol{u}$, ρ, and τ are velocity, density, stress tensor of gas–liquid mixture, respectively. The mixture density is computed as

$$\rho = \alpha_g \rho_g + \alpha_l \rho_l \tag{1.12}$$

The conservation mass of the gas phase under the effects of bubble-induced turbulence is described as

$$\frac{\partial (\alpha_g \rho_g)}{\partial t} + \nabla \cdot \left(\alpha_g \rho_g \boldsymbol{u}_g\right) = D_t \tag{1.13}$$

where D_t is the dispersion effects due to random fluctuations of the bubble motion. The gas velocity $\boldsymbol{u}_g$ is computed as

$$\boldsymbol{u}_g = \boldsymbol{u}_{slip} + \boldsymbol{u}_l \tag{1.14}$$

where $\boldsymbol{u}_{slip}$ is given based on the experimental investigation. The mixture velocity $\boldsymbol{u}$, the liquid velocity $\boldsymbol{u}_l$ and the gas velocity $\boldsymbol{u}_g$ have a relation as

$$\rho \boldsymbol{u} = \alpha_g \rho_g \boldsymbol{u}_g + \alpha_l \rho_l \boldsymbol{u}_l \tag{1.15}$$

Multi-phase plume integral model

Review of this model is based on the work of Socolofsky et al. (2008). In this model, the governing equation is written in the term of the entrainment flux of the flow for the inner and outer bubble plume, respectively, as

$$\frac{d(\pi u_i b_i^2)}{dz} = E_i - E_o - E_p \tag{1.16}$$

$$\frac{d(\pi u_o (b_o^2 - b_i^2)}{dz} = E_a + E_o - E_i + E_p \tag{1.17}$$

where u is continuous phase velocity; b is plume half width (b is the plume radius at vertical coordinate z, and z-axis is the plume centerline); and i, o, and a indicate the inner plume, outer plume, and ambient fluid, respectively. The general idea of model is to use the similarity assumptions and entrainment hypothesis, which converts the three-dimensional problem to a set of one-dimensional equations (Socolofsky et al., 2008). The conservation of mass and momentum fluxes of the regions of the flow, such as inner plume and outer plume, are solved separately by the different equations. However, these equations are connected together using the flow entrainment quantities,

such as turbulence induced in the inner plume transports an entrainment flux E_i into the inner plume; turbulence induced in the outer plume generates an entrainment flux E_a into the outer plume; a transport of entrainment flux E_o from the inner plume into the outer plume; the flux of flow from the inner plume that escapes to form the outer plume E_p.

The E–E approach has the advantage of low computational cost compared to the E–L, L–L and semi-L–L approaches because the momentum transport of the gas phase is calculated efficiently by solving only one vector equation (Fraga et al., 2016). However, there are some drawbacks of this approach, as mentioned by Fraga et al. (2016), and Murai and Matsumoto (2000), and they are as follows: (1) the inherent numerical diffusion of the Eulerian treatment of the bubble phase, (2) the lack of physical details of bubble dynamics such as location and velocity of individual bubbles and induced fluid-bubble interaction, and (3) the approach cannot provide the correct solution in cases where the dispersed phase does not have adequate number density and spatial continuity.

1.1.2 Eulerian–Lagrangian approach

In the E–L approach, the liquid phase is described in the Eulerian frame and treated mathematically as a continuous phase, while each bubble is calculated as a Lagrangian marker that is affected by external forces and governed by Newton's second law. A few works related to this approach are Fraga et al. (2016), Sokolichin and Eigenberger (1997, 1999), Murai and Matsumoto (2000), Johansen and Boysan (1988), Swan and Moros (1993), Caballina et al. (2003), Delnoij et al. (1997a,b, 1999), Kuo et al. (1997), Yang et al. (2002), Finn et al. (2011), Cihonski et al. (2013), and Lan and Garca (2006).

The momentum equation for the motion of an individual spherical bubble proposed by Auton et al. (1988) is expressed as

$$\rho_g V_b \frac{d\boldsymbol{u}_g}{dt} = \boldsymbol{F}_B + \boldsymbol{F}_D + \boldsymbol{F}_L + \boldsymbol{F}_{VM} + \boldsymbol{F}_P + \boldsymbol{F}_{Ba} \tag{1.18}$$

where $\boldsymbol{F}_B$, $\boldsymbol{F}_D$, $\boldsymbol{F}_L$, $\boldsymbol{F}_{VM}$, $\boldsymbol{F}_P$, and $\boldsymbol{F}_{Ba}$ are buoyancy, drag, lift, virtual-mass or added-mass, pressure gradient force, and Bassett forces, respectively. These forces are expressed as (Sridhar and Katz, 1995)

$$\begin{cases} \boldsymbol{F}_B = \left(\rho_g V_b - \rho_l V_b\right)\boldsymbol{g} \\ \boldsymbol{F}_D = \dfrac{1}{2} C_D \rho_l \left(\dfrac{\pi d_b^2}{4}\right) |\boldsymbol{u}_g - \boldsymbol{u}_l| \left(\boldsymbol{u}_g - \boldsymbol{u}_l\right) \\ \boldsymbol{F}_L = -C_L \rho_l V_b \left(\boldsymbol{u}_g - \boldsymbol{u}_l\right) \times \left(\nabla \times \ \boldsymbol{u}_l\right) \\ \boldsymbol{F}_{VM} = C_V \rho_l V_b \left(\dfrac{D\boldsymbol{u}_l}{Dt} - \dfrac{d\boldsymbol{u}_g}{dt}\right) \\ \boldsymbol{F}_P = \rho_l V_b \dfrac{D\boldsymbol{u}_l}{Dt} \\ \boldsymbol{F}_{Ba} = 6\pi \left(\dfrac{d_b}{2}\right)^2 \mu \displaystyle\int_o^t \frac{d(\boldsymbol{u}_b - \boldsymbol{u}_l)/d\tau}{\sqrt{\pi\nu(t-\tau)}} d\tau \end{cases} \tag{1.19}$$

Bassett force is considered as integrated effects of the interactions of a bubble with its own wake (Sridhar and Katz, 1995). In the case of low Reynolds number past a sphere, this force can be neglected due to small entrained bubble, i.e., a weak wake induced behind the bubble. The Lagrangian trajectory of an individual bubble is calculated from its velocity as

$$\frac{d\boldsymbol{x}_g}{dt} = \boldsymbol{u}_g \tag{1.20}$$

The E–L approach can be divided into two main branches, based on the term of the gas-volume fraction modeled in the simulation.

Model is not in the term of volume fraction

In the first branch, the bubble effects on the liquid phase is modeled based on the momentum point sources calculated using the reaction forces of the fluid acting upon the bubbles, and the volume fraction is not considered. Example of investigations using this approach is Fraga et al. (2016) and Caballina et al. (2003). The conservation equations of mass and momentum of the liquid phase is written as Caballina et al. (2003)

$$\nabla \cdot \boldsymbol{u}_l = 0 \tag{1.21}$$

$$\rho_l \left(\frac{\partial \boldsymbol{u}_l}{\partial t} + (\boldsymbol{u}_l \cdot \nabla)\boldsymbol{u}_l \right) = -\nabla p + \mu_l \nabla^2 \boldsymbol{u}_l + \boldsymbol{\Phi}_S \tag{1.22}$$

where $\boldsymbol{\Phi}_S$ is the effects of the momentum point sources, induced by the bubbles, on the liquid phase. The $\boldsymbol{\Phi}_S$ can be calculated using rectangular finite volume as (Caballina et al., 2003)

$$\boldsymbol{\Phi}_S(\boldsymbol{x}, t) = \frac{V_b}{V_f} \sum_{i=1}^{N_b} \left[\rho_g \left(\boldsymbol{g} - \frac{d\boldsymbol{u}_g}{dt} \right) + \rho_l \left(\frac{\partial \boldsymbol{u}_l}{\partial t} + \boldsymbol{u}_l \cdot \nabla \boldsymbol{u}_l - \boldsymbol{g} \right) \right] \tag{1.23}$$

where $V_b = \pi d_b^3/6$, d_b is the bubble diameter, $V_f = \Delta x \Delta y \Delta z$ is the volume of a grid cell, and N_b is number of bubbles.

The above momentum equation can be written in the term of the unresolved turbulence (filtered equation) as

$$\frac{\partial u_i}{\partial t} + \frac{\partial u_i u_i}{\partial x_j} = -\frac{\partial p}{\partial x_i} + 2\nu \frac{\partial (S_{ij})}{\partial x_j} - \frac{\tau_{ij}}{\partial x_j} + \zeta_i \tag{1.24}$$

where the ζ_i can be obtained using spherical finite volume as (Fraga et al., 2016)

$$\zeta_i = -\frac{1}{V_b} \sum_{b=1}^{N_b} \boldsymbol{F}_{b,i}^* \Delta V \tag{1.25}$$

$$\boldsymbol{F}_{b,i}^* = \boldsymbol{F}_{D,i} + \boldsymbol{F}_{L,i} + \boldsymbol{F}_{VM,i} + \boldsymbol{F}_{P,i} \tag{1.26}$$

and ΔV is calculated as

$$\Delta V = \frac{V_b}{V_{ball}} \frac{L_j}{L_k} \tag{1.27}$$

L_j/L_k is explained as the linear effects of a bubble to the considered grid node.

The term τ_{ij} is calculated using turbulent models such as LES model in the investigation by Fraga et al. (2016).

Model is in the term of volume fraction

In the second branch, the gas volume fraction is added to the momentum point sources to account for modification of the liquid continuity and momentum equations. Example of investigations using this approach is Finn et al. (2011), Cihonski et al. (2013), Delnoij et al. (1997a,b, 1999). The mass and momentum equations for the liquid phase can be written as Delnoij et al. (1997a)

$$\frac{\partial(\alpha_l\rho_l)}{\partial t} + \nabla\cdot(\alpha_l\rho_l\boldsymbol{u}_l) = 0 \tag{1.28}$$

$$\frac{\partial(\alpha_l\rho_l\boldsymbol{u}_l)}{\partial t} + \nabla\cdot(\alpha_l\rho_l\boldsymbol{u}_l\boldsymbol{u}_l) = -\alpha_l\nabla p - \nabla\cdot(\alpha_l\tau_l) + \alpha_l\rho_l\boldsymbol{g} + \boldsymbol{\Phi}_S \tag{1.29}$$

To eliminate the term $\boldsymbol{\Phi}_S$, Murai and Matsumoto (2000), Sugiyama et al. (2000) proposed an E–L model in which the gas phase is described in both Eulerian and Lagrangian frames, i.e., it is treated mathematically as both continuous phase and dispersion phase (each bubble is presented as a Lagrangian marker). The momentum equation for the Lagrangian motion of an individual bubble is written as

$$\rho_g V_b\frac{d\boldsymbol{u}_g}{dt} = \boldsymbol{F}_B + \boldsymbol{F}_D + \boldsymbol{F}_L + \boldsymbol{F}_{VM} + \boldsymbol{F}_P + \boldsymbol{F}_V \tag{1.30}$$

where $\boldsymbol{F}_B$, $\boldsymbol{F}_D$, $\boldsymbol{F}_L$, $\boldsymbol{F}_{VM}$, and $\boldsymbol{F}_P$ are forces mentioned above, and $\boldsymbol{F}_V$ is viscous force acting on the bubble expressed as

$$\boldsymbol{F}_V = V_b\mu_l\Big(\nabla^2\boldsymbol{u}_l + \frac{1}{3}\nabla(\nabla\cdot\boldsymbol{u}_l)\Big) \tag{1.31}$$

The momentum equation for the liquid phase is derived from a sum of two momentum equations of two phases, and it is written as

$$\frac{\partial(\alpha_l\rho_l\boldsymbol{u}_l)}{\partial t}+\nabla\cdot(\alpha_l\rho_l\boldsymbol{u}_l\boldsymbol{u}_l)+\frac{\partial(\alpha_g\rho_g\boldsymbol{u}_g)}{\partial t}+\nabla\cdot(\alpha_g\rho_g\boldsymbol{u}_g\boldsymbol{u}_g) = -\nabla p-(\alpha_l\rho_l+\alpha_g\rho_g)\boldsymbol{g}+\nabla\cdot\big((1+\alpha_g)\tau_l\big) \tag{1.32}$$

The E–L approach has the following benefits. First, the E–L approach can treat situations in which there is an exact distribution of bubble sizes, but the degree of accuracy in such cases will depend on the number of particles used, as well as the physics invoked. For example, the distribution of eight bubble sizes under interaction with a vortex ring was successfully simulated by Finn et al. (2011) and Cihonski et al. (2013). Second, bubble–bubble interaction for dense cases can be treated by constructing models such as those in the investigations by Delnoij et al. (1999), Lan and Garca (2006). Thirdly, the boundary conditions of the bubbles at the solid body, free surface, and bubble injection parts can be expressed more accurately. In addition, the Lagrangian description of bubble dynamics has been recently revised and examined by researchers such as Sridhar and Katz (1995) and Mazzitelli et al. (2003). However, Eulerian treatment of the nonlinear convection term for fluid flow, for example, by using finite-difference or spectral element schemes, leads to diffusion or dissipation errors (Cottet and Poncet, 2003; Cocle et al., 2008; Chatelain et al., 2008).

1.1.3 Lagrangian–Lagrangian approach

In the L–L approach, both phases are treated as Lagrangian markers. The liquid is discretized into fluid elements or particles by using smoothed particle hydrodynamics (SPH) methods and vortex methods. Compared to grid-based methods or Eulerian methods, Lagrangian methods for fluid flow have the advantages of automatic adaptation of computational elements and low numerical dissipation associated with the discretization of nonlinear convection (Cottet and Poncet, 2003; Cocle et al., 2008; Chatelain et al., 2008; Uchiyama and Matsumura, 2010).

The SPH methods were introduced by Lucy (1977) and further developed by Gingold and Monaghan (1985) for solving astrophysical problems. In SPH methods, a fluid is modelled by dividing it into a discrete set of particles that are evolved based on the weighted influence of their neighbors (Meister and Rauch, 2015). Each particle has individual mass, thermo-physical properties, and the ensemble can be considered as interconnected-fluid particles whose field values are governed based on the conservation laws of continuum fluid mechanics (Das and Das, 2009). In the gas phase, an individual bubble can be discretized into particles, as in the fluid phase, as given in the investigations of Meister and Rauch (2015), and Das and Das (2009). Moreover, one type of the L–L approach combines an SPH method for solving the fluid phase and each Lagrangian marker representing an individual bubble, for example, the investigation of Ihmsen et al. (2011).

Vortex methods are known to have superior ability in terms of analyzing the evolution of vortex structures, such as the formation and deformation of eddies of various scales (Uchiyama and Matsumura, 2010). Uchiyama (2004), Uchiyama and Degawa (2007, 2008) proposed a vortex method to simulate two-dimensional bubbly flow, and Uchiyama and Matsumura (2010) proposed vortex methods to simulate three-dimensional bubbly flow and gas-solid particle two-phase flow (Uchiyama and Naruse, 2003; Yagami and Uchiyama, 2007; Uchiyama and Yagami, 2005). The flow characteristics associated with the interaction of two phases can be successfully captured by using a vortex method, and the simulated results compare favorably with the corresponding measurements. However, these vortex methods distort the computational particle distribution, and the computational cost of Biot–Savart integration of velocity with $\mathcal{O}(N^2)$ operations is very high, where N is number of fluid elements. To overcome these issues, the Lagrangian methods for fluid flow have been improved to yield the semi-Lagrangian vortex methods or hybrid-Eulerian–Lagrangian methods.

1.1.4 Semi-Lagrangian–Lagrangian approach

In the semi-L–L approach, the gas phase is described in the Lagrangian frame, the liquid phase is solved in both the Eulerian and the Lagrangian frames, called semi-Lagrangian

approach or vortex-in-cell method or remeshed particle method.

The vortex-in-cell method retains the advantageous features of mesh-free methods and mesh-based methods and limits the disadvantages of both methods. In general, the vortex-in-cell method uses vortex elements or particle transport conservative quantities and grid-based formulas to calculate fields (Cottet and Poncet, 2003). The vortex elements carrying vorticity are arranged in Eulerian grids, while the velocity field is obtained from the vorticity field by solving Poisson equations. Clearly, the greatest advantage of the Eulerian methods is low computational cost in calculating the velocity obtained from the Poisson equation solved by a fast Poisson solver such as FISHPACK, PoisFFT, etc. After the vortex elements are transported by the convection term, interpolation schemes are used to redistribute the vortex elements on Eulerian grids while ensuring that the flow momentum is conserved. The spirit of the vortex-in-cell method is to avoid the high cost of Biot–Savart integration, while still benefitting from the most advantageous features of the Lagrangian vortex methods. The vortex-in-cell method was proposed by Birdsall and Fuss (1969) to simulate many-body plasmas in plasma physics and then adapted by Christiansen (1973) to simulate two-dimensional incompressible inviscid and homogeneous fluid flows. This method was later adapted for the two- and three-dimensional incompressible viscous fluid flows by Cottet and Koumoutsakos (2000). Cottet and Poncet (2003) proposed a vortex-in-cell method combined with the penalization method to simulate flow around the body. The method was proved to be a robust and efficient to simulate flow around two tandem cylinders, as shown in Appendix A. The vortex-in-cell method was improved to heighten its numerical accuracy and efficiency by Uchiyama et al. (2014b). Chen et al. (2014) improved the vortex-in-cell method by introducing the vorticity source term to consider two-way coupling between two phases, and the accuracy and computational efficiency were validated in a simulation of rising bubble clusters. Subsequently, a vortex-in-cell method was proposed by Uchiyama et al. (2015); Uchiyama and Shimada (2014) to simulate a variety of two-phase flows such as bubbly flows and solid particle-gas flows. The method is applicable to the simulation of two-phase flows.

1.2 Objective and construction

1.2.1 Objective

The research objective is described as follows:

First, based on the above literature review and previous investigation (Uchiyama et al., 2015), the semi-L–L approach will continue to be developed to adapt to the simulations of the gas–liquid two-phase flows around a rigid obstacle.

Second, a comprehensive understanding of the flow phenomena of the gas–liquid two-phase flows is key to improve the design and control related engineering devices. Therefore, the characteristics of the evolution of annular bubble, the interaction between a vortex

ring and a bubble plume, and the flow around a circular cylinder inside a bubble plume will be clarified.

1.2.2 Construction

The remainder of this dissertation was organized as follows:

In Chapter 2, a semi-L–L approach for the simulation of the gas–liquid two-phase flow was explained in a detail. The simulation of the evolution of annular bubble plume was implemented to validate the numerical model. Moreover, the characteristics of the bubbly flows such as the vortex structure of the liquid phase induced by bubble movement and the interactions between two phases were discussed.

In Chapter 3, the simulation of a vortex ring launched vertically upward into annular bubble plume was conducted to investigate the characteristics of the interactions between a vortex and a bubble plume. The approach was also validated by comparing the simulation results such as liquid-velocity distribution, vortex-ring displacement, and bubble entrainment into the vortex ring to the corresponding experimental measurements. The bubble dynamics and the transportability of the bubbles by a vortex ring were clarified. Additionally, the effects of entrained bubbles upon the vortex structure were investigated.

In Chapter 4, the simulation of the gas–liquid two-phase flow around a circular cylinder was conducted. The numerical method was validated by using some benchmark simulation and experiment cases. The characteristics of the behavior of the bubble plume around the cylinder and the induced vortex structure of the liquid phase were clarified.

Conclusion was given in Chapter 5.

Chapter 2

Numerical simulation of an annular bubble plume

2.1 Introduction

In this chapter, the vortex-in-cell method for simulating bubbly two-phase flow (Uchiyama et al., 2015) is combined with an immersed boundary method, as investigated in Appendix A, to investigate the evolution of the three-dimensional vortex structure of a liquid flow induced by an annular bubble plume. The semi-Lagrangian–Lagrangian (semi-L–L) approach will be described.

A variety of benchmark cases have been used to investigate bubbly two-phase flows, such as a bubble plume from a single injection point (Schwarz and Turner, 1988; Torvik and Svendsen, 1990; Socolofsky et al., 2008; Johansen and Boysan, 1988; Swan and Moros, 1993), plane bubble plume (Alam and Arakeri, 1993; Caballina et al., 2003; Uchiyama and Degawa, 2008), bubble columns (Sokolichin and Eigenberger, 1997, 1999; Tabib et al., 2008; Delnoij et al., 1997a,b, 1999), and bubble–laden mixing layer (Yang et al., 2002). However, in this study, the experimental investigation of the annular bubble plume by Uchiyama and Kusamichi (2013) is employed to study bubbly two-phase flows. An annular bubble plume can be considered a distinctive case of a plane bubble plume in which the injection line is bent into a circle. Bubbles released from an annulus rise upward due to buoyancy force. The rising bubbles generate vortex structures of various scales surrounding the bubble plume. New phenomena related to vortex dynamics generated by an annular bubble plume will be discovered and clarified. The remainder of this chapter is organized as follows: an explanation of the basic equations for two-phase flows is given in section 2.2, the numerical simulation method is described in section 2.3, a discussion of the result is given in section 2.4, and our conclusions are given in section 2.5.

2.2 Basic equations

2.2.1 Assumptions

Simulation of gas–liquid two-phase flow is performed with the following assumptions:

(i) the mixture is a gas–liquid bubbly flow with small entrained bubbles;

(ii) the two phases are incompressible, and no phase change occurs;

(iii) the mass and momentum of the gas phase are very small and negligible compared to those of the liquid phase; and

(iv) the bubbles conserve their spherical shape, and neither fragmentation nor coalescence occurs.

2.2.2 Governing equation for liquid and gas phases

The conservation equations for the mass and momentum of the liquid flow, based on the above-mentioned assumptions, are explained as below (Chen et al., 2014; Sokolichin and Eigenberger, 1997, 1999; Uchiyama and Matsumura, 2010; Uchiyama and Degawa, 2007, 2008; Uchiyama et al., 2015):

$$\frac{\partial \alpha_l}{\partial t} + \nabla \cdot (\alpha_l \boldsymbol{u}_l) = 0 \tag{2.1}$$

$$\alpha_l \frac{D\boldsymbol{u}_l}{Dt} = -\frac{1}{\rho_l}\nabla p + \nu_l \nabla^2 \boldsymbol{u}_l + \alpha_l \boldsymbol{g} \tag{2.2}$$

where

$$\frac{D\boldsymbol{u}_l}{Dt} = \frac{\partial \boldsymbol{u}_l}{\partial t} + \big(\boldsymbol{u}_l \cdot \nabla\big)\boldsymbol{u}_l \tag{2.3}$$

and α_l is the liquid volume fraction which satisfies the gas volume fraction α_g as follows:

$$\alpha_l + \alpha_g = 1 \tag{2.4}$$

With the above-mentioned assumptions, the forces acting on an individual bubble include buoyancy force $\boldsymbol{F}_B$, drag force $\boldsymbol{F}_D$, lift force $\boldsymbol{F}_L$, virtual mass force or added mass force $\boldsymbol{F}_{VM}$, and pressure gradient force $\boldsymbol{F}_P$. Hence, the momentum equation of the motion of an individual bubble, proposed by Auton et al. (1988), and recently reviewed by Sridhar and Katz (1995), Mazzitelli et al. (2003), and employed for E–L model (Fraga et al., 2016; Krause et al., 2010; Murai and Matsumoto, 2000; Johansen and Boysan, 1988; Swan and Moros, 1993; Caballina et al., 2003; Delnoij et al., 1997a,b, 1999), and L–L model (Uchiyama and Matsumura, 2010; Uchiyama and Degawa, 2008), and semi-L–L model (Chen et al., 2014; Uchiyama and Yagami, 2005), is expressed as follows:

$$\rho_g V_b \frac{d\boldsymbol{u}_g}{dt} = \boldsymbol{F}_B + \boldsymbol{F}_D + \boldsymbol{F}_L + \boldsymbol{F}_{VM} + \boldsymbol{F}_P \tag{2.5}$$

where

$$\boldsymbol{F}_B = \big(\rho_g V_b - \rho_l V_b\big)\boldsymbol{g} \tag{2.6}$$

$$\boldsymbol{F}_D = \frac{1}{2} C_D \rho_l A_b |\boldsymbol{u}_g - \boldsymbol{u}_l| \big(\boldsymbol{u}_g - \boldsymbol{u}_l\big) \tag{2.7}$$

$$\boldsymbol{F}_L = -C_L \rho_l V_b \big(\boldsymbol{u}_g - \boldsymbol{u}_l\big) \times (\nabla \times \ \boldsymbol{u}_l) \tag{2.8}$$

$$\boldsymbol{F}_{VM} = C_V \rho_l V_b \Big(\frac{D\boldsymbol{u}_l}{Dt} - \frac{d\boldsymbol{u}_g}{dt}\Big) \tag{2.9}$$

$$\boldsymbol{F}_P = \rho_l V_b \frac{D\boldsymbol{u}_l}{Dt} \tag{2.10}$$

where $A_b = 0.25\pi d_b^2$ and d_b is the bubble diameter. Equation (2.5) is rewritten as follows:

$$\frac{d\boldsymbol{u}_g}{dt} = \frac{1+C_V}{\beta+1}\frac{D\boldsymbol{u}_l}{Dt} - \frac{1}{\beta+C_V}\frac{3C_D}{4d_b}|\boldsymbol{u}_g-\boldsymbol{u}_l|(\boldsymbol{u}_g-\boldsymbol{u}_l) + \frac{\beta-1}{\beta+C_V}\boldsymbol{g} - \frac{C_L}{\beta+C_V}(\boldsymbol{u}_g-\boldsymbol{u}_l)\times(\nabla\times\boldsymbol{u}_l) \tag{2.11}$$

where, β is the density ratio between the gas and the fluid phases, ρ_g and ρ_l, and the virtual mass and lift coefficients equal 0.5. The Reynolds number of bubbles in the current simulation is less than 100; therefore, the drag coefficient of an individual spherical bubble is expressed as follows (Chen et al., 2014; Finn et al., 2011; Cihonski et al., 2013; Sridhar and Katz, 1995; Mazzitelli et al., 2003)

$$C_D = \frac{24}{Re_b}\left(1 + 0.15Re_b^{0.687}\right) \tag{2.12}$$

where

$$Re_b = \frac{d_b|\boldsymbol{u}_g - \boldsymbol{u}_l|}{\nu_l} \tag{2.13}$$

The Lagrangian trajectories of bubbles, $\boldsymbol{x}_g$, are calculated from their velocity as follows:

$$\frac{d\boldsymbol{x}_g}{dt} = \boldsymbol{u}_g \tag{2.14}$$

2.2.3 Vorticity equation and orthogonal decomposition of liquid velocity

Taking the curl of Eq. (2.2), the velocity–vorticity equation of the fluid phase is derived, as detailed in Appendix B

$$\frac{\partial\boldsymbol{\omega}}{\partial t} + (\boldsymbol{u}_l\cdot\nabla)\boldsymbol{\omega} = (\boldsymbol{\omega}\cdot\nabla)\boldsymbol{u}_l + \frac{\nu_l}{\alpha_l}\nabla^2\boldsymbol{\omega} + \frac{1}{\alpha_l}\nabla\alpha_l\times\left(\boldsymbol{g} - \frac{D\boldsymbol{u}_l}{Dt}\right) \tag{2.15}$$

where the vector vorticity $\boldsymbol{\omega}$ is defined as follows:

$$\boldsymbol{\omega} = \nabla\times\boldsymbol{u}_l \tag{2.16}$$

According to the Helmholtz theorem, velocity $\boldsymbol{u}_l$ is represented as the summation of the curl of a vector potential $\boldsymbol{\psi}$ and the gradient of a scalar potential ϕ:

$$\boldsymbol{u}_l = \nabla\times\boldsymbol{\psi} + \nabla\phi \tag{2.17}$$

The velocity calculated using Eq. (2.17) remains unaltered even when any gradient of the scalar potential function is added to. To remove this arbitrariness, a solenoidal condition is imposed on $\boldsymbol{\psi}$:

$$\nabla\cdot\boldsymbol{\psi} = 0 \tag{2.18}$$

Taking the curl of Eq. (2.17) and substituting Eq. (2.18) into the resultant equation, the vector Poisson equation for $\boldsymbol{\psi}$ is derived as follows:

$$\nabla^2\boldsymbol{\psi} = -\boldsymbol{\omega} \tag{2.19}$$

When substituting Eq. (2.17) into the continuity equation, Eq. (2.1), and rewriting the resultant equation by using the relationship $\nabla\cdot(\nabla\times\boldsymbol{\psi})$, the Poisson equation of ϕ is obtained as follows:

$$\frac{\partial\alpha_l}{\partial t} + \alpha_l\nabla^2\phi + (\nabla\phi + \nabla\times\boldsymbol{\psi})\cdot\nabla\alpha_l = 0 \tag{2.20}$$

2.3 Vortex-in-cell method for bubbly flow

2.3.1 Discretization of vorticity field by vortex elements

The vortex-in-cell (VIC) method discretizes the vorticity field into vortex elements p with vorticity $\boldsymbol{\omega}_p$ and their velocity $\boldsymbol{u}_l$, as given by the value of velocity field at their location $\boldsymbol{x}_p = (x_p, y_p, z_p)$. The vorticity–velocity equation, Eq. (2.15), is rewritten based on the Lagrangian description of vortex elements as follows:

$$\frac{d\boldsymbol{x}_p}{dt} = \boldsymbol{u}_l(\boldsymbol{x}_p) \tag{2.21}$$

$$\frac{d\boldsymbol{\omega}_p}{dt} = \Big(\boldsymbol{\omega}(\boldsymbol{x}_p)\cdot\nabla\Big)\boldsymbol{u}_l(\boldsymbol{x}_p) + \frac{\nu_l}{\alpha_l}\nabla^2\boldsymbol{\omega}(\boldsymbol{x}_p) + \frac{1}{\alpha_l}\nabla\alpha_l \times \left(\boldsymbol{g} - \frac{D\boldsymbol{u}_l(\boldsymbol{x}_p)}{Dt}\right) \tag{2.22}$$

The vortex element velocity $\boldsymbol{x}_p$ is calculated using Eq. (2.17) on grid nodes, while $\boldsymbol{\psi}$ and ϕ are obtained by solving Poisson Eqs. (2.19) and (2.20), respectively. The vorticity $\boldsymbol{\omega}$ in Eq. (2.19) is $\boldsymbol{\omega}(\boldsymbol{x}_p)$, and it is obtained by solving Eq. (2.22) considering vortex stretching, diffusion, and external sources. The vortex elements carrying their vorticity $\boldsymbol{\omega}(\boldsymbol{x}_p)$ transport to a new location due to the convection term in Eq. (2.21). Subsequently, the new vortex elements are created on grid nodes by using an interpolation scheme. Supposing that after the Lagrangian calculation of Eqs. (2.21) and (2.22), the vortex elements have vorticity $\boldsymbol{\omega}(\boldsymbol{x}_p)$ and location $\boldsymbol{x}_p$, the new vortex elements are created at grid location $\boldsymbol{x}_q = (x_q, y_q, z_q)$. The new vortex elements carry vorticity $\boldsymbol{\omega}(\boldsymbol{x}_q)$ calculated from $\boldsymbol{\omega}(\boldsymbol{x}_p)$ as follows:

$$\boldsymbol{\omega}(\boldsymbol{x}_q) = \sum_{p}^{N_p} \boldsymbol{\omega}_p W\Big(\frac{x_q - x_p}{\Delta x}\Big) W\Big(\frac{y_q - y_p}{\Delta y}\Big) W\Big(\frac{z_q - z_p}{\Delta z}\Big) \tag{2.23}$$

where N_p is the number of vortex elements, Δx, Δy, and Δz are cell widths. W is a third-order accurate kernel-interpolation function, as shown in detail in Section A.2.2 of Appendix A.

2.3.2 Calculation of gas volume fraction

The liquid volume fraction calculated using Eq. (2.4) is defined on the grid nodes; therefore, the gas volume fraction is computed on the grid nodes as well. Supposing that a bubble of volume V_b belongs to a cell; the gas volume fraction of this individual bubble is calculated as follows:

$$\alpha_g = \frac{V_b}{\Delta x \Delta y \Delta z} \tag{2.24}$$

The gas volume fraction obtained using Eq. (2.24) remains unchanged even when the bubble moves inside the cell. However, the gas volume fraction changes discontinuously from 1 to 0 when the bubble moves out of the cell, as shown in Fig. 2.2 (a). To overcome this problem, the gas volume fraction is computed by interpolating the volume of a bubble

to the grid nodes placed around it, as shown in Fig. 2.1 (b). Considering the one-dimensional form, the gas volume fraction at grid position $\boldsymbol{x}_q$ is calculated from a bubble at position $\boldsymbol{x}_g$ as follows:

$$\alpha_g(x_q) = \frac{V_b}{\Delta x} W_\alpha\Big(\frac{x_q - x_g}{\Delta x}\Big) \tag{2.25}$$

where W_α is triangular function, and it was employed in (Cottet and Koumoutsakos, 2000) as follows:

$$W_\alpha(\varepsilon) = \begin{cases} 0 & \text{if } |\varepsilon| > 1 \\ 1 - |\varepsilon| & \text{if } |\varepsilon| \le 1 \end{cases} \tag{2.26}$$

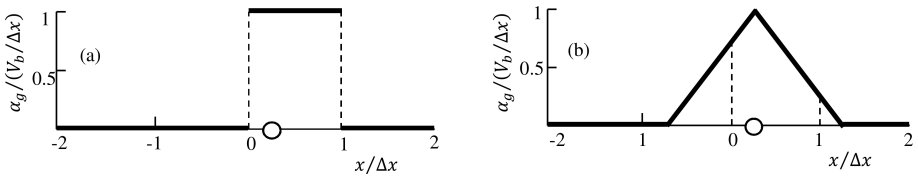

Figure 2.1: Calculation of gas volume fraction. Figures (a) and (b) represent the calculation of gas volume fraction by using Delta and linear functions, respectively. The bubble location is represented by circles.

The function, W_α, satisfies the following properties: $W_\alpha(\varepsilon) \ge 0$, $\int_{-\infty}^{\infty} W_\alpha = 1$, and $W_\alpha(0) = 1$. This means the value of the gas volume fraction must be positive, the sum of the volume of bubbles is conserved on grid nodes, and the volume impact of a bubble on its position is itself, respectively. It may be possible to use Eq. (A.11) instead of Eq. (2.26), but Eq. (A.11) does not satisfy the above-mentioned properties.

Because W_α is a linear interpolation function, the gas volume fraction in three-dimensional form is calculated as the product of three one-dimensional forms and is written as follows:

$$\alpha_g(\boldsymbol{x}_q) = \frac{V_b}{\Delta x \Delta y \Delta z} W_\alpha\Big(\frac{x_q - x_g}{\Delta x}\Big) W_\alpha\Big(\frac{y_q - y_g}{\Delta y}\Big) W_\alpha\Big(\frac{z_q - z_g}{\Delta z}\Big) \tag{2.27}$$

For the number of bubbles, N_b, the gas volume fraction is computed by the summation on each grid point as

$$\alpha_g(\boldsymbol{x}_q) = \sum_p^{N_b} \frac{V_b}{\Delta x \Delta y \Delta z} W_\alpha\Big(\frac{x_q - x_g}{\Delta x}\Big) W_\alpha\Big(\frac{y_q - y_g}{\Delta y}\Big) W_\alpha\Big(\frac{z_q - z_g}{\Delta z}\Big) \tag{2.28}$$

2.3.3 Discretization by staggered grid and correction of vorticity field

The capability of the vortex-in-cell method combined with staggered grid schemes has proven to prevent numerical oscillation and improve accuracy by discretizing equations in a consistent manner (Uchiyama et al., 2014b). Figure 2.2 shows the arrangement of flow quantities in a cell. The vector potential, $\boldsymbol{\psi}$, and vorticity field, $\boldsymbol{\omega}$, are defined on the cell edges, while the vector liquid velocity, $\boldsymbol{u}_l$ is defined on the centers of cell surfaces. The

scalar potential, ϕ, and liquid volume fraction, α_l, is defined at the cell center.

The process of solving the momentum equation and redistributing vortex particles onto the grid nodes generates numerical errors. The condition of the vorticity being a solenoidal vector field is not satisfied; this means $\nabla \cdot \boldsymbol{\omega} \neq 0$. To achieve this condition, the vorticity can be corrected using one of two methods. The first method is the projection used widely in 'vortex methods community'. Based on Helmholtz's theorem, the vorticity field is decomposed into an irrotational (curl-free, $\nabla \times P = 0$) vector field and a solenoidal (divergence-free, $\nabla \cdot \boldsymbol{Q} = 0$) vector field as

$$\boldsymbol{\omega} = \nabla P + \nabla \times \boldsymbol{Q} \tag{2.29}$$

Taking divergence operation on both sides of Eq. (2.29), the result is obtained as

$$\nabla^2 P = \nabla \cdot \boldsymbol{\omega} \tag{2.30}$$

The Poisson equation, Eq. (2.30), is solved to obtain P, then the vorticity field is corrected by eliminating the irrotational term, ∇P, as

$$\boldsymbol{\omega}_{corrected} = \boldsymbol{\omega} - \nabla P \tag{2.31}$$

In the second method, the vorticity field is corrected using Eq. (4.10), i.e., $\boldsymbol{\omega}_{corrected} = \nabla \times \boldsymbol{u}_l$ (Uchiyama et al., 2014b), because

$$\nabla \cdot \boldsymbol{\omega} = \nabla \cdot (\nabla \times \boldsymbol{u}_l) = \nabla \times (\nabla \cdot \boldsymbol{u}_l) = 0 \tag{2.32}$$

The solenoidal condition of the vorticity is satisfied when using one of two methods. It is noted that no theory is based on to lead a correction of the vorticity using the Eq. (2.31) or Eq. (4.10). However, these methods were proved as good solutions for this problem by Uchiyama et al. (2014b), Cottet and Poncet (2002). Due to a requirement of solving the Poisson equation (2.30), the computational cost using the first method is higher than that using the second method. In the current simulation, the second method was employed to correct the vorticity field. In the present simulation, the vorticity correction is performed after every 50 time steps.

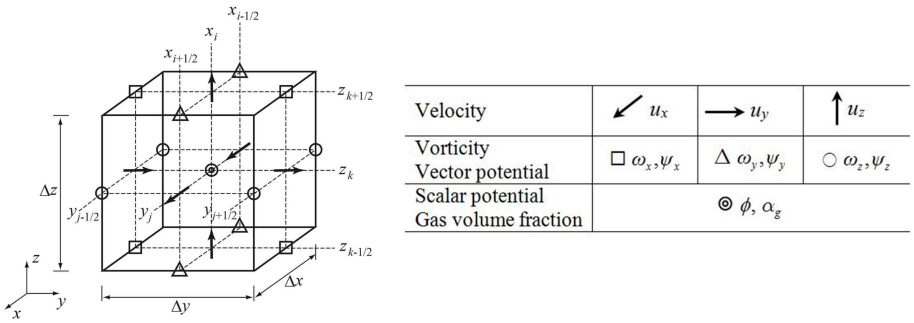

Figure 2.2: Flow quantities arranged on a staggered-grid cell

2.3.4 Immersed boundary method for no-slip condition

The immersed boundary (IB) method was originally proposed by Peskin (1972) and proved by Cottet and Poncet (2003) to be robust and applicable for simulating the flow around a solid body. In the present study, we use an IB method with the VIC method to satisfy the no-slip condition on the body surface. When using the penalization method (Cottet and Poncet, 2003), which is a type of immersed boundary method, the vorticity–velocity equation (Eq. (2.22)) is rewritten as follows:

$$\frac{d\boldsymbol{\omega}_p}{dt} = \Big(\boldsymbol{\omega}(\boldsymbol{x}_p)\cdot\nabla\Big)\boldsymbol{u}_l(\boldsymbol{x}_p) + \frac{\nu_l}{\alpha_l}\nabla^2\boldsymbol{\omega}(\boldsymbol{x}_p) + \frac{1}{\alpha_l}\nabla\alpha_l\times\Big(\boldsymbol{g} - \frac{D\boldsymbol{u}_l(\boldsymbol{x}_p)}{Dt}\Big) + \nabla\times\Big[\lambda\chi_s\Big(\boldsymbol{u}_s - \boldsymbol{u}(\boldsymbol{x}_p)\Big)\Big] \tag{2.33}$$

where $\boldsymbol{u}_s$ is the velocity of the solid body, and λ is the penalization parameter. χ_s that classifies the solid and fluid regions is given as follows:

$$\chi_s(x) = \begin{cases} 1 & \text{if } x \in S \\ 0 & \text{if } x \in F \end{cases} \tag{2.34}$$

where S and F denote the solid and fluid regions, respectively, as shown in Fig. 2.3. χ_s is varied smoothly from 0 to 1 near the fluid–solid interface using a Heaviside function shown in Section A.2.3 of Appendix A.

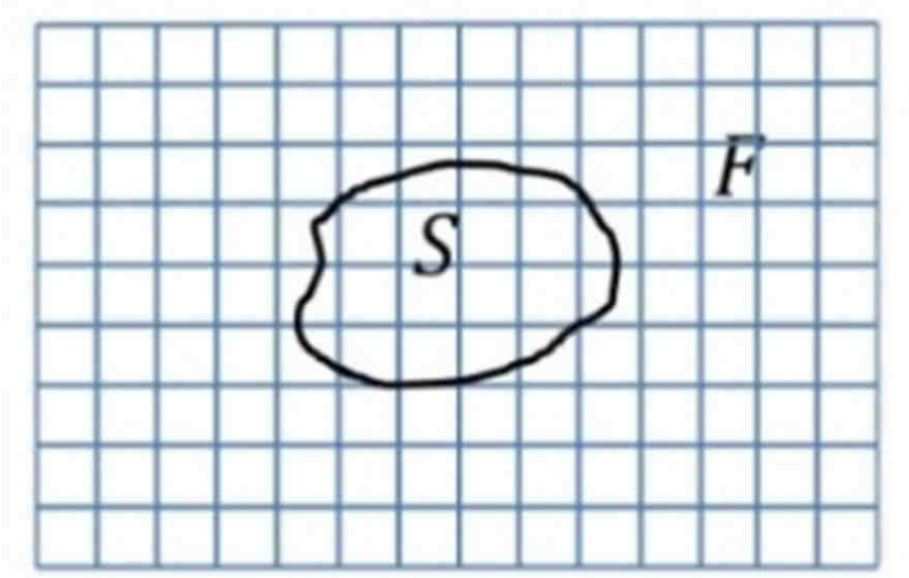

Figure 2.3: Two-dimensional configuration of solid and fluid regions S and F, respectively

In the present simulation, we use three-dimensional staggered grids to arrange the liquid velocity components on the centers of cell surfaces; hence, three χ_s are created on three grid systems of liquid velocity components.

Equation (2.33) is solved by splitting methods; therefore, the penalization velocity $\boldsymbol{u}_\lambda$ term to implement the no-slip condition at the fluid–solid interface is expressed as follows:

$$\frac{d\boldsymbol{u}_l(\boldsymbol{x}_p)}{dt} = \lambda\chi_s(\boldsymbol{u}_s - \boldsymbol{u}_l) \tag{2.35}$$

By choosing $\lambda = \frac{1}{\Delta t}$ and applying the forward finite-difference scheme, the velocity field in Eq. (2.35) is computed as

$$\boldsymbol{u}_\lambda = (1 - \chi_s)\boldsymbol{u}_l + \chi_s \boldsymbol{u}_s \tag{2.36}$$

The penalization vorticity is calculated by summation of its previous simulation time step value and its change as

$$\boldsymbol{\omega_\lambda} = \boldsymbol{\omega} + \Delta\boldsymbol{\omega} \tag{2.37}$$

Here, the change in vorticity, $\Delta\boldsymbol{\omega}$, is obtained from the change in velocity as

$$\Delta\boldsymbol{\omega} = \nabla \times (\boldsymbol{u}_\lambda - \boldsymbol{u}_l) \tag{2.38}$$

When substituting the Eq. (2.36) into Eq. (2.38) and substituting the resulting equation into Eq. (2.37), the penalization vorticity is calculated as

$$\boldsymbol{\omega_\lambda} = \boldsymbol{\omega} + \nabla \times (\chi_s(\boldsymbol{u}_s - \boldsymbol{u}_l)) \tag{2.39}$$

2.3.5 Numerical procedure

Given a flow at time t, the flow at $t + \Delta t$ is simulated by the following procedure:

(1) calculate the momentum equation of the bubble, Eq. (2.11), to obtain bubble velocity, $\boldsymbol{u}_g$;

(2) calculate the Lagrangian trajectory of the bubble $\boldsymbol{x}_g$ using Eq. (2.14);

(3) calculate the gas volume fraction α_g using Eq. (2.28), and the liquid volume fraction α_l using Eq. (2.4);

(4) calculate the strength of $\boldsymbol{\omega}(\boldsymbol{x}_g)$ using Eq. (2.22) to account for vortex diffusion, stretching, and external sources;

(5) calculate the convection of liquid elements $\boldsymbol{x}_p$ using Eq. (2.21);

(6) calculate the redistribution of liquid vorticity field $\boldsymbol{\omega}$ using Eq. (2.23);

(7) calculate the vector potential of liquid $\boldsymbol{\psi}$ using Eq. (2.19);

(8) calculate the scalar potential of liquid ϕ using Eq. (2.20);

(9) calculate the liquid velocity $\boldsymbol{u}_l$ using Eq. (2.17);

(10) calculate the correction of the liquid vorticity field $\boldsymbol{\omega}$ using Eq. (2.16);

(11) calculate the penalization velocity $\boldsymbol{u}_\lambda$ using Eq. (2.36) to implement the no-slip condition at the cylinder surface;

(12) calculate the penalization vorticity $\boldsymbol{\omega_\lambda}$ using Eq. (2.39).

Equations (2.11) and (2.14) are calculated using the forward finite-difference scheme. The fluid velocity on the right-hand side of Eq. (2.11) is obtained by interpolating from grid location to bubble location by using Eq. (2.23). In Eq. (2.22), the temporal variation is calculated using the two-step Adams–Bashforth method, the spatial variation is evaluated using the fourth-order accurate staggered-grid finite-difference scheme. Fluid particles tracking in Eq. (2.21) is computed using the forward finite-difference scheme. The Poisson equation (2.19) is solved by employing the Fourier method with the

periodic boundary condition. The FFTW3 library (http://www.fftw.org) is employed to calculate the Fourier transform. After solving Eq. (2.19), the vector of potential is modified to satisfy the no-slip condition at the wall and the slip condition at the fluid surface. The Poisson equation (2.20) is solved using the successive-over-relaxation method.

2.4 Result and discussion

2.4.1 Simulation conditions

The simulation conditions are set to be as the same as the experimental conditions (Uchiyama and Kusamichi, 2013). Figure 2.4 shows the bubbly flow configuration. An empty cylinder with an outer diameter of $D = 58$ mm, inner diameter of $0.74D$, and height of $0.8D$ is placed at the bottom of a tank. The bubbles located around the outer cylinder surface are released from the height of $h = 0.7D$. Affected by buoyancy force, the bubbles rise and induce liquid flow around them. The tank size ($L_x \times L_y \times L_z$) is selected to be similar to the tank used in the experiment, and its dimensions are $5.16D \times 5.16D \times 5.16D$ divided into $100 \times 100 \times 100$ cubic cells. Investigation of the effects of various tank sizes on the dynamics of the bubble plume is very time consuming. Moreover, the effects of various tank sizes on the dynamics of the bubble plume are out of the scope of this study. This effect could be considered in the future study. Under the present simulation conditions, the fluid time scale is larger than the bubble time scale. The value of the time step Δt in the simulation is based on an investigation of the bubble plume with the same bubble diameter (Uchiyama et al., 2015) and is equivalent to the bubble time scale calculated using the formula $\tau_b = d_b^2/(36\nu_l)$ (Caballina et al., 2003). The non-dimensional time step, $(u_t/D)\Delta t$, is set to 0.000276. The bubble diameter is generated randomly, and it lies in the range 0.15–0.25 mm. The bubble diameter is similar to that in the experiment, and it satisfies the assumptions mentioned in section 2.2.1. Specifically, the bubble diameter must be smaller than the cell width, Δx, to avoid any numerical difficulties when solving Eq. (2.22). Moreover, the release location of the bubbles is selected randomly around the cylinder. The bubbles are released with zero velocity. The number of bubbles released satisfies the bubble flow rate Q = 4.1 mm^3/s.

In industrial devices handling bubbly flows, bubbles having various diameters are observed depending on the flow regime. Recently, some devices utilizing so-called micro-bubbles with an extremely small diameter of 0.2 mm or less have been developed for aeration and cleaning. Their performance is revealed to be much higher than that of the existing devices. In this paper, the proposed simulation method is applied to the analysis of the flow laden with such micro-bubbles to demonstrate the applicability and validity.

At the cylinder surfaces, the penalization method explained above is employed to implement the no-slip condition.

At the bottom and side surfaces of the tank, the liquid velocity is zero (no-slip condition), that is, $\boldsymbol{u}_l = 0$, the vector potential and the scalar potential satisfy the non-

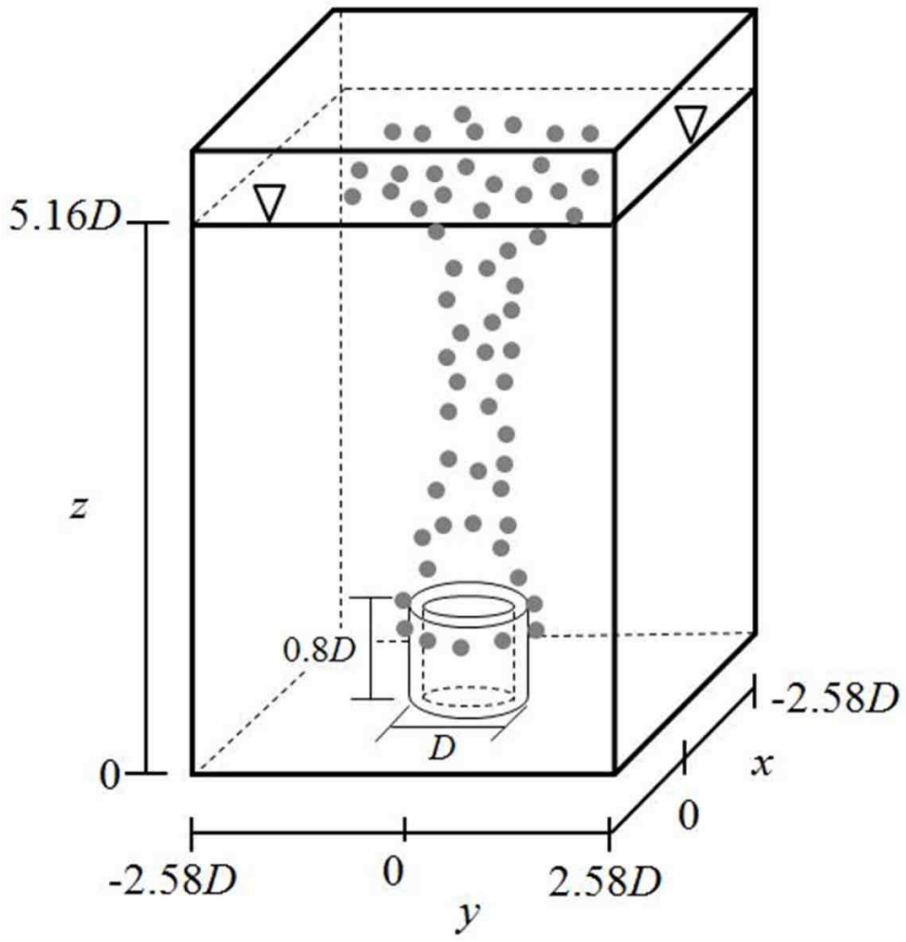

Figure 2.4: Configuration of bubbly flow

penetration condition (Uchiyama et al., 2014b; Wong and Reizes, 1984; Raul et al., 1990; Pasquetti and Bwemba, 1994) and solenoidal condition ($\nabla \cdot \boldsymbol{\omega} = 0$), for example, at $x = 2.58D$

$$\frac{\partial \psi_x}{\partial x} = \psi_y = \psi_z = 0 \tag{2.40}$$

$$\frac{\partial \phi}{\partial x} = 0 \tag{2.41}$$

The non-penetration condition is derived from the requirement of mass conservation at the considered plane as in (Wong and Reizes, 1984)

$$\iint_S \boldsymbol{u}_l \, dS = \iint_S (\nabla \times \boldsymbol{\psi} + \nabla\phi) \, dS \overset{\texttt{Stokes's theorem}}{=} \iint_S \nabla\phi \, dS + \oint_L \boldsymbol{\psi} \, dl = 0 \tag{2.42}$$

where S is the plane ($x = 2.58D$) and L is the closed border of S. Eqs. (2.40) and (2.41) are a solution of Eq. (2.42). It is noted that the conditions of the vector and scalar potentials, Eqs. (2.40) and (2.41), do not fulfill all the conditions of liquid-velocity components ($\boldsymbol{u}_l = 0$). In general, the derivatization of the vector and scalar potentials can satisfy only the condition of tangential or normal liquid-velocity components, as can be seen in (Wong and Reizes, 1984). Despite this, in the current method, both no-slip condition ($\boldsymbol{u}_l = 0$) and non-penetration condition (Eqs.(2.40) and (2.41)) are employed

for the simulation. This has been proven to be a good combination for the simulation of wall-bounded flow (Uchiyama et al., 2014b). It is conjectured that applying both the no-slip and non-penetration conditions at the wall in every time step leads to a convergence of both conditions in which the vector and scalar potentials asymptote to satisfy all conditions of liquid-velocity components.

At the fluid surface, the deformation is ignored, and a free-slip condition is assumed to be applicable. The normal velocity and the gradient of the tangential velocity with respect to the fluid surface are zero:

$$u_z = \frac{\partial u_x}{\partial y} = \frac{\partial u_z}{\partial z} = 0 \tag{2.43}$$

Substituting Eq. (2.12) into Eq. (2.43), the following equations are obtained

$$\frac{\partial \psi_y}{\partial x} - \frac{\partial \psi_x}{\partial y} + \frac{\partial \phi}{\partial z} = 0 \tag{2.44}$$

$$\frac{\partial^2 \psi_z}{\partial y \partial z} - \frac{\partial^2 \psi_y}{\partial z^2} + \frac{\partial}{\partial z}\left(\frac{\partial \phi}{\partial x}\right) = 0 \tag{2.45}$$

$$\frac{\partial^2 \psi_x}{\partial z^2} - \frac{\partial^2 \psi_z}{\partial x \partial z} + \frac{\partial}{\partial z}\left(\frac{\partial \phi}{\partial y}\right) = 0 \tag{2.46}$$

Eqs. (2.45) and (2.46) are satisfied when the vector and scalar potentials at the top surface of the domain are calculated as

$$\frac{\partial^2 \psi_x}{\partial z^2} = \frac{\partial^2 \psi_y}{\partial z^2} = \frac{\partial \psi_z}{\partial z} = 0 \tag{2.47}$$

$$\frac{\partial \phi}{\partial z} = 0 \tag{2.48}$$

The conditions of the vector and scalar potentials (Eqs. (2.47) and (2.48)) and the liquid velocity (Eq. (2.43)) are applied at the top surface of the domain in every simulation-time step.

2.4.2 Various scales of vortex structure

The bubbles released from the bottom of the computational domain, as described above, rise owing to buoyancy force. The movement of bubbles generates various eddies surrounding the bubble plume. An eddy is defined as a region with a positive second invariant, Q , representing the local balance between the shear-strain rate and the magnitude of vorticity, as mentioned by Jeong and Hussanin (1995), and it is expressed as follows:

$$Q \equiv 0.5(u_{i,i}^2 - u_{i,j}u_{i,j}) = -0.5u_{i,j}u_{j,i} = 0.5(||\Omega||^2 - ||S||^2) \tag{2.49}$$

where S and Ω are the symmetric and antisymmetric components of $\nabla \boldsymbol{u}$, and they are written as $S_{ij} = 0.5(u_{i,j} + u_{j,i}$ and $\Omega_{ij} = 0.5(u_{i,j} + u_{j,i})$, respectively. Hence, in this investigation, we use the Q criterion to analyze formation and deformation of the vortex

structure.

Figure 2.5 shows the time evolution of the Q value and three-dimensional bubble distribution, where t^* is the dimensionless time calculated as $t^* = t(u_t/D)$. In the early stage of the flow, as seen at $t^* = 5.5$, at the fluid surface, two vortex rings called the outer vortex ring and inner vortex ring are generated outside and inside the bubble plume, respectively. Subsequently, the outer vortex ring enlarges, while the inner vortex ring moves downward at $t^* = 8.3$. Various vortex rings are observed along the bubble plume. The vortex rings are deformed as can be seen at $t^* = 11$ and 13.8, and this deformation is explained later. At $t^* = 16.5$, the outer vortex ring enlarges continuously, and its strength decreases. Another vortex ring develops at the fluid surface, and the various deformed vortex rings inside the bubble plume move downward. These vortex rings are generated as a result of the meandering motion of the bubble plume and the effect of the fluid surface. Fully developed flow is observed from $t^* = 18.8$.

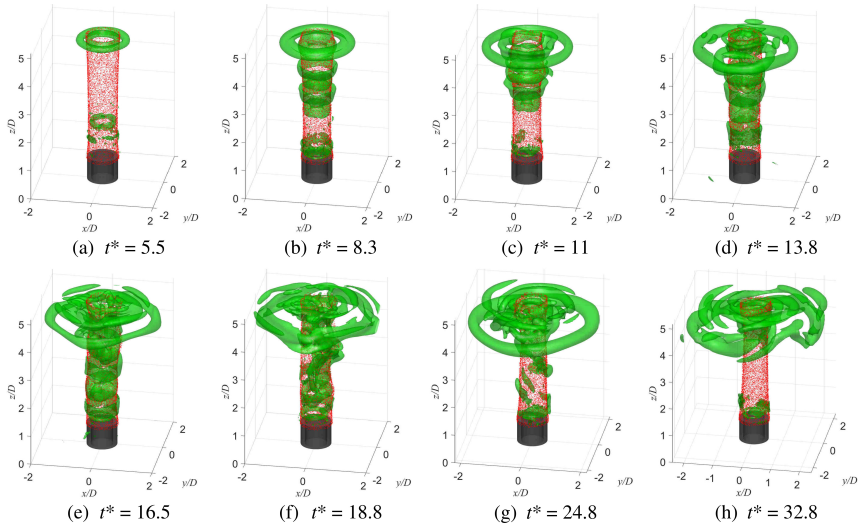

Figure 2.5: Time evolution of iso-surface of Q . $Q = 0.05$ is represented by green surfaces, three-dimensional bubble distribution is represented by red dots, and the cylinder is represented by gray surfaces

In figure 2.6, a comparison of the instantaneous bubble distribution on the x-z plane passing through the plume centerline between the simulation and the experiment is shown. The bubbles do not move straight upward, but their motion shifts toward the plume centerline. The bubbles in the experiment are more attracted to the centerline than the bubbles in the simulation, and there is a greater dispersion of bubbles in the experiment. The possible causes of this discrepancy are explained by the difference in bubble release between the simulation and the experiment, as well as the limitation of simulation time. Under the initial condition, the liquid phase in the simulation is totally quiescent, while the liquid phase of the experiment is not quiescent. Moreover, the bubbles in the simulation are equally distributed at the annulus and then released

regularly over time. In the experiment, the bubbles are distributed in groups and are not released regularly over time. Therefore, the rising of bubbles is also performed by bubble groups. The movement of bubbles or the buoyancy flux generates the fluid shear layers. In the simulation, these shear layers are symmetric with respect to the plume centerline in the early development stage of the flow. In the experiment, these shear layers are not symmetric and are not generated equally and regularly. The interaction of irregular fluid shear layers leads to the generation of eddies on the inside of the bubble plume. These eddies attract a greater number of bubbles toward the centerline and disperse them. In addition, the maximum simulation time, $t^* = 32.8$, is inadequate to observe completely the developed stage of the bubble plume.

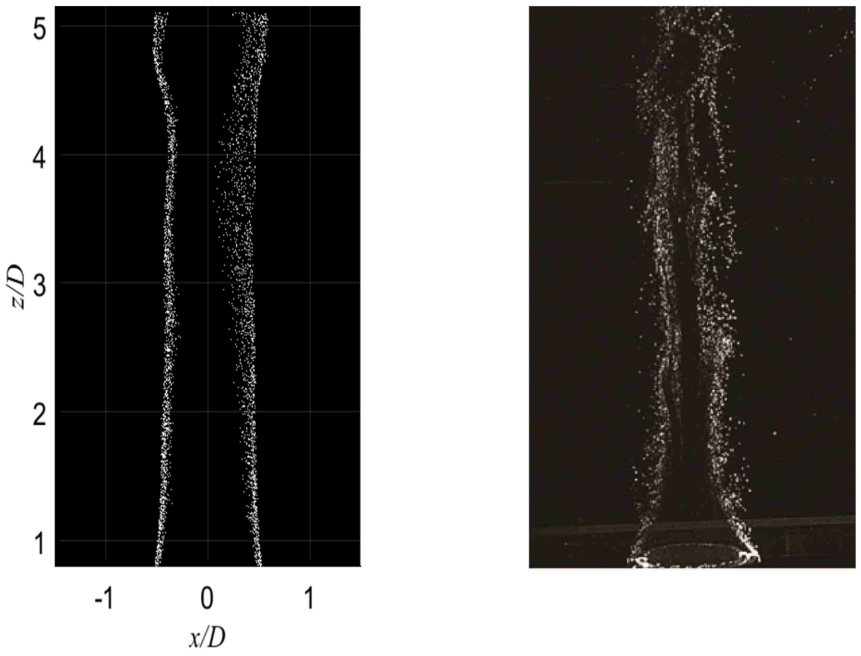

Figure 2.6: Comparison between simulated and experimental instantaneous bubble distribution on x-z plane passing through plume centerline

In Figure 2.7, the time evolution of the iso-surface of ω_z and three-dimensional bubble distribution are presented. At time $t^* = 8.3$ and 9.6, the three-dimensional vortical flow starts to develop, in which pairs of positive and negative vortex tubes with green and blue surfaces, respectively, interleave sequentially. These interleaved vortex tubes twist together slightly at $t^* = 11, 13.8$ and significantly at $t^* = 16.5, 18.8$. The vortical flow is fully developed from this time. Ultimately, the three-dimensional vortical flow spreads out across the computational domain, as can be seen at $t^* = 24.8$ and 32.8.

In Figure 2.8, the bubble distribution and vorticity ω_y with time variation on the x-z plane are presented. After the early quasi-stable stage from the beginning to $t^* = 5.5$, the bubble plume starts to behave in a meandering fashion, as can be seen at $t^* = 8.3$

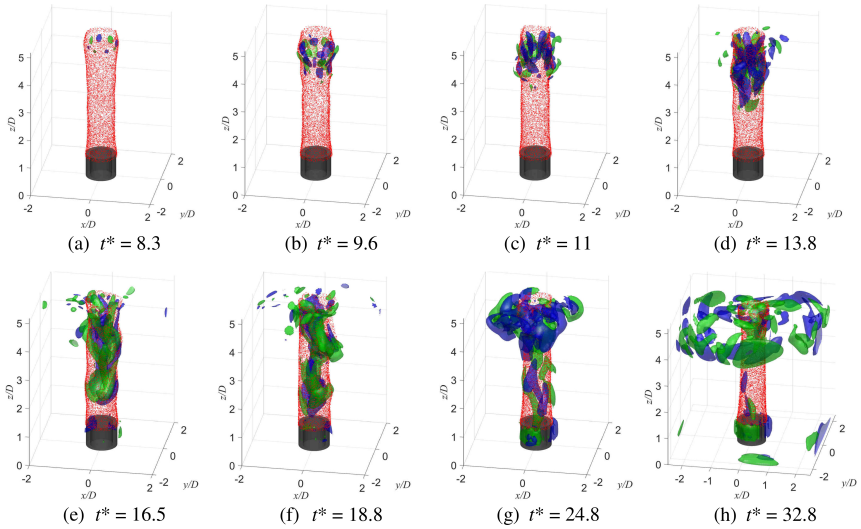

Figure 2.7: Time evolution of iso-surface of ω_z. $\omega_z/(u_t/D) = \pm 0.9$ is represented by green and blue surfaces, respectively, bubble distribution is represented by red dots, and the cylinder is represented by gray surfaces

due to the primary instability. This primary instability seems to closely resemble that in thermal plumes (Alam and Arakeri, 1993). The meandering phenomenon is observed clearly at times $t^* = 11$ and 13.8. The vorticity ω_y is generated surrounding bubble plume. Various eddies known as vortex rings are formed as a consequence of the inhomogeneous distribution of the bubble plume, as can be seen at $t^* = 11, 13.8$. The symmetry of the bubble plume and the vorticity distribution disappear at $t^* = 13.8$ and 16.5. The bubbly flow is fully developed from $t^* = 18.8$.

2.4.3 Vector fluid velocity field

Figure 2.9 shows the time evolution of the vector liquid velocity and bubble distribution at the x-z plane passing through the plume centerline. As explained above, the vortex structure of flow is composed of vortex rings of various scales. The formation and deformation of these vortex rings are expressed in detail here. At $t^* = 5.5$, the bubble plume is quasi-stable, and the initial development of two vortex rings inside and outside the plume is observed at the fluid surface. Thereafter, the strength of these vortex rings increases, as can be seen at $t^* = 8.3$. The outer vortex ring enlarges along with the horizontal direction, while the inner vortex ring moves downward at $t^* = 8.3$ and 9.6. Vortex rings of various scales are formed along the bubble plume because of the inhomogeneous bubble distribution. The bubble plume behaves in a meandering and swaying fashion in this period. Moreover, at $t^* = 9.6$, two tandem vortex rings are observed inside the bubble plume near the fluid surface. The movement of tandem vortex rings is directed downward by their own self-induced velocity, with the stronger vortex ring above the weaker vortex ring. The stronger vortex ring rapidly catches up with the weaker vortex ring and then interacts with it, as can be seen at $t^* = 11$. These two vortex rings penetrate each other, resulting in the generation of a long deformed eddy, as can be seen at $t^* = 11$ and 13.8.

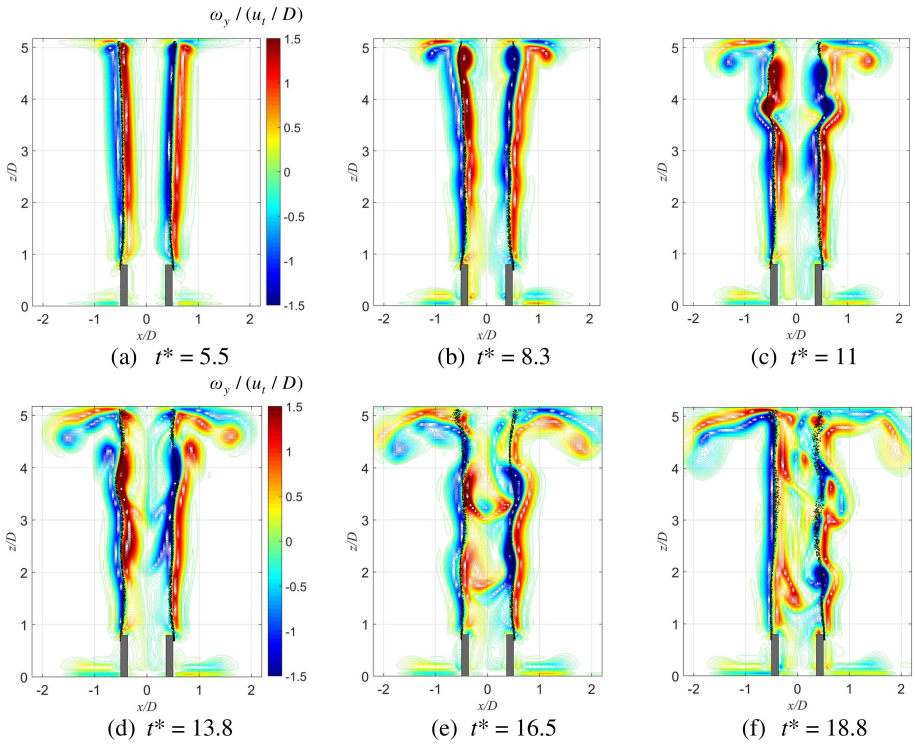

Figure 2.8: Time evolution of vorticity field ω_y and bubble distribution represented by black dots on x-z plane passing through plume centerline, and cross section of the cylinder displayed by gray areas

The symmetry with respect to the centerline of the vortex rings and bubble plume is lost during this time evolution. From $t^* = 16.5$, the appearance of a three-dimensional vortical flow formed by various eddies both inside and outside the bubble plume is observed. Eventually, an upward velocity inside the bubble plume of the developed flow is illustrated at $t^* = 24.8$ and 32.8, as pointed out in an experimental investigation as well (Uchiyama and Kusamichi, 2013).

2.4.4 Time-average and time variation of liquid velocity

Figure 2.10 shows the time-averaged vertical liquid velocity denoted as $< w >$ and computed from $t^* = 5.5$ to 9.6 in the transition stage of the annular bubble plume. As can be seen in this figure, the flow velocity is along the downward direction at the center of the plume. The liquid velocity peaks at the position of bubble rise, and it decreases gradually outside the bubble plume. The maximum velocity is observed at the values $x/D = 0.5$ and $y/D = 0.5$. The liquid velocity at three heights along both horizontal directions x and y is smaller than the terminal velocity $u_t = 16$ mm/s of a single bubble of diameter $d_b = 0.2$ mm rising in the quiescent liquid.

Figure 2.11 shows the effect of grid resolution on the calculation results. The vertical liquid velocity profiles along horizontal lines passing through the centerline of the bubble plume at three distinct heights with two grid resolutions of $80 \times 80 \times 80$ and $100 \times 100 \times 100$

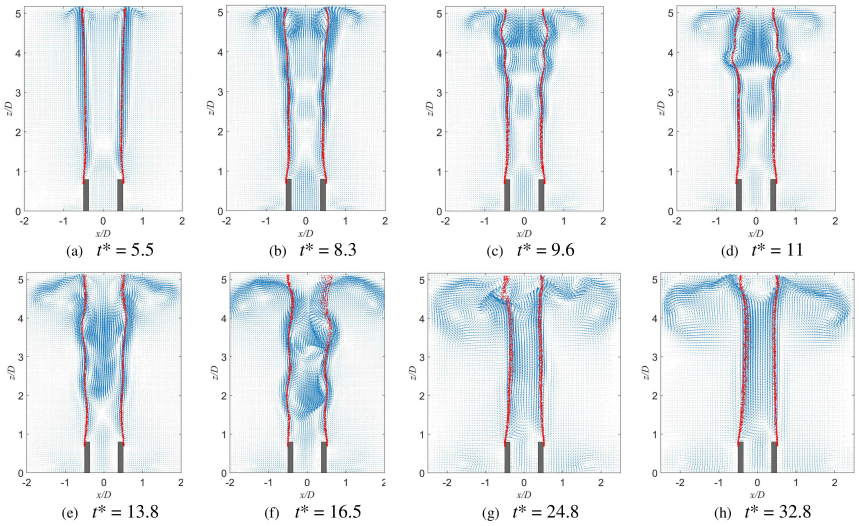

Figure 2.9: Time evolution of vector liquid velocity and bubble distribution at x-z plane passing through plume centerline. Bubble distribution is represented by red dots, and cross-section of the cylinder is displayed by gray areas

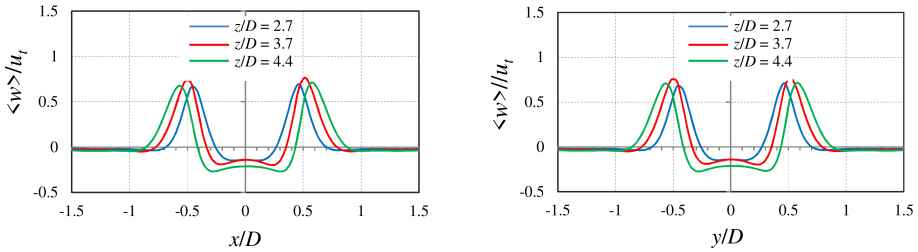

Figure 2.10: Profiles of time-averaged vertical liquid velocity (averaged from $t^* = 5.5$ to 9.6 in a transition stage) on horizontal lines passing through plume centerline at various heights shown in the legend

cells are compared. The liquid velocity profiles calculated using both grid resolutions are similar; therefore, the present simulation converges at $100 \times 100 \times 100$ cells.

It is known that at a sufficiently high bubble flow rate in the transition stage, the plane bubble plume meanders along a vertical plane passing through an injection line, while the annular bubble plume behaves in a meandering fashion along a vertical cylinder surface passing through an injection annulus. Therefore, the velocity profiles of the annular bubble plume in this stage are compared with those of the plane bubble plume. Figure 2.12 shows a comparison between the time-averaged vertical liquid velocity profiles along both horizontal directions x, y passing through the plume centerline and Gaussian distributions that have been fitted to the peaks. The liquid velocity is averaged from $t^* = 5.5$ to 9.6 in the transition stage of the flow. The vertical liquid velocity profiles are scaled with their corresponding maximum velocity and have been shifted horizontally so that the profile peaks line up. Outside the bubble plume, the liquid profiles are similar to the theoretically predicted values (Milgram, 1983) and the simulation results (Uchiyama

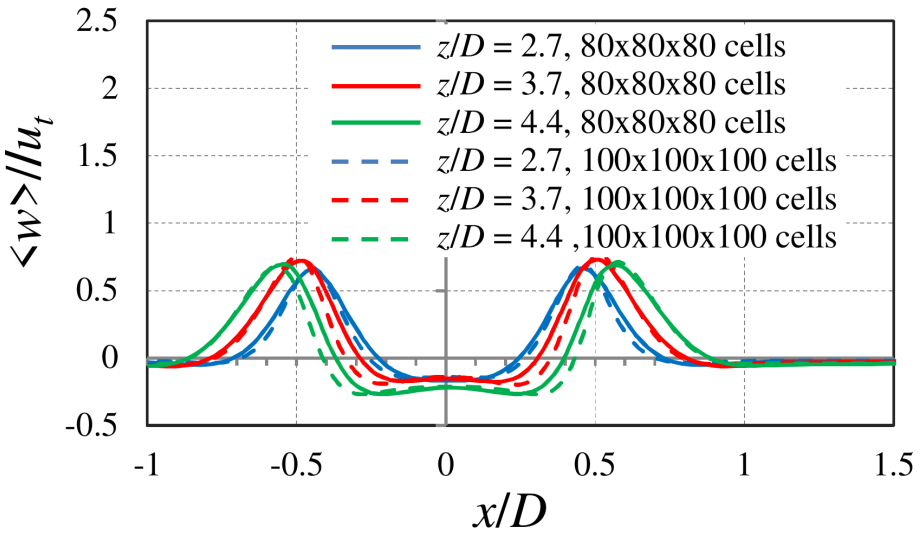

Figure 2.11: Effect of grid resolution on vertical liquid velocity profiles (averaged from $t^* = 5.5$ to 9.6 in a transition stage) on horizontal lines passing through plume centerline at various heights shown in the legend

and Degawa, 2008) for a plane plume. The Gaussian function plotted in the figure is $W(r) = exp(-(r - r_0)^2/(\sqrt{0.025})^2)$. Inside the bubble plume, the liquid profiles are lower than the Gaussian distribution and this is ascribed to the fact that the bubble plume is annular rather than plane. The distributions of vertical liquid velocity are similar on both horizontal lines.

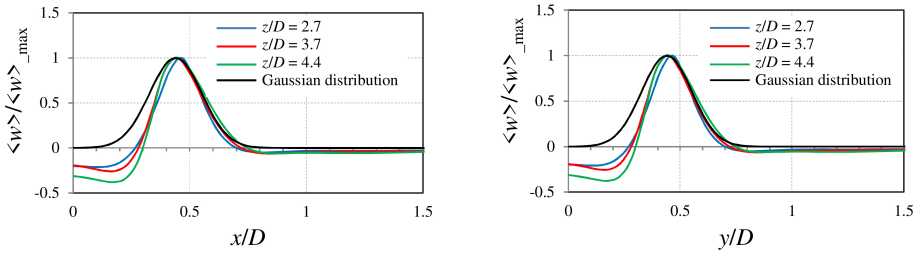

Figure 2.12: Profiles of time-averaged vertical liquid velocity (averaged from $t^* = 5.5$ to 9.6 in a transition stage) on horizontal lines passing through plume centerline at the various heights shown in the legend. A Gaussian distribution is shown for comparison. $< w >_{max}$ is the maximum value of $< w >$

Fluctuation of the vertical liquid velocity, w, with time evolution is measured at six points, as shown in figure 2.13. The points A_1, A_2, and A_3 lie on a vertical (z-direction) line pass through the injection annulus. At the heights $z/D = 3.7$ and 4.4, after increasing from the beginning to $t^* = 7.5$, the vertical liquid velocity at points A_2, A_3 fluctuate strongly in the time range of $t^* = 7.5$–15. This is ascribed to the effect of the meandering motion of the bubble plume. The vertical fluid velocity fluctuates following the behavior of the bubble plume. A positive value of the vertical velocity at these points is observed from $t^* = 15$, and this fact is caused by the bubbly flow developed in this period. By

contrast, the vertical liquid velocity at point A_1 increases from the outset until $t^* = 7.5$, and then, it fluctuates slightly. At this location near the region where the bubbles were released, the vertical liquid velocity seems to be less affected by the meandering motion of the bubble plume. The points B_1, B_2, and B_3 are located on the centerline of the bubble plume at three distinct heights. The vertical liquid velocities at these points are negative from $t^* = 5$ to 20, as explained by a transition effect, before the momentum flux has diffused into the inner part of the plume, and generated a quasi-steady developed flow. These values become positive and fluctuate slightly in the developed stage of the flow.

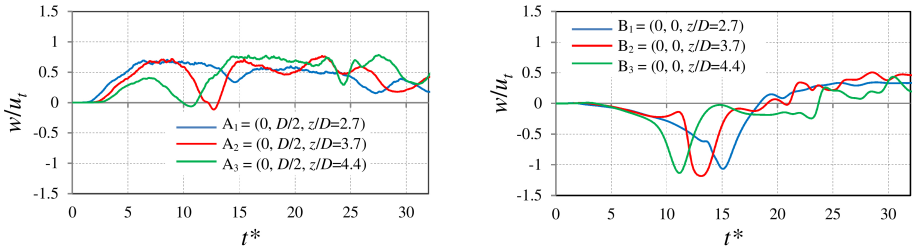

(a) Points on a vertical line passing through the injection annulus

(b) Points on the bubble plume centerline

Figure 2.13: Time variation of vertical (z-direction) liquid velocity at six points shown in the legend

In Fig. 2.14, the fluctuation of horizontal liquid velocity, v, at six points is presented. At points A_2 and A_3, the horizontal liquid velocities fluctuate more strongly than that at point A_1. In addition, the horizontal liquid velocity at points A_1, A_2, and A_3 fluctuate more strongly than those at the points on the bubble plume centerline.

Figure 2.15 shows the RMS value of liquid flow on the horizontal lines passing through the plume centerline at three distinct heights. Herein, the RMS value of w and $< w >$ are the root mean square and time-averaged values of vertical liquid velocity, respectively. The maximum of the RMS of w is observed at $x/D = 0.5$ and $y/D = 0.5$, which correspond to the position at which the bubbles rise. The RMS of w inside the bubble plume is higher than that outside the bubble plume because of the significant effect of the annular bubble plume on liquid flow inside the bubble plume. In addition, the RMS of w at $z/D = 2.7$ is lower than at $z/D = 3.7$ and 4.4, and this can be explained by the fact of that the flow near the bubble release region is affected to a lesser extent.

Figure 2.16 shows a comparison of the distribution of time-averaged vertical liquid velocity, $< w >$, on the horizontal line passing through the plume centerline between the simulation and the experimental results (Uchiyama and Kusamichi, 2013). The vertical liquid velocity in the simulation is computed by averaging from $t^* = 20$ to 32 when the bubbly flow is fully developed. The vertical liquid velocity is calculated in this period because the experiment data contains estimates for the fully developed flow stage. The vertical liquid velocity obtained in the simulation does not agree well with the experimental

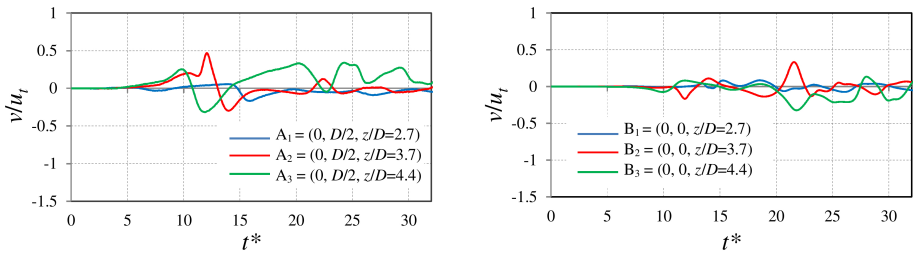

(a) Points on a vertical line passing through the injection annulus

(b) Points on bubble plume centerline

Figure 2.14: Time variation of horizontal (y-direction) liquid velocity at six points shown in the legend

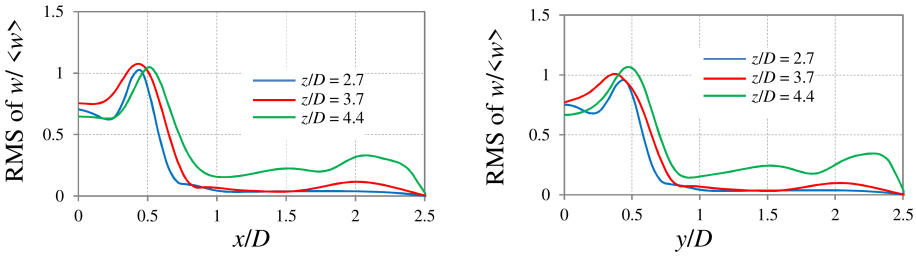

Figure 2.15: Profiles of RMS of vertical liquid velocity on horizontal lines passing through plume centerline at the various heights shown in the legend

values. The maximum upward liquid velocity in the experiment is observed at the bubble plume centerline, while that in the simulation is observed at $x/D = 0.25$. This could be explained by the fact that the flow has not fully developed yet, as can be seen in Fig. 2.13 in which there would have been a slow increase in centerline velocity if the simulation had been further calculated. However, the tendency of the flow in the present simulation agrees with the experiment. At the center of the bubble plume, in both the simulation and the experiment, the upward liquid velocity at $z/D = 3.7$ is higher than those at $z/D = 2.7$ and 4.4. A gradual decrease in liquid velocity from the rise position of the bubbles to far outside the bubble plume is seen in both the simulation and the experiment.

2.4.5 A comparison of bubble velocity with liquid velocity and terminal velocity of a single bubble

A comparison between the instantaneous rise velocity of the two phases is visualized at cross sections $z/D = 2.7, 3.7$, and 4.4 at the typical times $t^* = 9.6$ and 18.8 as shown in figure 2.17. At time $t^* = 9.6$, the bubble plume is observed to be a state of meandering motion. The liquid rise velocity is not turbulent at the three heights, as can be seen in the plots in the top row of the figure. However, at times $t^* = 18.8$, the liquid rise velocity fluctuates slightly at $z/D = 3.7$ and significantly at $z/D = 4.4$. The bubble rise velocity is always higher than the liquid rise velocity at three distinct heights and two specific times.

The ratio of the bubble rise velocity to the terminal bubble velocity is shown in figure 2.18. The bubble diameter in the present simulation is 0.15–0.25 mm. The bubble

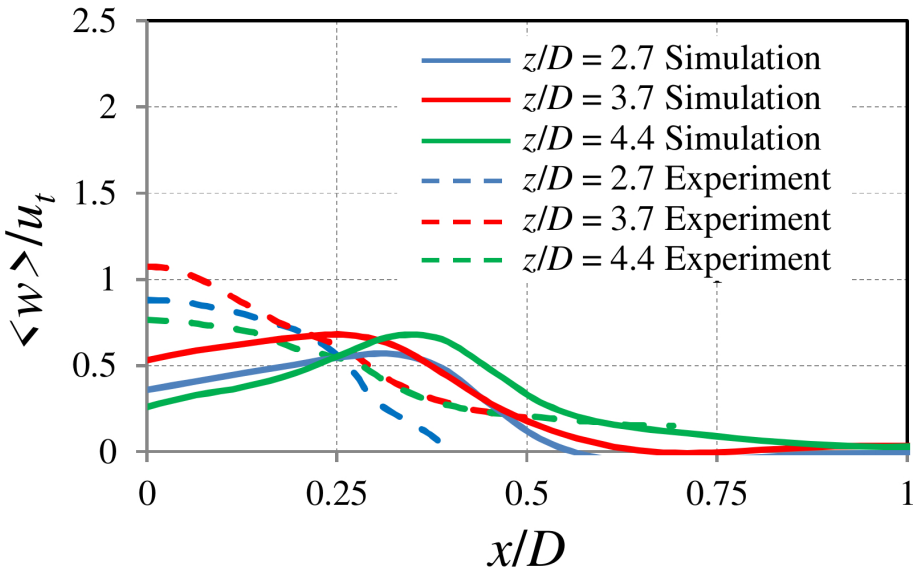

Figure 2.16: Comparison of time-averaged vertical liquid velocity profiles (averaged from $t^* = 20$ to 32 in a developed stage) on the horizontal lines passing through plume centerline at the various heights shown in the legend between simulation results and experimental measurements (Uchiyama and Kusamichi, 2013)

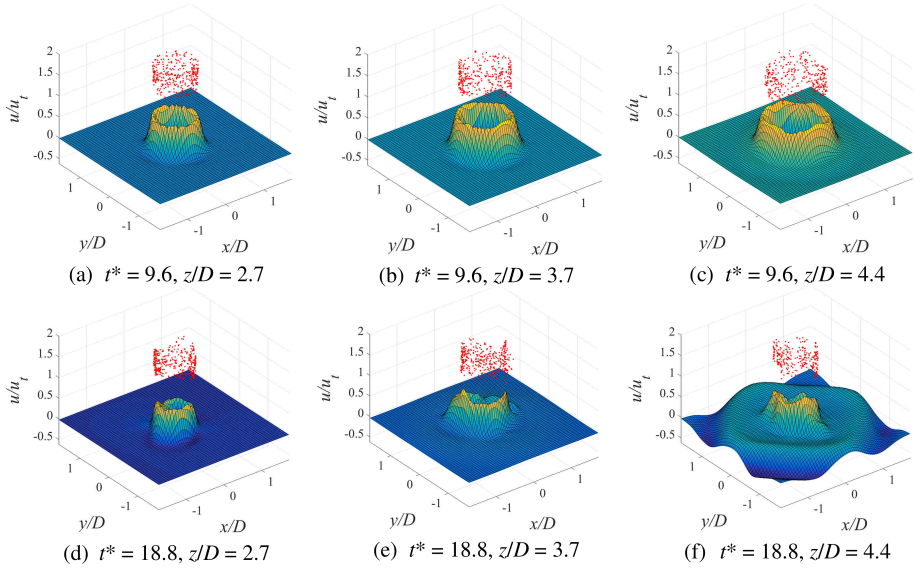

Figure 2.17: Comparison of instantaneous rise velocity between liquid and gas phases. The bubble rise velocity is visualized as the height of red dot position, and liquid rise velocity is visualized as curved surface. These velocities are investigated at cross sections $z/D = 2.7, 3.7$, and 4.4 at times $t^* = 9.6$ and 18.8. The u_t is the terminal velocity of a single bubble of diameter $d_b = 0.2$ mm rising in quiescent liquid

velocity is investigated in two flow states, including transition state at $t^* = 9.6$ and developed state at $t^* = 18.8$. At the height $z/D = 1$, the ratio of bubble rise velocity to u_t varies from 1 to 1.5 units at both instantaneous times $t^* = 9.6$ and 18.8. The bubbles with $d_b = 0.2$ mm move upward with a ratio of more than one unit. The

bubbles near the release region are less affected by bubbly flow and rise as isolated single bubbles in quiescent water. When these bubbles get to a certain height, they are affected significantly by liquid flow induced by the previous bubbles. At time $t^* = 9.6$ and height $z/D = 3.7, 4.4$, the ratio is higher than 1.5 units because of the effect of vertical upward liquid flow. Nevertheless, at $t^* = 18.8$ and height $z/D = 3.7, 4.4$, the ratio varies from 1 to 2 units, and there are even a few bubbles with ratios higher than 2 units. This is due to the effect of the appearance of three-dimensional flow in this period. This observation agrees with the experimental result obtained by Uchiyama and Kusamichi (2013), and the simulation result obtained by Uchiyama and Degawa (2008). With $z/D \geq 2$ the time-averaged bubble velocity is higher than the terminal velocity. The ratio between bubble velocity and terminal velocity is found to be in the range of 1.2–2 (Uchiyama and Degawa, 2008). The present investigation uses instantaneous time to offer greater detail about the effects of each flow development stage on bubble velocity.

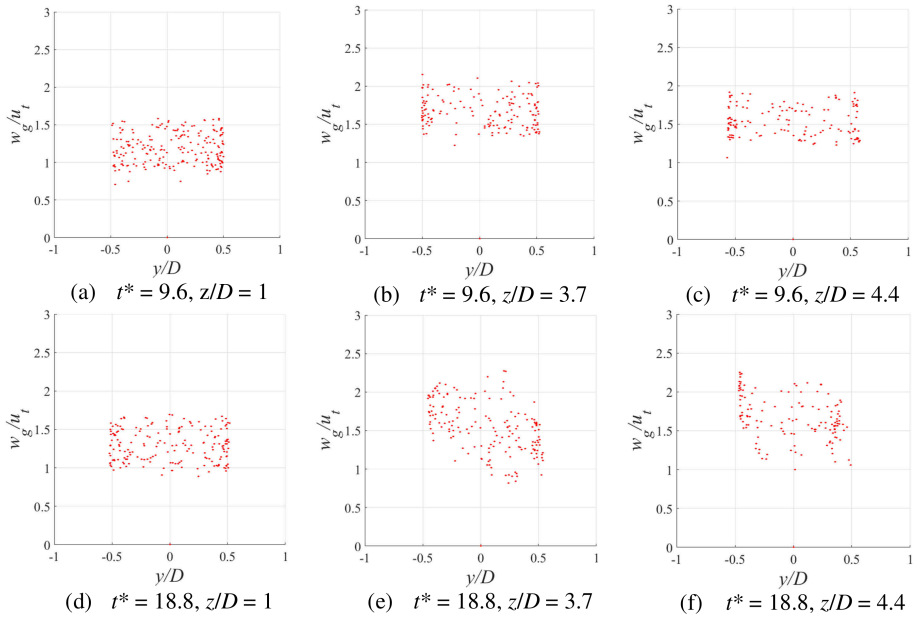

Figure 2.18: Ratio of bubble rise velocity w_g to terminal velocity u_t of a single bubble of diameter $d_b = 0.2$ mm in quiescent water. The ratio value of w_g/u_t is visualized by the height of red dot position. The bubble rise velocity is investigated at cross sections $z/D = 1, 3.7$, and 4.4 at times $t^* = 9.6$ and 18.8 and these cross sections are viewed from the x-direction (cross-sections degenerate into lines)

Figure 2.19 shows a comparison between the slip velocity and the terminal rise velocity of a single bubble in quiescent water. Generally, the slip velocity is always smaller than the terminal rise velocity. During the transition stage of the flow, as can be seen at $t^* = 9.6$, the slip velocity is symmetric with respect to the plume centerline. In the developed stage of the flow, as can be seen at $t^* = 18.8$, the slip velocity is not symmetric and seems to display random effects caused by turbulence. This is consistent with the developmental characteristics of the vortical flow, as observed above.

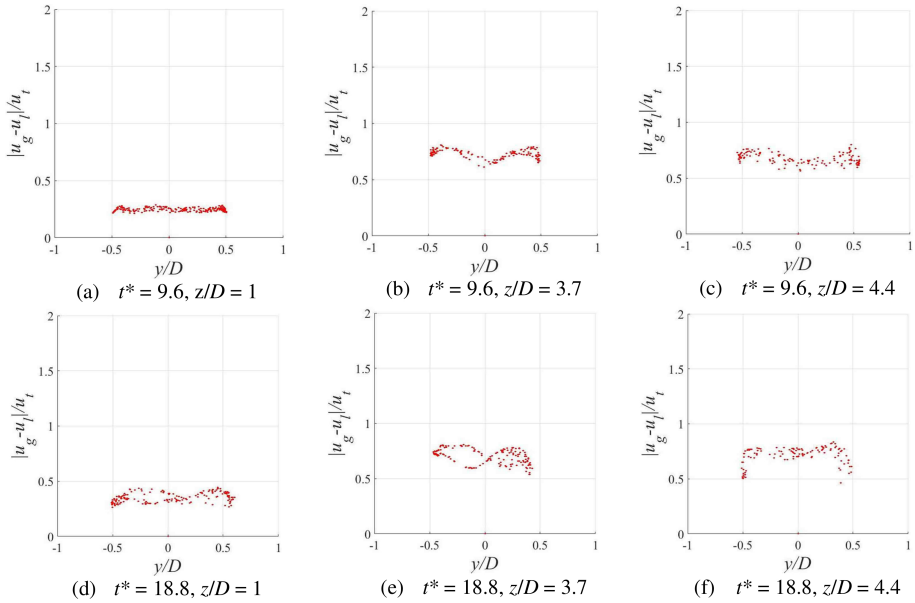

Figure 2.19: Ratio of slip velocity $|u_g - u_l|$ to the terminal velocity u_t of a single bubble of diameter $d_b = 0.2$ mm in quiescent water. The ratio value of $|u_g - u_l|/u_t$ is visualized by the height of red dot position. The slip velocity is investigated at cross sections $z/D = 1, 3.7$, and 4.4 at times $t^* = 9.6$ and 18.8 and these cross sections are viewed from the x-direction (cross-sections degenerate into lines)

2.4.6 Gas volume fraction distribution

Figure 2.20 shows the time-averaged gas volume fraction distribution on the horizontal line passing through the plume centerline. The maximum value of the gas volume fraction is obtained at height $z/D = 2.7$, while the minimum value is obtained at $z/D = 3.7$. In addition, the width of the gas volume fraction profile at height of $z/D = 3.7$ is greater than that at the height of $z/D = 2.7$. This is explained by the meandering motion of the bubble plume, leading to strong spreading of the bubble distribution in the horizontal direction at height of $z/D = 3.7$. In the present simulation, the gas volume fraction is less than 0.0003.

2.5 Conclusions

The evolution of an annular bubble plume was numerically simulated by using the semi-L–L approach. The approach is composed of the vortex-in-cell method to solve for the liquid phase and a Lagrangian description of the gas phase. The characteristics of the bubbles and induced-liquid flow for the annular bubble plume are remarked as follows:

(1) Vortex structure of the flow, such as vortex rings of various scales is formed and then deformed. The formation of these vortex rings was found to be a consequence of the inhomogeneous bubble distribution and the effect of the fluid surface. The interaction, expansion of these vortex rings, and effect of the bubble plume lead to their deformation.

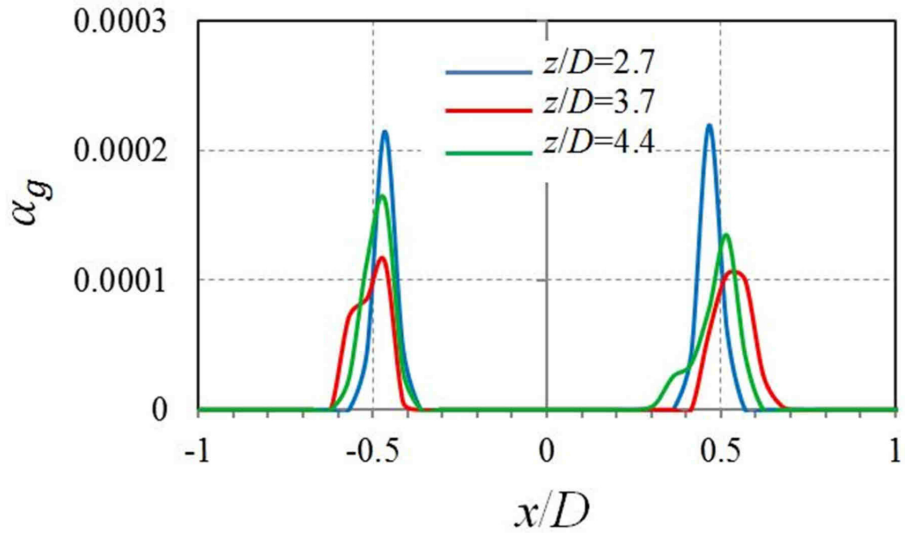

Figure 2.20: Profiles of time-averaged gas volume fraction on the horizontal lines passing through the plume centerline at the various heights shown in the legend

(2) Bubbly flow is stable in the early stage of the flow, and then it rapidly reaches the transition stage with meandering motion of the bubble plume owing to primary instability. The annular bubble plume and vortex structures are symmetric with respect to the plume centerline in this period. Subsequently, the three-dimensional vortical flow is observed, and the symmetry of bubble plume and the vortex structure disappears.

(3) Time-averaged vertical liquid velocity on the horizontal lines passing through the plume centerline at three distinct heights was measured. In the transition stage of the flow, the liquid velocity profiles were close to the theoretically predicted profiles (Milgram, 1983), and they agreed with the existing numerical results (Uchiyama and Degawa, 2008). In the fully developed stage of the flow, the time-averaged vertical liquid velocity in the present simulation does not agree well with the corresponding experimental measurements. However, the tendencies of the flow, such as the meandering motion of the bubble plume, and upward velocity inside the bubble plume between the simulation and the experiment were found to be similar.

(4) The bubble rise velocity is always higher than the liquid rise velocity. The time-averaged vertical liquid velocity is lower than the terminal bubble velocity at the bubble flow rate of Q = 4.1 mm^3/s. The bubble rise velocity is higher than the bubble terminal velocity because of the effect of upward liquid flow induced by the bubbles. This observation agrees with the existing both experimental and simulation results. The bubble velocity is affected significantly by the height of evolution and the development stage of the flow. Near the release region, the bubbles rise as a single bubble in the quiescent liquid. In the transition state, the ratio between bubble velocity and terminal velocity ranges from 1.5 to 2 units. However, this ratio is in the range of 1 to 2 units

when the flow is fully developed. This change ascribed to the effect of fully developed flow on bubble velocity.

(5) Gas volume fraction in the present simulation was less than 0.0003. The time-averaged gas volume fraction near the bubble release region was higher than that in the region with meandering motion. However, the width of gas volume fraction distribution near the bubble release region was smaller. This was caused by spreading of bubbles in the horizontal direction, in which the meandering motion of the bubble plume appears.

Nomenclatures

A_b	Area of a circle of diameter d_b
C_D, C_L, C_V	Drag, lift, and virtual mass coefficients of the bubble, respectively
d	Signed distance from fluid–solid interface to grid node
d_b	Bubble diameter
D	Outer diameter of the cylinder
$\boldsymbol{F}_B, \boldsymbol{F}_D, \boldsymbol{F}_L, \boldsymbol{F}_{VM}, \boldsymbol{F}_P$	Buoyancy, drag, lift, virtual mass, and pressure gradient forces, respectively
$\boldsymbol{g}$	Gravitational acceleration
L_x, L_y, L_z	Tank dimensions
p	Pressure
Q	Bubble flow rate
Q	Vortex identification
Re_b	Reynolds number of the bubble
S, F	Solid and fluid regions, respectively
t	time
t^*	Non-dimensional time
$\boldsymbol{u}_l, \boldsymbol{u}_g$	Liquid and gas velocity, respectively
$\boldsymbol{u}_S$	Solid velocity
$\boldsymbol{u}_\lambda$	Penalization velocity
u_t	Terminal velocity
V_b	Bubble volume
$W(x)$	Redistribution function of vorticity
W_α	Redistribution function of gas volume fraction
$\boldsymbol{x}, \boldsymbol{x}_p, \boldsymbol{x}_q$	Coordinate, vortex-particle location, and grid node location, respectively
α_l, α_g	Volume fraction of liquid and gas phases, respectively
ρ_L, ρ_g	Density of liquid and gas phases, respectively
β	Density ratio between gas and liquid phases
$\boldsymbol{\omega}$	Vector vorticity of liquid
$\omega_x, \omega_y, \omega_z$	Components of $\boldsymbol{\omega}$
$\boldsymbol{\omega}_\lambda$	Penalization vorticity
ϕ	Scalar potential

$\boldsymbol{\psi}$	Vector potential
ψ_x, ψ_y, ψ_z	Components of $\boldsymbol{\psi}$
ν_l	Liquid kinematic viscosity
λ	Penalization parameter
χ_S	Solid-mask function
$\Delta x, \Delta y, \Delta z$	Grid widths
Δt	Time-increment
S, Ω	Strain and rotation rate tensors, respectively
τ_b	Bubble time-scale

Table 2.1: Nomenclature

Chapter 3

Numerical simulation of the interaction between a vortex ring and a bubble plume

3.1 Introduction

Bubbly flows are observed in a wide variety of engineering applications such as heat exchangers, fermentation devices, chemical reactors, and waste treatment systems (Fraga et al., 2016). A comprehensive understanding of the interaction between the gas and liquid phases is important for improving designs and controlling engineering devices related to bubbly two-phase flows. It has been reported that bubble motion is mainly governed by the vortical flows; hence, the important canonical problem of the interaction between the bubbles and the vortical flow is often used to discover the characteristics of bubbly two-phase flows. Vortical flows can be idealized, such as Taylor–Green vortex (Druzhinin and Elghobashi, 1998; Ferrante and Elghobashi, 2007), Taylor–Couette (Chouippe et al., 2014), Lamb–Oseen vortex (Oweis et al., 2005), and Taylor vortex (Deng et al., 2006), and natural phenomena of fluid dynamics of vortex rings(Bergdorf et al., 2007; Sridhar and Katz, 1999; Finn et al., 2011; Cihonski et al., 2013; Wang et al., 2013; Uchiyama and Yoshii, 2015a; Uchiyama and Kusamichi, 2013).

The vortex ring, one of the archetypal structures of fluid-dynamic phenomena (Bergdorf et al., 2007), moves by its own self-induced velocity. When it moves, it can transport and entrain the bubbles surrounding it. The bubble entrainment into the vortex ring deforms the ring's structure. Sridhar and Katz (1999) conducted an experimental investigation of the effects of five entrained bubbles upon this structure. The vortex ring was launched perpendicular to the bubble motion, and bubble diameter varied in the range of 0.25–0.75 mm. Sridhar and Katz demonstrated that, at very low gas volume fractions, the entrained bubbles can significantly alter the vortex structure. The distortion of the vortex core is maximal when the bubbles settle. The small bubbles settle close to the core center, whereas the larger bubbles settle farther away but still significantly distort this core. Vortex distortion is explained as a result of the change in liquid momentum owing to bubble entrainment. When the bubbles move to the central side of the vortex ring, the original circular shape of the vortex core is regained. Moreover, the vortex-ring strength remains unchanged over the full-time evolution.

Finn et al. (2011) numerically simulated the two-dimensional entrainment of eight bubbles in a vortex tube, and the simulation conditions were set similar to the experimental investigation by Sridhar and Katz (1999). The bubble motion captured in the simulation was similar to that measured experimentally. The vortex distortion was clarified through measurements such as vortex asymmetry, core fragmentation, peak vorticity, and angular-momentum-decay rate. Continuing the work of Finn et al. (2011), Cihonski et al. (2013) numerically simulated full three-dimensional bubble entrainment into the vortex ring. They utilized two approaches to modeling the effects of the bubbles upon the vortex ring. In the first approach, the bubble effects on the flow were modeled based on momentum point sources calculated using the reaction forces of the fluid acting upon the bubbles. The gas volume fraction is not considered. In the second approach, the gas volume fraction was added to the momentum point sources to account for modification of the liquid continuity and momentum equations. Cihonski et al. (2013) proved that the second approach performed well in reproducing the experimental observation of both the gas and liquid phases.

Wang et al. (2013) numerically investigated the interaction between a vortex ring and a planar bubble plume. The vortex ring was launched at a Reynolds number of $Re_\Gamma = 5,200$, perpendicular to the bubble-rise direction. Most bubbles were entrained into the lower part of the vortex core, while some rose and were gradually entrained in the upper part. As a result of this irregular bubble entrainment, the vorticity value in the lower part of the vortex core decreased more than that in the upper part. The upper part of the vortex core moved faster than the lower part, and the entrained bubbles escaped, mostly accumulating in the wake of the vortex ring. The entrained-bubble effects upon the vortex-ring circulation were small. The distance of bubble transport induced by this vortex ring was inversely proportional to the bubble diameter.

The features of particle transport by a vortex ring have been used in various engineering applications. For example, in olfactory-display engineering, a vortex ring is used to transport a clump of scented air to the observers nose to determine the compound odor, as in the investigation of Yanagida et al. (2004). Domon et al. (2000) conducted an experimental investigation of the relationship between particles with a specific gravity and the feasibility of transporting these particles by a vortex ring. They reported that particles with specific gravities larger than unity will be scattered out of the vortex ring, owing to centrifugal forces. However, if their specific gravities are less than unity, they will be trapped in the vortex core and carried over long distances. Yagami and Uchiyama (2011) numerically simulated the transport of solid particles by a vortex ring at $Re_\Gamma = 2,600$. They showed that the particle transport depended significantly upon the particles's Stokes number (St). The solid particles with $St = 0.01$ were transported, while those with $St = 1$ were not. The transported particles were distributed around the vortex ring and formed a dome.

Generally, heavy particles are entrained into the region of low-vorticity-magnitude values, while light particles accumulate in the region of high-vorticity-magnitude values (Druzhinin and Elghobashi, 1998; Ferrante and Elghobashi, 2007). Therefore, the interaction between a vortical flow and light particles cannot be inferred from the results with heavy particles. (Uchiyama and Yoshii, 2015a) numerically simulated the entrainment and transport of the gas bubbles by a vortex ring at $Re_\Gamma = 400, 500$, and 600. The total volume of the entrained bubbles in the vortex core is higher for lower values of Re_Γ. Because of the slower convection, the vortex ring remains inside the bubble cluster over a longer time, and meaning that more bubbles are entrained in the vortex core. The entrained bubble affects the vortex-core strengthen when Re_Γ decreases. The vortex-ring diameter increases along with its convection, and this increment becomes greater as the gas volume fraction increases.

Uchiyama and Kusamichi (2013) experimentally examined the interaction of the bubbles with a vortex ring launched vertically upward at $Re_\Gamma = 8063$ into a bubble plume. They reported that bubbles are spirally entrained into the vortex ring just after its launch. The bubbles moving to the rear of vortex ring are left behind when the vortex ring reaches a certain height. The gas volume fraction distribution along the horizontal line passing through the vortex ring's center increases until a certain displacement is achieved, after which reduction occurs. The core is deformed with vortex-ring convection, and vortex-ring circulation is reduced by the entrained bubbles.

However, the characteristics of the interaction between the vortex ring and the bubble plume have not been fully clarified. The unknown characteristics of this interaction are as follows: (1) the efficiency of bubble transport by the vortex ring; (2) the mechanism of bubble motion when they are initialized at and near the core center; and (3) the effects of entrained bubbles upon the azimuthal instability of the vortex ring. Therefore, this investigation will throw some light on the problem of the interaction between the vortex ring and the bubble plume using numerical simulations. The initial conditions in the simulation are set similar to those in the experimental investigation (Uchiyama and Kusamichi, 2013). The present simulation is verified by comparing the simulation measurements, such as the vortex ring displacement, liquid velocity distribution, and bubble entrainment, to the corresponding experimental measurements. The efficiency of bubble transport is investigated by calculating the total bubble volume in control volumes and the bubble-transportation distance. The bubble dynamics are investigated by calculating the bubble trajectory, bubble velocity, liquid vorticity at bubble location, and bubble azimuthal motion. The effects of entrained bubbles upon the vortex structure are clarified by investigating correlations between the gas volume fraction and liquid vorticity, and between the gas volume fraction and the vortex deformation intensity. Moreover, the liquid velocity, Q criteria, and vortex ring circulation are investigated. The

effects of entrained bubbles upon the ring's azimuthal instability are explained through visualization of the structure of the vorticity component, ω_z, and the energy spectrum of ω_z.

In this chapter, the semi-Lagrangian–Lagrangian approach is used to investigate the interaction between the vortex ring and the bubble plume. The remainder of this chapter is organized as follows: a discussion of the results is given in section 3.2; and our conclusions are given in section 3.3.

3.2 Result and discussion

3.2.1 Simulation condition

The simulation conditions are set as the experimental conditions in (Uchiyama and Kusamichi, 2013). Figure 3.1 shows the configuration of a vortex ring launched into a bubble plume. An empty cylinder with an outer diameter of $D_0 = 58$ mm, an inner diameter of $0.74D_0$, and a height of $0.8D_0$ is placed at the bottom of a tank. The bubbles located around the outer surface of the cylinder are released from a height of $h = 0.7D_0$. Under buoyancy, the bubbles rise and induce a water flow around them. The dimensions of the tank are $4.14D_0 \times 4.14D_0 \times 5.16D_0$ divided into $240 \times 240 \times 300$ cubic cells. The value of the time step Δt in the simulation is referenced from a numerical investigation of annular bubble plume and is equivalent to the time scale of the bubble calculated using the formula $\tau_b = d_b^2/(36\nu_l)$. The non-dimensional time step $\Gamma_0 \Delta t/(D_0/2)^2$ is set to 0.0048. The bubble diameter is generated randomly within a range of 0.15–0.25 mm. The bubble diameter is similar to the experimental value (Uchiyama and Kusamichi, 2013), and it satisfies the assumptions mentioned in section 2.2.1. The release location of the bubbles is selected randomly from the outer cylinder surface. The bubbles are released with zero velocity. The number of bubbles released satisfies the bubble-flow rate, Q = 4.1 mm^3/s. First, the bubbles are released without interacting with the vortex ring. Due to buoyancy, the bubbles rise and form a bubble plume. When the bubbly flow is fully developed, a vortex ring is launched into the bubble plume. The vortex ring at the outset is expressed as the Gaussian distribution (Bergdorf et al., 2007)

$$\omega_\theta(\boldsymbol{x}, t = 0) = \frac{\Gamma_0}{\pi\sigma^2} \mathrm{e}^{-(s/\sigma)^2} \tag{3.1}$$

Here, $s^2 = (z - Z_C)^2 + (|(x, y) - (X_C, Y_C)| - R)^2$, (X_C, Y_C, Z_C) is the vortex-ring center, and R, Γ_0, σ are the radius, circulation, and core radius of the vortex ring, respectively. R and σ equal $0.4655D_0$ and $0.111D_0$, respectively. The Reynolds number, $Re_\Gamma = \Gamma_0/\nu_l$, based on the vortex-ring circulation and the liquid-kinematic viscosity, is $8,063$. The initial center location of the vortex ring is $(X_C, Y_C, Z_C) = (0, 0, 1.2D_0)$.

At the cylinder surfaces, the wall of the tank and the top surface of domain (fluid surface), the boundary conditions of the liquid are employed as studied in chapter 2.

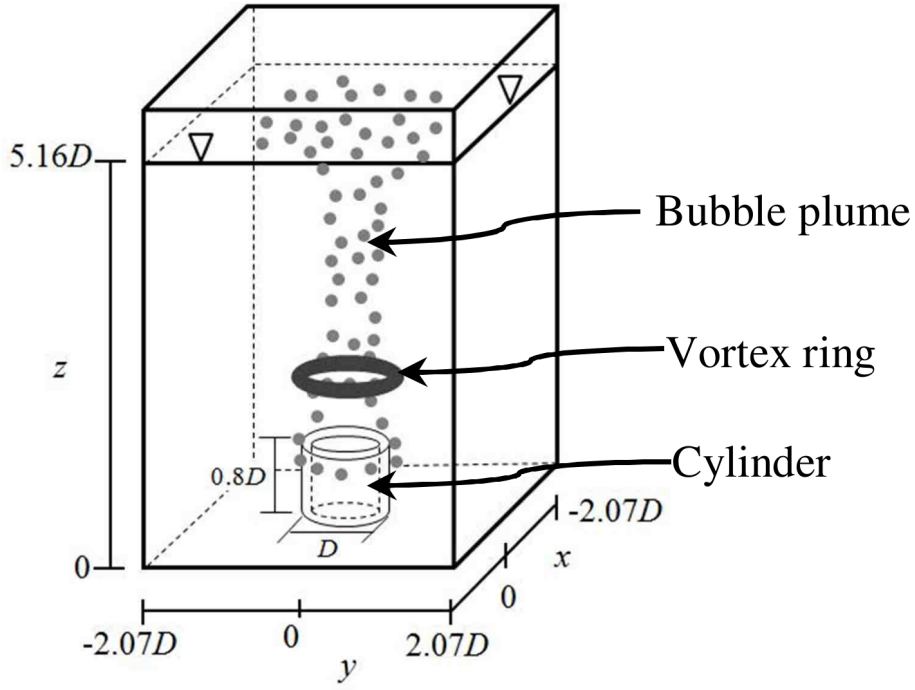

Figure 3.1: Configuration of a vortex ring launched into a bubble plume

3.2.2 Validation

Bubble plume

First, the bubble plume without the vortex ring is simulated. Figure 3.2 shows the liquid velocity and the bubble distribution in the vertical cross section passing through the cylinder's centerline, where t^* is the non-dimensional time defined by $t^* = t\Gamma_0/(D_0/2)^2$. The distributions at four time points are presented. The bubbles, released from the cylinder tip, rise owing to buoyancy and induce a surrounding liquid flow. A meandering motion occurs due to the induced eddies at $t^* \geq 330$. The characteristics of this bubble plume were clarified by the previous numerical investigation of annular bubble plume.

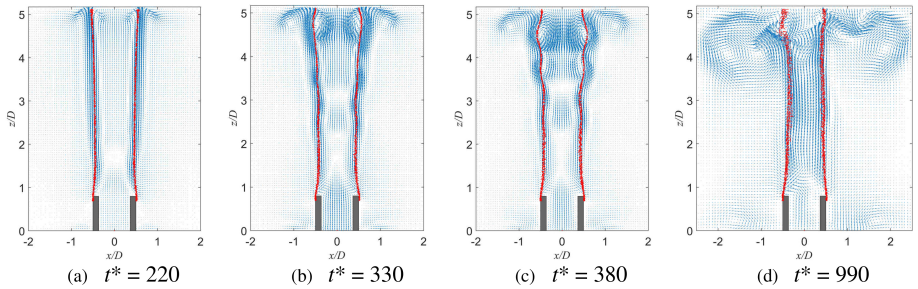

Figure 3.2: Time evolution of the vector liquid-velocity field and bubble distribution on the x-z plane passing through the bubble plume centerline. The liquid velocity field is represented by blue vectors. The bubble distribution is represented by red dots. A cross section of the cylinder is displayed by gray areas

Vortex ring launched into the bubble plume

A vortex ring is launched into the still water. Figure 3.3 shows the time variation of the displacement of the vortex ring, Z_V. The vortex ring convects with a constant velocity. This displacement agrees well with the experiment (Uchiyama and Kusamichi, 2013).

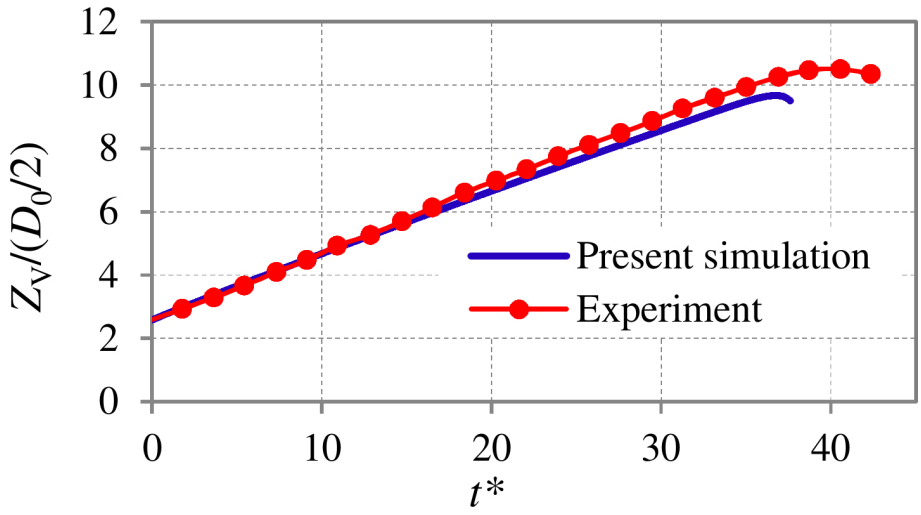

Figure 3.3: Time evolution of displacement of vortex ring

Figure 3.4 shows the velocity profiles along the horizontal lines passing through the center of the vortex ring. The profiles of the velocity component, u_z, at vortex-ring displacements of $Z_V/(D_0/2) = 6.9$ and 9.03 are depicted. The simulated velocity profiles agree nearly with the experimental measurement (Uchiyama and Kusamichi, 2013).

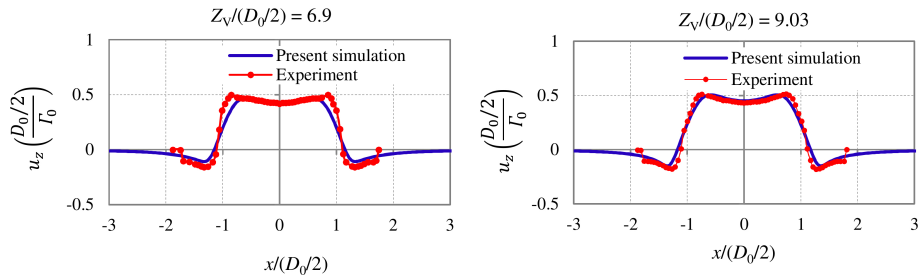

Figure 3.4: Profiles of vertical velocity of liquid on horizontal lines passing through vortex-ring center

When the bubble plume develops until time $t^* = 990$, as can be seen in Fig. 3.2, the bubble distribution at this time is used as the initial condition for the simulation case of the vortex ring launched vertically upward into the bubble plume. Figure 3.5 shows the time evolution of the vorticity distribution in the vertical central cross-section of the vortex ring, where the bubbles are also plotted. At $t^* = 5.5$, the bubbles above the vortex ring tend to move to the rear along the vortex core, where they become spirally entrained. At $t^* = 19.8$ and 24.8, the spiral entrainment proceeds further. The

number of bubbles surrounding the vortex core increases. At $t^* = 29.7$, the number of bubbles around the vortex core is slightly smaller than that at $t^* = 24.8$, and some bubbles are distributed behind the vortex ring. Because the bubbles, moving to the rear of vortex ring, are affected by an inertial force, they are left behind the vortex ring.

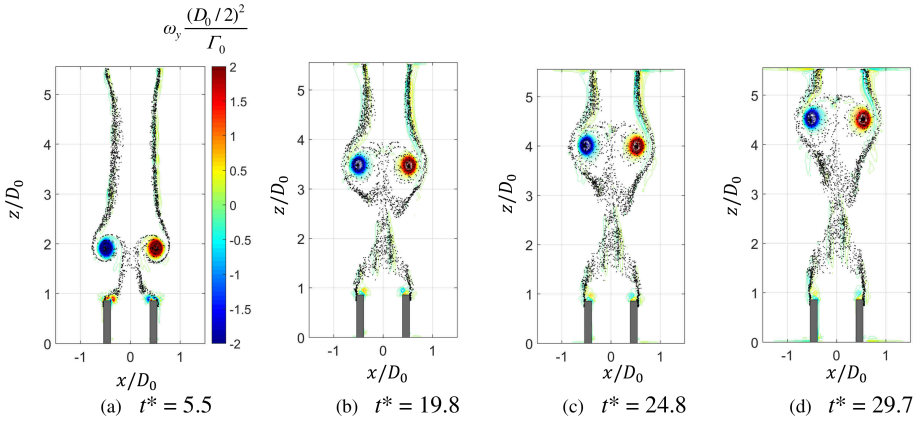

Figure 3.5: Time evolution of vorticity field and bubble distribution on x-z plane passing through vortex-ring center: Bubbles are represented by black dots

Figure 3.6 shows the experimentally visualized bubbles (Uchiyama and Kusamichi, 2013). The bubble entrainment simulated by the present study is almost the same as that visualized by the experiment.

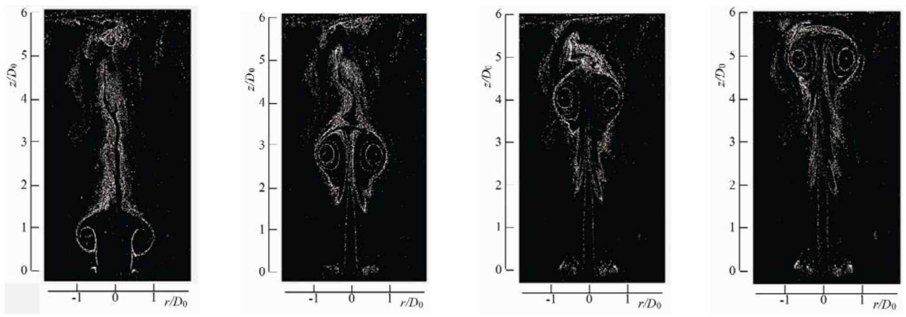

Figure 3.6: Experimentally visualized bubbles around vortex ring on x-z plane passing through vortex-ring center: Bubbles are represented by white dots

Figure 3.7 shows the effects of grid resolution upon the simulation results. The grid-node variation of the vorticity component ω_y at a point $P = (0, 0, Z_V(t^* = 27.5))$, and of the vertical velocity of one bubble, are calculated. The simulation results converge as the grid resolution increases, and the grid resolution used for the present simulation is $240 \times 240 \times 300$ cubic cells.

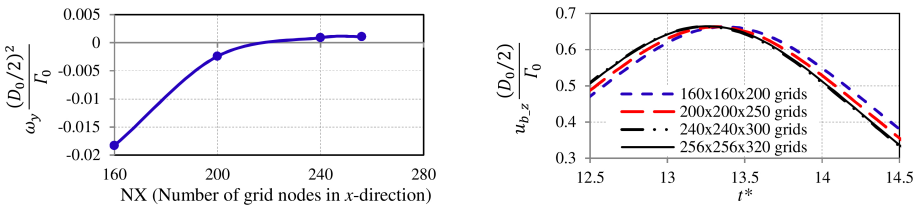

(a) $\boldsymbol{\omega_y}$ at P(0, 0, $Z_V(t^* = 27.5)$) (b) Upward velocity of one bubble

Figure 3.7: Convergence study

3.2.3 Entrainment and transport of bubbles by a vortex ring

The ability of a vortex ring to transport bubbles is investigated through calculation of the total volumes of the bubbles in three control volumes located concentrically with the vortex ring. Control volumes 1, 2, and 3 are three-dimensional cylinders and toruses, respectively, as sketched in Fig. 3.8, and they are expressed by the following equations:

$$\begin{cases} x^2 + y^2 \leq D_0^2 \\ |z - Z_v(t)| \leq D_0 \end{cases} \tag{3.2}$$

$$\begin{cases} x^2 + y^2 \leq D_0^2 \\ |z - Z_v(t)| \leq D_0/2 \end{cases} \tag{3.3}$$

$$\left(R - \sqrt{x^2 + y^2}\right)^2 + \left(z - Z_v(t)\right)^2 \leq \sigma^2 \tag{3.4}$$

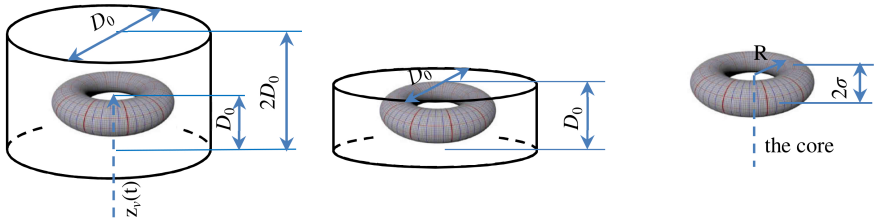

(a) Control volume 1 (b) Control volume 2 (c) Control volume 3

Figure 3.8: Configuration of the control volumes. The vortex-ring core is the three-dimensional gray torus. Control volumes 1 and 2 are the three-dimensional cylinders. Control volume 3 is the vortex-ring core

In figure 3.9, after increasing from the outset to $t^* = 30$, the total volume of bubbles in control volume 1 decreases in the final stage of the flow. Control volume 2 shows a space surrounding the vortex core, while control volume 3 shows a space which is the vortex core. The total volumes of the bubbles in control volumes 2 and 3 increase from the outset to $t^* = 15$ before slightly decreasing in the final stage. The total volume of the bubbles in control volume 2 almost equals that in control volume 3, meaning that most bubbles in control volume 2 accumulate in the core. The vortex ring can transport the bubbles surrounding it over distances.

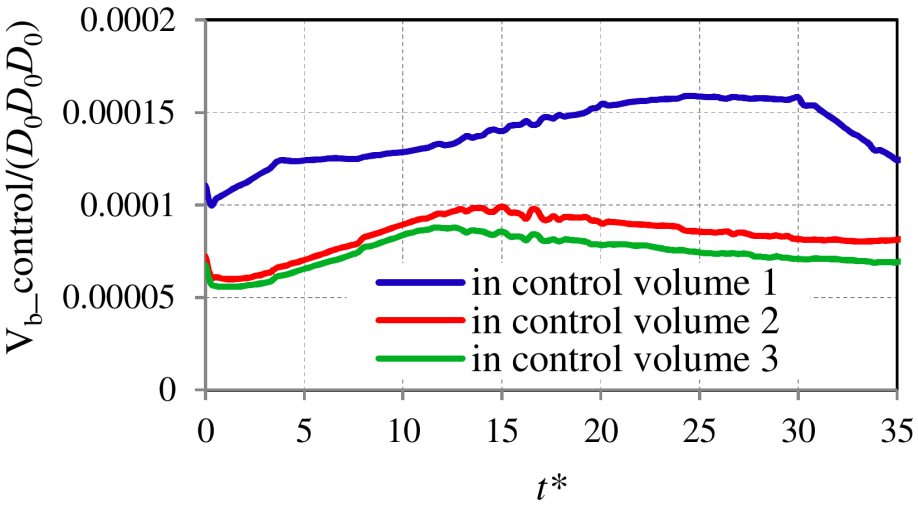

Figure 3.9: Time evolution of total bubble volume in the control volumes

The efficiency of transporting bubbles by vortex ring is clarified by investigating their trajectories and transportation distances. Figure 3.10 shows the vorticity and the bubble distribution on the x-z plane passing through the vortex-ring center at $t^* = 5.5$ and cross sections A_1-A_1, A_2-A_2, A_3-A_3, and A_4-A_4, where bubbles are selected to investigate. Figure 3.11 shows the trajectories of the tracked bubbles over the whole period of the interaction, from $t^* = 0$ to $t^* = 38.5$. At the end of the simulation, the vortex ring reaches a height greater than $z/D_0 = 5.0$. The bubbles, selected from the cross-section A_1-A_1, are affected slightly by the wake of the vortex ring, and their displacement reaches $z/D_0 = 2.0$. They are not transported to a height of $z/D_0 = 5.0$. However, the bubbles, selected from the cross section A_2-A_2, are entrained toward the center of the vortex ring, then accompany it vertically upward. Although they are transported to a height of $z/D_0 = 5.0$, they do not move around the core of the vortex ring. The transportation distance of bubbles located behind the vortex ring depends significantly on the distance, L, between the bubbles and the vortex ring. At $Re_\Gamma = 8,063$, with the distance being $L/D_0 \leq 0.5$, the bubbles behind the vortex ring are completely transported.

After entrainment into the vortex core, some bubbles selected from the cross section A_3-A_3 quickly escape the core. Almost tracked bubbles move together with the vortex ring, and around the core of the vortex many times. The trajectories of these tracked bubbles are similar to two-dimensional-helical curves. In the core's frame of reference, these entrained bubbles are not stationary. The bubbles, selected from the cross section A_4-A_4, are entrained into the rear of the vortex ring and then abandoned behind it. They are not transported to a height of $z/D_0 = 5.0$. The transport of these bubbles by the vortex ring is not efficient.

The mechanism of the bubble motion is clarified by calculating the time evolution of their upward velocity, u_{gz}, as shown in Fig. 3.12. Bubbles 1, 2, and 3, selected from the cross section A_1-A_1, move at an almost constant velocity. They do not move along with

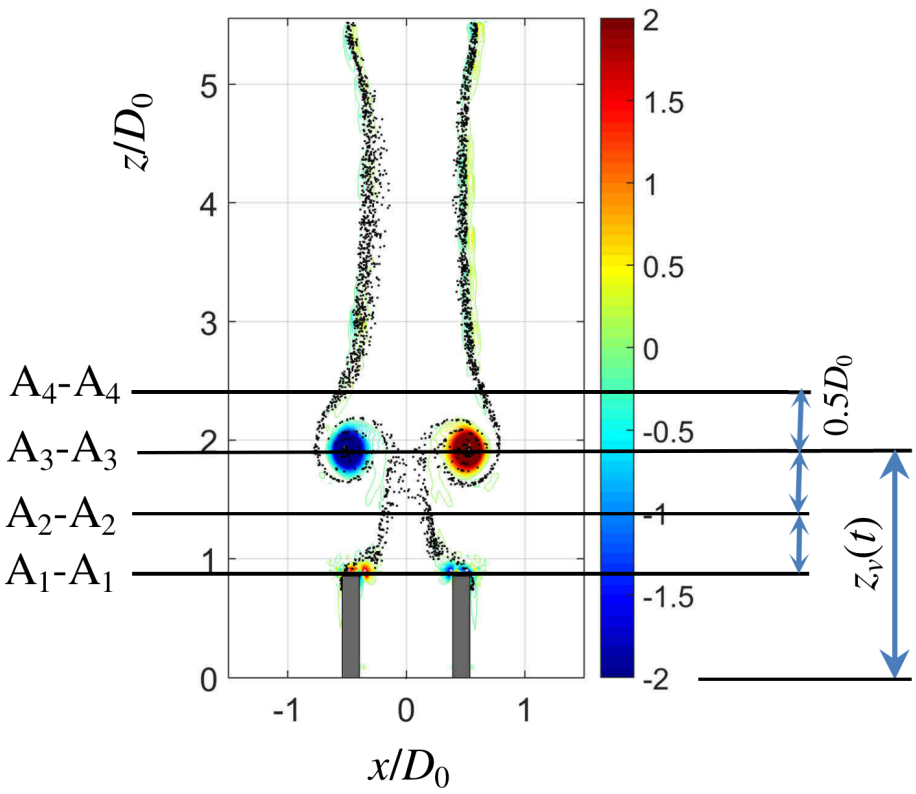

Figure 3.10: Vorticity and bubble distributions at $t^* = 5.5$ on the x-z plane passing through the vortex-ring center, and cross sections A_1-A_1, A_2-A_2, A_3-A_3, and A_4-A_4

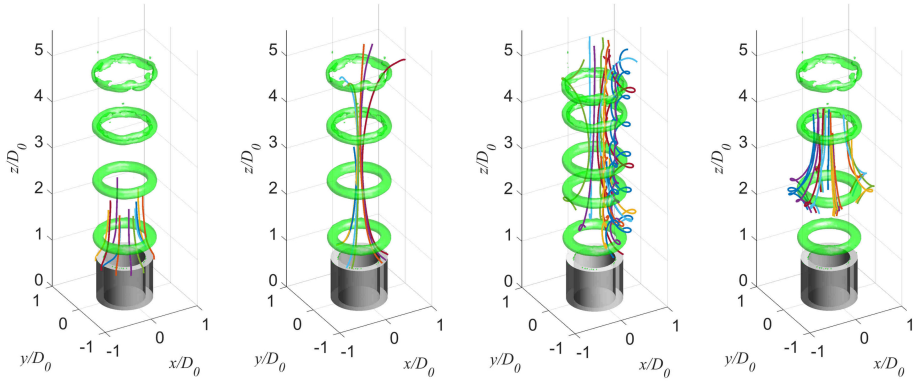

(a) From A_1-A_1 (b) From A_2-A_2 (c) From A_3-A_3 (d) From A_4-A_4

Figure 3.11: Trajectories of the bubbles over the whole period of the interaction between the vortex ring and bubble plume. These bubbles are selected from cross sections A_1-A_1, A_2-A_2, A_3-A_3, and A_4-A_4 at time $t^* = 5.5$

the vortex ring, their motions are dominated by buoyancy, and their velocities are similar to the terminal velocity of a single bubble rising in quiescent water. Bubbles 4, 5, and 6, selected from the cross section A_2-A_2, are entrained towards the vortex-ring center, their velocities increase significantly. Subsequently, they move together with the vortex ring, and their velocities decline strongly. Bubbles 7, 8, and 9, selected from the cross section A_3-A_3, accelerate when they move from the rear to the central side of the vortex ring. In the vortex core, they decelerate and move around the core. When located below the

core fringe, they accelerate again. Their upward velocity is nearly periodic and gradually extinguished by the vortex-ring convection. Bubbles 10, 11, and 12, selected from the cross section A_4-A_4, move with negative velocity when they are attracted to the rear of the vortex ring. Subsequently, abandoned behind, they move at a speed slightly higher than terminal velocity.

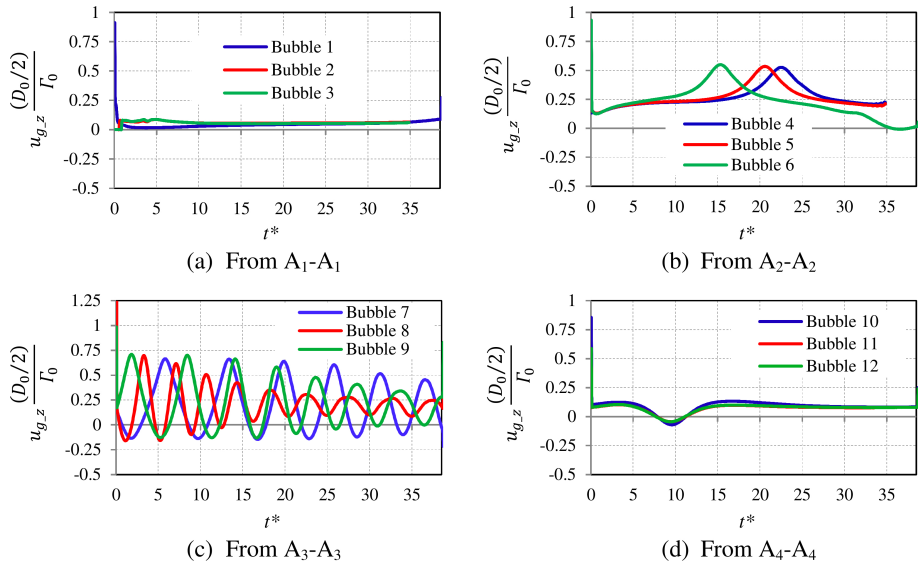

(a) From A_1-A_1 (b) From A_2-A_2

(c) From A_3-A_3 (d) From A_4-A_4

Figure 3.12: Time evolution of vertical velocity of bubbles

Figure 3.13 shows the vorticity magnitudes at the trajectories of the tracked bubbles and at the core center. The core center is the position of the maximum of the vorticity magnitude, while at the vortex-ring center the vorticity magnitude is negligible. The bubbles, selected from the cross sections A_1-A_1, A_2-A_2, and A_4-A_4, settle far from the core center. Therefore, the vorticity-magnitude values at these bubbles are much smaller than those at the core center. However, the vorticity magnitude at the trajectories of three bubbles, selected from the cross section A_3-A_3, gradually approaches to those at core center. In other words, these bubbles are entrained into the core center. From the figure, the fastest process of bubble entrainment into the core center is observed on bubble 8, following bubbles 9 and 7, respectively. Bubble 8 is entrained near the core from $t^* = 12.5$, and then moves around the core center. At the end of the simulation, the vorticity-magnitude values at the trajectories of these bubbles and at the core center almost converge. The speed of the bubble entrainment into the core depends significantly on the correlative initial position between the bubble and the core center.

The dependence of the bubble motion upon the correlative initial position between the bubble and the core center is further investigated. Figure 3.14 shows the time evolution of the vertical velocity of bubbles 13, 14, and 15 initialized at the core center and the vorticity-magnitude value at the positions of these bubbles. Their upward velocity and the vorticity-magnitude values at these bubbles fluctuate slightly, as compared to bubbles

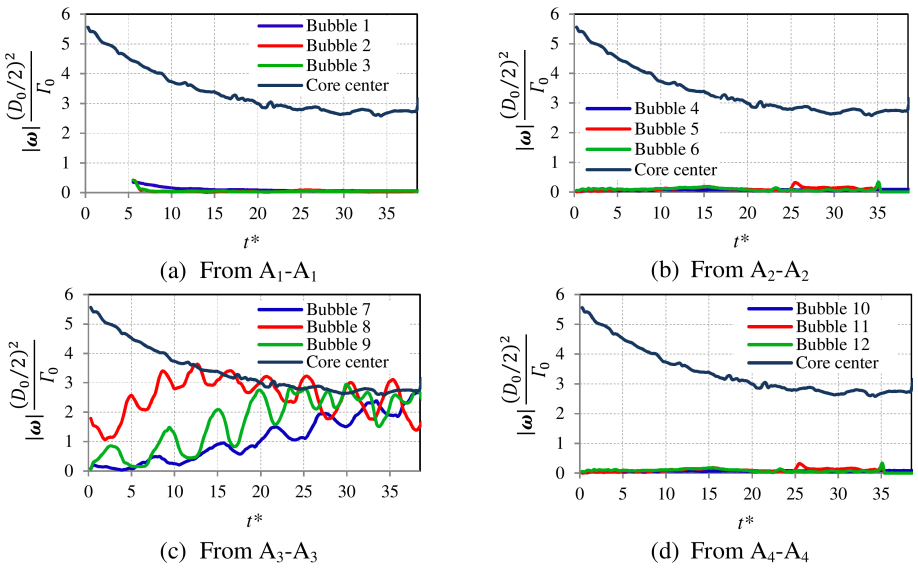

(a) From A_1-A_1 (b) From A_2-A_2

(c) From A_3-A_3 (d) From A_4-A_4

Figure 3.13: Time variation of liquid-vorticity magnitude calculated at the position of tracked bubbles and at core center

7, 8, and 9. The motion of these bubbles is more stable than those selected from the cross section A_3-A_3. In the core's frame of reference, they are almost stationary.

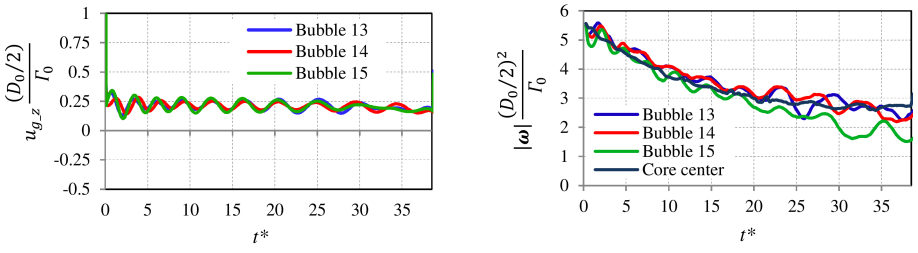

(a) (b)

Figure 3.14: a) Time evolution of the upward velocity of bubbles initialized at core center; b) time evolution of the vorticity magnitude calculated at the positions of the bubbles initialized at core center

The azimuthal motion of the bubbles, selected from the cross sections A_2-A_2 and A_3-A_3, is investigated. Figure 3.15 shows a projection of the trajectories of the tracked bubbles onto the bottom of the domain. In general, the azimuthal displacement of the bubbles is small. The motion of the bubbles is almost in two dimensions. This is ascribed to the fact of that the vorticity component, ω_z, is small compared to the ω_x and ω_y components. The motion of these bubbles is dominated by the two-dimensional vortex structure . After being entrained toward the center of the vortex ring, the azimuthal displacement of the bubbles selected from the cross section A_2-A_2 is observed. Some bubbles, selected from the cross section A_3-A_3, do not move around the core, and their azimuthal displacement is not observed, while the bubbles with trajectories similar to helical shapes, their azimuthal displacement is observed. This is explained as a fact

that these bubbles locate in the core longer than other bubbles. The core in which has the most significant impact on the azimuthal motion of the bubbles. The azimuthal displacement of these bubbles fluctuates and increases with the time evolution.

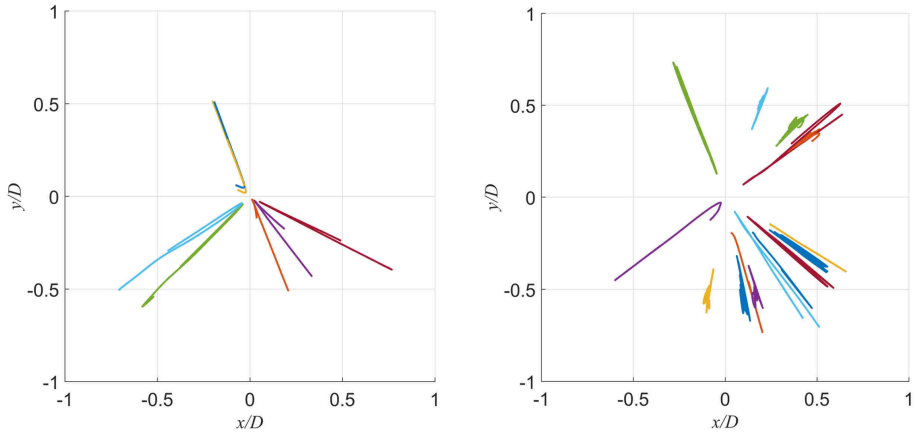

(a) From A_2-A_2 (b) From A_3-A_3

Figure 3.15: A top-bottom view of bubble trajectories over whole period of interaction

Figure 3.16 shows the azimuthal velocity, $u_{g-\theta}$, of the bubbles selected from the cross sections A_2-A_2 and A_3-A_3. This velocity is obtained by transforming u_g from the Cartesian coordinate system to the cylindrical coordinate system. The azimuthal velocities of bubbles 4, 5, and 6 selected from the cross section A_2-A_2 are almost zero in the range from the outset to $t^* = 20$. These velocities change significantly when these bubbles are entrained into the central side of the vortex ring. The fluctuation of these bubble velocities is not observed, because they do not move around the core. By contrast, the azimuthal velocities of bubbles 7, 8, and 9 selected from the cross section A_3-A_3 fluctuate slightly in the early stage and strongly from $t^* = 15$, owing to the growth of vorticity component ω_z, as explained later.

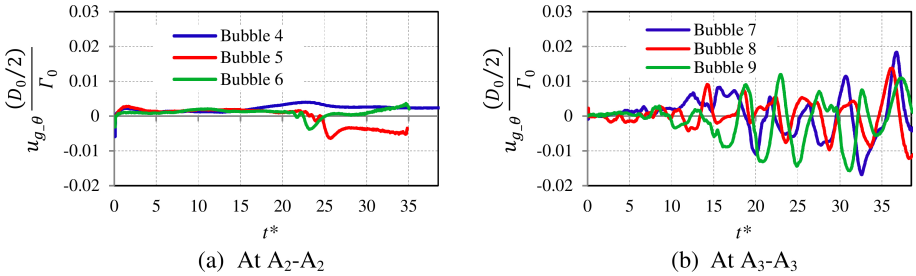

(a) At A_2-A_2 (b) At A_3-A_3

Figure 3.16: Time evolution of azimuthal velocity of bubbles

The azimuthal bubble motion is further clarified by comparing the azimuthal velocity of the bubble to the azimuthal velocity of the liquid calculated at these bubble location. In Fig. 3.17, when bubbles 7 and 8, selected from the cross section A_3-A_3, are located far from the core center, their azimuthal motion is less controlled by the liquid. The

azimuthal velocity of the bubbles is much smaller than that of the liquid during this period. When these bubbles approach the core center, their azimuthal motion is more controlled by the liquid. The azimuthal velocity of the bubbles almost equals the liquid velocity. This is caused by the bubbles being closer to the core center, making their motion more stable.

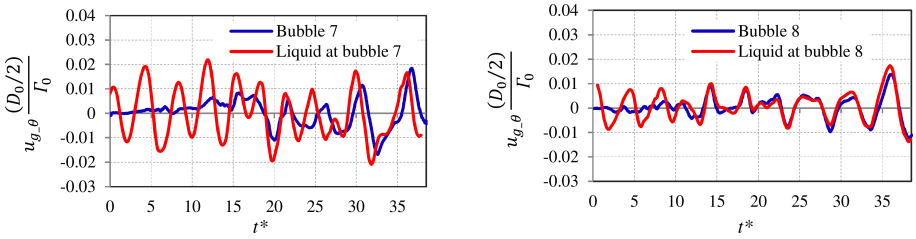

Figure 3.17: Azimuthal velocity of two bubbles and of liquid calculated at these bubble locations

3.2.4 Effects of entrained bubbles upon vortex structure

The effects of the entrained bubbles upon the vortex structure are investigated. Figure 3.18 shows a comparison of the vorticity profiles along the horizontal lines passing through the vortex-ring center between two simulation cases. In the early stage of flow, as can be seen at $t^* = 5.5$, the effects of the entrained bubbles on the vorticity distribution are low. This is explained as the fact that the total volume of the entrained bubbles in the vortex core is small and the accumulation of vortex-stretching effects is inadequate. These effects increase with time, as can be seen at $t^* = 16.5, 27.5$, and 33. The vorticity values at the core center reduce significantly, owing to the bubble entrainment. The vorticity-distribution peaks reduce gradually with the flow evolution. Uchiyama and Kusamichi (2013) showed that the entrained bubbles cause the decrement of the absolute value of the vorticity around the vortex core, reducing the vortex-ring strength. The present simulation results are favorably parallel with the experimental measurements.

To clarify the relationship between the entrained bubbles and the vortex deformation, the gas volume fraction and vortex-deformation intensity are calculated. As shown in Fig. 3.19, the vortex structure is deformed at the entrained-bubble locations, and the deformation peak is at the core center. Moreover, the deformation intensity is nearly directly proportional to the total volume of the entrained bubbles.

Figure 3.20 shows the effects of the entrained bubbles upon the vertical liquid-velocity distribution. In general, at three distinct time points, the entrained bubbles increase the liquid velocity. At $t^* = 5.5$, the effects of the entrained bubbles upon the liquid velocity are small, owing to the small amount volume of entrained bubbles in the vortex core. These effects increase with the time evolution. The maximum effects are at the core

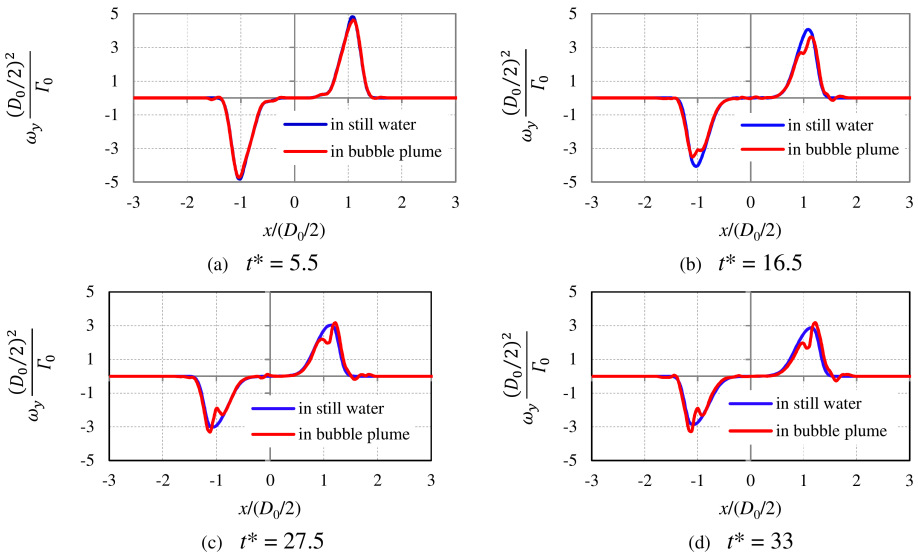

Figure 3.18: Profiles of liquid vorticity ω_y along horizontal lines passing through vortex-ring center at four time points

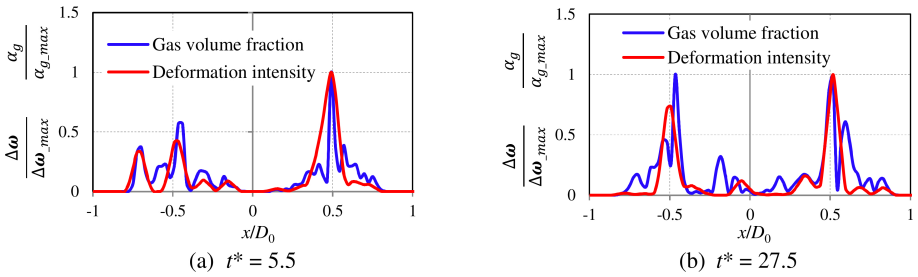

Figure 3.19: Profiles of the gas-volume fraction and vortex-deformation intensity along the horizontal lines passing through the vortex-ring center at two times in two simulation cases. The vortex-deformation intensity is $\Delta\boldsymbol{\omega}/\Delta\boldsymbol{\omega}_{max}$, where $\Delta\boldsymbol{\omega} = ||\boldsymbol{\omega}_{case1}| - |\boldsymbol{\omega}_{case2}||$

center, and the liquid velocity is increased by 33.33%, as can be seen at $t^* = 27.5$.

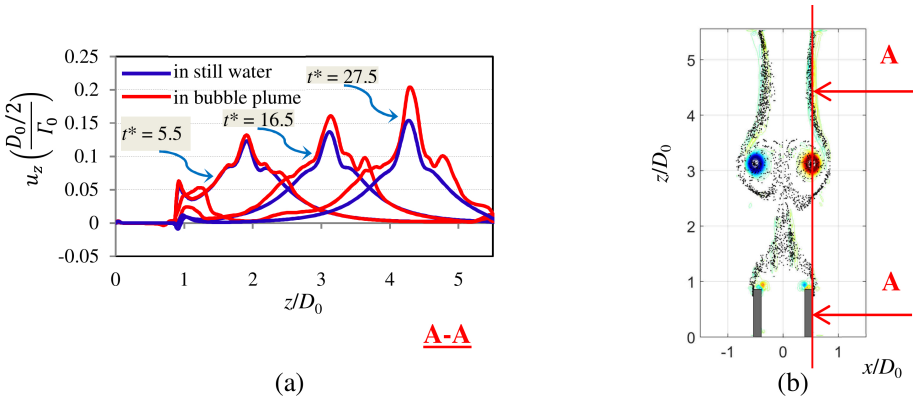

Figure 3.20: (a) Profiles of upward liquid velocity on a vertical line passing through the core center in two simulation cases at three point time points. (b) Configuration on the vertical line, where liquid velocity is investigated

The effects of the entrained bubbles upon the vortex structure are further clarified by investigating the time evolution of Q-contour lines. The Q-criteria, a type of vortex identification method, represented as the balance between the local shear-strain rate and vorticity magnitude, is used to determine a three-dimensional vortex core (Jeong and Hussanin, 1995). Q is calculated as $Q \equiv 0.5(u_{i,i}^2 - u_{i,j}u_{i,j}) = -0.5u_{i,j}u_{j,i} = 0.5(||\Omega||^2 - ||S||^2)$, where $S_{ij} = 0.5(u_{i,j} + u_{j,i})$ and $\Omega_{ij} = 0.5(u_{i,j} - u_{j,i})$. Figure 3.21 shows the time evolution of the Q-contour lines. In the plots along the top row of Fig. 3.21, when a vortex ring is launched into still water, the shape of the Q-contour lines is conserved over the whole time evolution. By contrast, in the plots on the bottom row of Fig. 3.21, when the vortex ring is launched into the bubble plume, the shapes of Q-contour lines are not conserved over the whole period. In the early stage of flow, as shown at $t^* = 5.5$, the Q-contour lines almost remain unchanged. They are then deformed, as shown at $t^* = 16.5$ and 27.5. The vortex structure is fragmented into multiple regions with the highest values of Q settled at their centers. The Q-contour lines with maximum values are first deformed, followed by those with lower values. This deformation starts at the position of high entrained-bubble concentration or at the core center, and spreads gradually to the core fringe, as shown at contours $Q = 0.5$ and 1 at times $t^* = 16.5$ and 27.5.

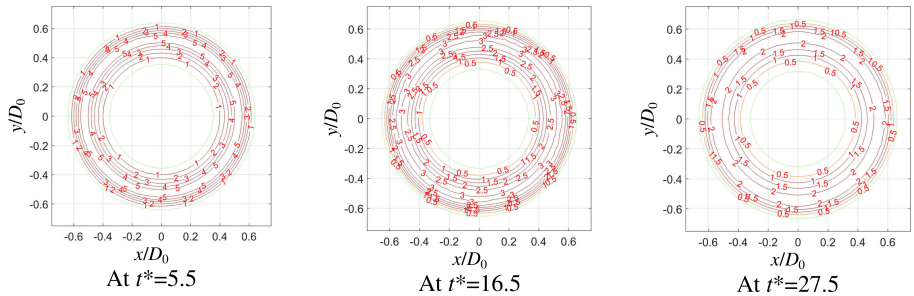

(a) A vortex ring is launched into still water

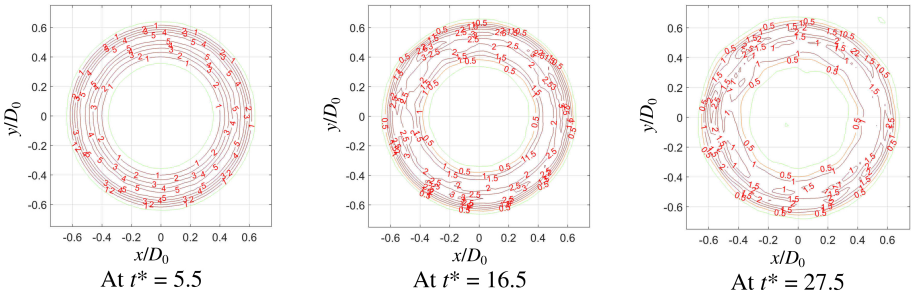

(b) A vortex ring is launched into bubble plume

Figure 3.21: Time evolution of Q-contour lines on the transverse planes passing through the vortex-ring center

The time evolution of the vortex-ring circulation is investigated,as shown in Fig. 3.22. The circulation is calculated on the x-z plane passing through the vortex-ring center as follows (Bergdorf et al., 2007):

$$\Gamma = \frac{1}{2}\iint_{A^+} \omega_y dxdz - \frac{1}{2}\iint_{A^-} \omega_y dxdz \tag{3.5}$$

where $A^+ = [0, D_0] \times [-0.5D_0 + z_v(t), 0.5D_0 + z_v(t)]$ and $A^- = [-D_0, 0] \times [-0.5D_0 + z_v(t), 0.5D_0 + z_v(t)]$. The circulation is calculated using this control area to avoid the effects of a vortex at the cylinder tip. The circulation of the vortex ring launched into the bubble plume is slightly smaller than that launched into the still water. This agrees with the experimental measurements by Sridhar and Katz (1999), Wang et al. (2013), and Uchiyama and Yoshii (2015a).

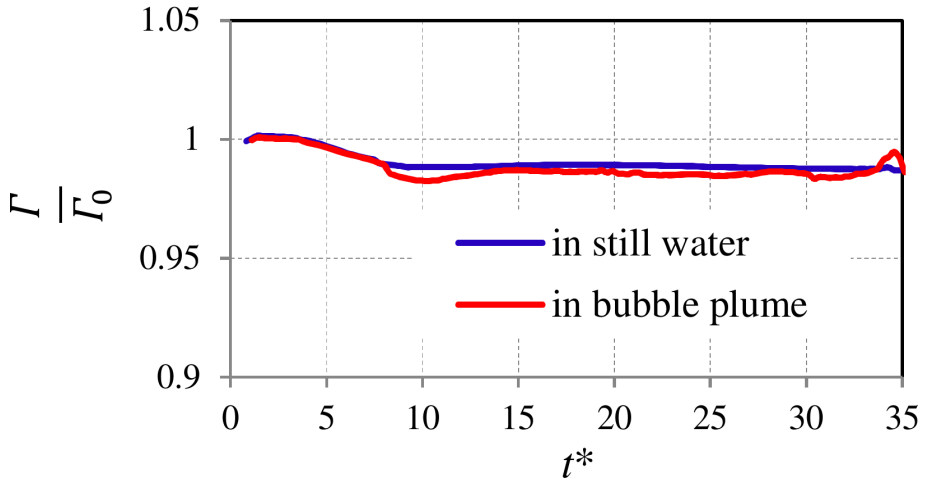

Figure 3.22: Time evolution of the vortex-ring circulation

Finally, the effects of the entrained bubbles upon the vortex-ring instability are investigated. This instability is expressed through visualization of the structure of ω_z and the energy spectrum of ω_z. Figure 3.23 shows the time evolution of the vorticity component ω_z in two simulation cases. In the plots on the top row of Fig. 3.23, the case of the vortex ring launched into still water, ω_z is constructed by arranging eight smaller clockwise and counterclockwise cores. These cores, visualized by red and green surfaces, interleave evenly. The strength of these cores increases with time. In the plots on the bottom row of Fig. 3.23, the case of the vortex ring launched into the bubble plume, ω_z is deformed in the early stage of the flow and then disturbed with time due to the entrained-bubble effects. The vorticity-component structure is broken up into multiple smaller scales.

The effects of the entrained bubbles on the vortex-ring instability are clarified by calculating the energy spectrum of ω_z. In case of the vortex ring launched into still water, the values of ω_z along a circle of radius R, are calculated. In case of the vortex ring launched into the bubble plume, the values of ω_z along three circles of radius R-σ, R, and R+σ are computed. These circles are concentric with the vortex ring. The values of ω_z along these circles are measured at three time-points, $t^* = 5.5, 16.5$, and 27.5, and then calculated by the Fourier transform. Figure 3.24 shows the energy spectrum of ω_z along these circles. In column (a), when vortex ring is launched into still water, one significant harmonic oscillation with mode (referred to m) $= 8$ is observed over the whole time evolution. The energy of this harmonic oscillation increases with time. In column (b),

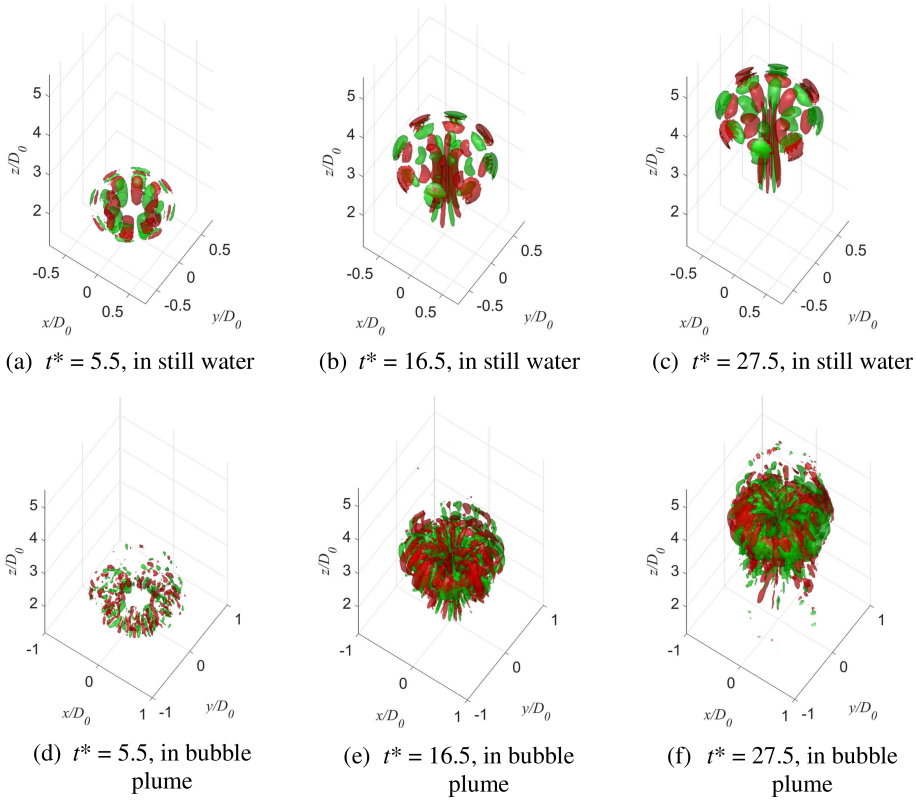

(a) t^* = 5.5, in still water (b) t^* = 16.5, in still water (c) t^* = 27.5, in still water

(d) t^* = 5.5, in bubble plume (e) t^* = 16.5, in bubble plume (f) t^* = 27.5, in bubble plume

Figure 3.23: Time evolution of the vorticity component ω_z in two simulation cases: Isosurfaces of $\omega_z(D_0/2)^2/\Gamma_0$ at values ± 0.025 and ± 0.05 are represented in the top and bottom rows, respectively. The positive and negative values of ω_z are represented by the red and green surfaces, respectively

the case of the vortex ring launched into the bubble plume, the energy is transferred to the second harmonic oscillation with $m = 16$ at $t^* = 16.5$ and then to the third harmonic oscillation with $m = 24$ at $t^* = 27.5$. Bergdorf et al. (2007) pointed out that, in the case of the vortex ring launched into the still water, after a long evolution of the vortex structure, the second and third harmonics appear sequentially. Therefore, it is clear that the entrained bubbles excite growth rate of the azimuthal instability of the vortex ring.

3.3 Conclusions

The interaction between the vortex ring and the bubble plume was simulated using a semi-Lagrangian–Lagrangian approach. This approach is composed of the vortex-in-cell method for the liquid phase and a Lagrangian description for the gas phase. The characteristics of the bubble plume, liquid-velocity distribution, vortex-ring displacement, and bubble entrainment into the vortex ring were compared favorably with the corresponding experimental measurements. Our conclusions are given as follows:

(1) The vortex ring can transport the surrounding bubbles. The transportation

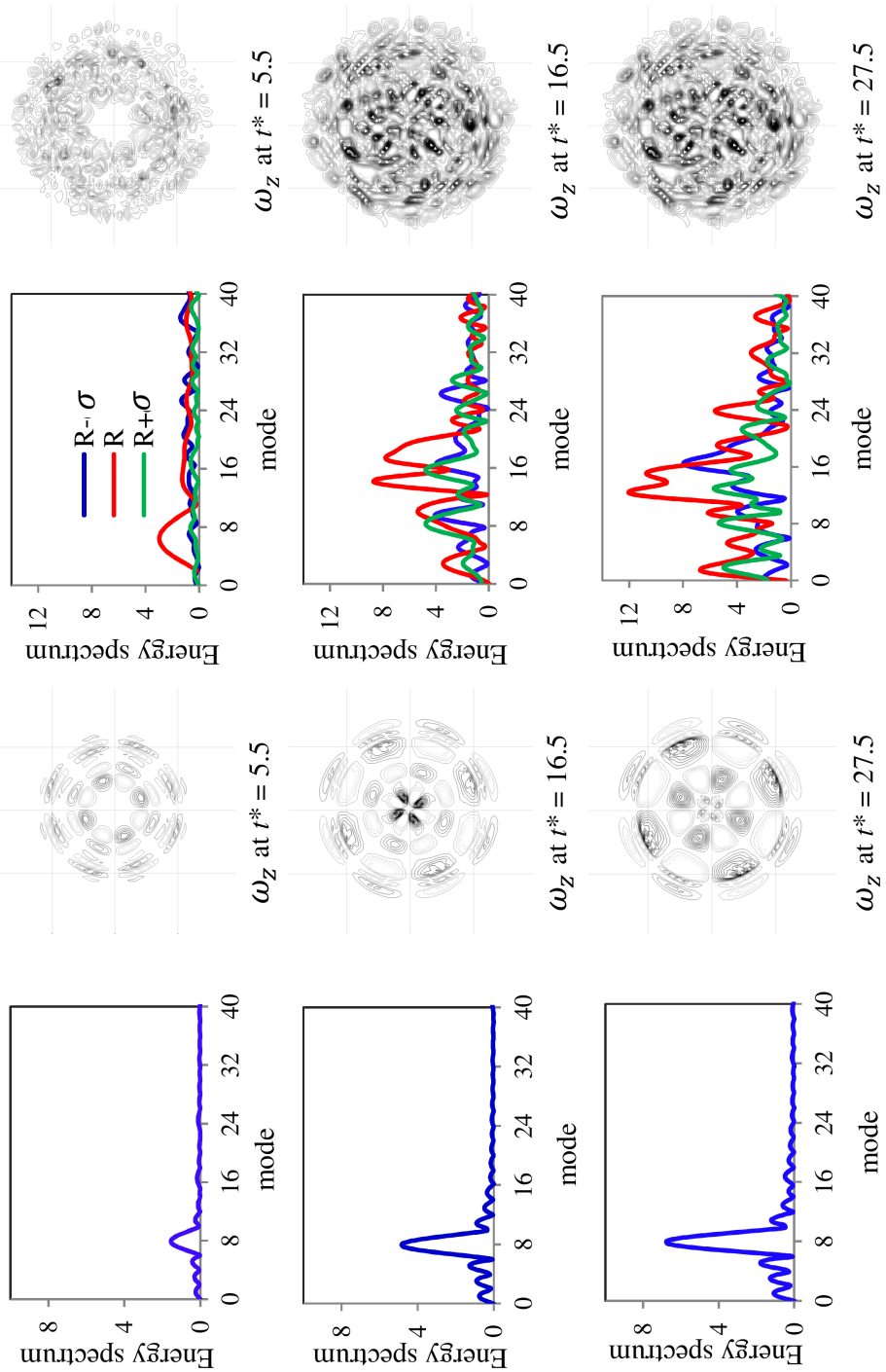

(a) Vortex ring launched into still water

(b) Vortex ring launched into bubble plume

Figure 3.24: Energy spectrum of ω_z

distance of bubbles significantly depends upon the correlative initial position between the bubbles and the core center. The bubbles initialized behind the vortex ring at a distance of less than a half of vortex ring's diameter are completely transported by the vortex ring. For greater initial distances, the bubbles are left behind the vortex ring. The bubbles initialized above the vortex ring are transported less efficiently. They are left behind when they move to the rear of the vortex ring.

(2) The bubble dynamics have the following characteristics. The entrained bubbles prefer to distribute near the core center of the vortex ring. The bubbles initialized near the core center are rapidly entrained, while the bubbles initialized far away take more time to distribute near the core center. The motion of these bubbles is nearly periodic and gradually extinguished with the time evolution. The bubble trajectories are similar to two-dimensional helical shapes. The bubbles initialized at the core center just move along with the vortex ring, and their motion is more stable than that of bubbles initialized farther from the core center. The azimuthal motion of the entrained bubbles increases when they are close to the core center. With time evolution, the azimuthal motion of these bubbles is gradually controlled by the azimuthal motion of the liquid phase. The bubble velocity equals the liquid at the bubble location.

(3) The effects of the entrained bubbles upon the vortex structure were clarified. The entrained bubbles deform the vortex structure, and this deformation increases with the vortex-ring convection. The deformation intensity is nearly directly proportional to the total volume of the entrained bubbles, and the deformation peak is observed at the core center. This deformation starts at the position of high entrained-bubble concentration, gradually spreading from the core center to the core fringe. The vortex core is fragmented into multiple regions with high values of Q settling at the centers of these regions. Although the entrained bubbles enhance the upward liquid velocity of the core center, the vortex-ring circulation remains almost unchanged.

(4) The entrained-bubbles excite the growth rate of the azimuthal instability of the vortex ring. In the case of a vortex ring launched into still water, one harmonic oscillation with mode = 8 is observed during its evolution. In the case of a vortex ring launched into the bubble plume, a second harmonic oscillation with mode = 16 and a third harmonic oscillation with mode = 24 appear sequentially during its evolution.

Nomenclatures

C_D, C_L, C_V	Drag, lift, and virtual mass coefficients of the bubble, respectively
d	Signed distance from fluid–solid interface to grid node
d_b	Bubble diameter
D_0	Outer diameter of the cylinder
$\boldsymbol{F}_B, \boldsymbol{F}_D, \boldsymbol{F}_L, \boldsymbol{F}_{VM}, \boldsymbol{F}_P$	Buoyancy, drag, lift, virtual mass, and pressure gradient forces, respectively
$\boldsymbol{g}$	Gravitational acceleration
Nt	Number of simulation time steps
p	Pressure
Q	Bubble flow rate
Q	Second invariant of velocity gradient tensor
R	Vortex-ring radius
RMS	Root mean square
Re_b	Bubble Reynolds number
$Re_\Gamma = \Gamma_0/\nu_l$	Vortex-ring Reynolds number
S, F	Solid and fluid regions, respectively
t	time
t^*	Non-dimensional time
$\boldsymbol{u}_l, \boldsymbol{u}_g$	Liquid and gas velocity, respectively
$u_{b-\theta}$	Bubble azimuthal velocity
$\boldsymbol{u}_\lambda$	Penalization velocity
V_b	Bubble volume
W	Redistribution function of vorticity
$\boldsymbol{x}, \boldsymbol{x}_p, \boldsymbol{x}_q$	Coordinate, vortex-particle location, and grid node location, respectively
Z_V	Vortex-ring displacement
X_C, Y_C, Z_C	Initial location of vortex-ring center
α_l, α_g	Volume fraction of liquid and gas phases, respectively
ρ_L, ρ_g	Density of liquid and gas phases, respectively
β	Density ratio between gas and liquid phases
$\boldsymbol{\omega}$	Vector liquid vorticity
$\omega_x, \omega_y, \omega_z$	Components of $\boldsymbol{\omega}$

$\boldsymbol{\omega}_\lambda$	Penalization vorticity
ϕ	Scalar potential
$\boldsymbol{\psi}$	Vector potential
ψ_x, ψ_y, ψ_z	Components of $\boldsymbol{\psi}$
ν_l	Liquid kinematic viscosity
λ	Penalization parameter
χ_S	Solid-mask function
$\Delta x, \Delta y, \Delta z$	Grid widths
Δt	Time-increment
S, Ω	Strain and rotation rate tensors, respectively
τ_b	Bubble time-scale
Γ_0	Vortex-ring circulation
σ	Core radius of the vortex ring
u_x, u_y, u_z	Liquid velocity components
u_θ	Liquid azimuthal velocity
$\boldsymbol{u}_S$	Solid velocity
u_t	Bubble terminal velocity
$V_{b-control}$	Total volume of bubbles in the control volume
W_α	Redistribution function of gas-volume fraction

Table 3.1: Nomenclature

Chapter 4

Numerical simulation of bubbly flow around a cylinder

4.1 Introduction

Gas–liquid two-phase flows around rigid obstacles are observed widely in engineering applications, such as shell and tube heat exchangers, steam generators, and condensers. A comprehensive understanding of the phenomena of gas–liquid two-phase flows around obstacles would allow for improved design and control of related engineering devices. Therefore, several researchers investigated their characteristics by generating a liquid flow around obstacles at a Reynolds number with a mixture of entrained bubbles in the upstream region, such as Inoue et al. (1986), Yokosawa et al. (1986), Lian et al. (1999), Uchiyama (2003a,b), Sugiyama et al. (2001), Bamardouf and McNeil (2009), Huang et al. (2006), and Degawa and Uchiyama (2008).

Free bubbly flow around obstacles was described by Murai et al. (2005) as first a free rise of bubbles inducing liquid flow and then the movement of both phases around the obstacles. Furthermore, the spatial scale of the two-phase convection was shown to depend sensitively upon the cylinder shape. All cylinder types studied, including a circular, square, triangular, ellipsoidal, and star cylinder, induced a wide single-phase wake region behind them that was much larger than the cross-section of the corresponding cylinder. A free bubbly flow of a bubble plume composed of five plane bubble plumes around a circular cylinder was investigated by Uchiyama and Ishiguro (2016). They showed that bubbles distributed along the lower half of the surface of the cylinder before separating from both sides of the cylinder to form bubble layers that convected almost vertically. Although the bubbles were entrained into the plume centerline downstream, they hardly distributed just behind the cylinder. The water shear layers also were shown to separate at both sides of the cylinder and roll up to form large-scale eddies that entrained the surrounding bubbles. However, many characteristics of the free bubbly flow around an obstacle have not yet been clarified, such as a vortex structure induced by the bubble plume, the slip velocity of the bubbles, or the relation between the patterns of the liquid and gas phases. Therefore, this work aims to clarify the characteristics of a free bubbly flow around an obstacle using numerical simulations using a circular cylinder to

represent the obstacle.

Thus far, three approaches have been used in computational fluid dynamics to simulate bubbly flows around an obstacle: Eulerian–Eulerian (E–E) (Uchiyama, 2003a,b; Bamardouf and McNeil, 2009), Eulerian–Lagrangian (E–L) (Sugiyama et al., 2001), and Lagrangian–Lagrangian (L–L) (Huang et al., 2006; Degawa and Uchiyama, 2008). This classification is based on a mathematical description of each phase, with which its governing equations are solved using either a mesh-free method or mesh-based method. Here, a semi-Lagrangian–Lagrangian (semi-L–L) method composed of a vortex-in-cell (VIC) method for the liquid phase and a Lagrangian description of the gas phase is developed, based on previous investigations, for the simulation of a bubbly flow around an obstacle.

The VIC method is a semi-Lagrangian (semi-L) method known as a remeshed vortex particle, hybrid E–L vortex method that has been extensively used for the simulation of incompressible flows. This method generally uses the vortex particles's transport conservative quantities and a grid-based formula to calculate the flow fields (Cottet and Poncet, 2003). The liquid flow is discretized into vortex particles that carry the liquid momentum in term of vorticity and move at the local liquid velocity field at the particle locations. Subsequently, the vortex particles are redistributed on the regular grid using interpolation schemes that ensure momentum conservation. The velocity and vorticity fields are then calculated on the grid nodes by solving the Poisson and momentum equations, respectively. The hybrid vortex method takes advantage of the mesh-based Eulerian method to remedy disadvantages of the mesh-free Lagrangian vortex method, while still benefiting from its advantages. First, the velocity is obtained in the Lagrangian vortex method using the Biot–Savart integral formula, in which the calculation of the velocity of each vortex element needs at least $(N-1)$ multiplications from the rest of vortex elements, leading to a total computational cost of $\mathcal{O}(N^2)$ operations for N vortex elements, also known as N-body problem in celestial mechanics. However, the computational cost decreases significantly if the velocity field is obtained by solving the Poisson equation using a mesh-based method such as the successive-over-relaxation method with $\mathcal{O}(N^{3/2})$ operations and the fast-Fourier-transform method with $\mathcal{O}(Nlog_2N)$ operations. Second, the calculation of the momentum equation using the mesh-based method uses a smart grid system, in which the flow quantities are discretized in a consistent manner to improve the method's accuracy and efficiency (Uchiyama et al., 2014b). Third, using redistribution schemes overcomes a persistent problem of the Lagrangian vortex method in which the vortex distribution is distorted with time, leading to a loss of accuracy, also known as vortex overlap issues. Due to the Lagrangian nature and fluid strain, the vortex elements cluster, leading to a lack of vortex elements in some regions in which a number of the vortex particles required to be adequate to satisfy a continuousness of the vorticity field (Barba et al., 2003). Fourth, the use of the Eulerian grid formula allows combining

the method with an immersed boundary (IB) method to implement the no-slip condition of the liquid flow on the surface of the solid obstacles of arbitrary shapes. The current method also takes advantage of the Lagrangian vortex method, which supplies a natural description of fluid dynamics and has a superior capability to analyze the evolution of a vortex structure, such as the formation, deformation, and decay of eddies of various scales. In the VIC method, the liquid flow is described in the Lagrangian frame, the convection term is solved using a linear equation, this offering a lower numerical dissipation than when using the nonlinear convection equation in the Eulerian frame.

The VIC method was proposed by Christiansen (1973) to simulate two-dimensional incompressible inviscid and homogeneous fluid flows and then adapted for two- and three-dimensional incompressible viscous fluid flows by Cottet and Koumoutsakos (2000). Cottet and Poncet (2002) then proposed a VIC method combined with a penalization method to simulate flow around a body. Uchiyama et al. (2014b) further improved the VIC method to heighten its numerical accuracy and efficiency. The VIC method was proved to be robust and efficient to simulate flow around two tandem cylinders, as studied in Appendix A. The VIC method has also been used to simulate a variety of two-phase flows such as bubbly flows by Uchiyama and Yoshii (2015b) and solid particle-gas flows by Uchiyama and Shimada (2014). In this study, the VIC method to simulate bubbly flow is combined with an IB method to investigate the characteristics of a bubbly flow around a circular cylinder. The remainder of this chapter is organized as follows: the numerical method is explained in section 4.2, the results are discussed in section 4.3, and conclusions are given in section 4.4.

4.2 Numerical method

Simulation of gas–liquid two-phase flows is performed using the following assumptions:

(i) the mixture is a gas–liquid bubbly flow with small entrained bubbles;

(ii) the two phases are incompressible, and no phase change occurs;

(iii) the mass and momentum of the gas phase are very small and negligible, respectively, compared to those of the liquid phase; and

(iv) the bubbles conserve their spherical shape, and neither fragmentation nor coalescence occurs.

4.2.1 Basic equation

Based on these assumptions, the mass and momentum conservation equations for the liquid phase are explained as (Uchiyama and Yoshii, 2015b; Sokolichin and Eigenberger, 1997, 1999):

$$\frac{\partial \alpha_l}{\partial t} + \nabla \cdot (\alpha_l \boldsymbol{u}_l) = 0 \tag{4.1}$$

$$\alpha_l \frac{D\boldsymbol{u}_l}{Dt} = -\frac{1}{\rho_l}\nabla p + \nu_l \nabla^2 \boldsymbol{u}_l + \alpha_l \boldsymbol{g} \tag{4.2}$$

where,

$$\frac{D\boldsymbol{u}_l}{Dt} = \frac{\partial \boldsymbol{u}_l}{\partial t} + \left(\boldsymbol{u}_l \cdot \nabla\right)\boldsymbol{u}_l \tag{4.3}$$

and α_l is the liquid volume fraction, which correlates with the gas volume fraction α_g by

$$\alpha_l + \alpha_g = 1 \tag{4.4}$$

The momentum equation for the motion of an individual spherical bubble, proposed by Auton et al. (1988), reviewed by Sridhar and Katz (1995), and employed in the semi-L–L model in previous investigations, is expressed as

$$\rho_g V_b \frac{d\boldsymbol{u}_g}{dt} = \boldsymbol{F}_B + \boldsymbol{F}_D + \boldsymbol{F}_L + \boldsymbol{F}_{VM} + \boldsymbol{F}_P \tag{4.5}$$

where $\boldsymbol{F}_B$, $\boldsymbol{F}_D$, $\boldsymbol{F}_L$, $\boldsymbol{F}_{VM}$, and $\boldsymbol{F}_P$ are forces acting upon a spherical bubble and have been expressed by Sridhar and Katz (1995), as shown in section 2.2.2. Eq. (4.5) can then be rewritten as follows:

$$\frac{d\boldsymbol{u}_g}{dt} = \frac{1+C_V}{\beta+1}\frac{D\boldsymbol{u}_l}{Dt} - \frac{1}{\beta+C_V}\frac{3C_D}{4d_b}|\boldsymbol{u}_g - \boldsymbol{u}_l|\left(\boldsymbol{u}_g - \boldsymbol{u}_l\right) + \frac{\beta-1}{\beta+C_V}\boldsymbol{g} - \frac{C_L}{\beta+C_V}\left(\boldsymbol{u}_g - \boldsymbol{u}_l\right)\times(\nabla\times\boldsymbol{u}_l) \tag{4.6}$$

where β is the density ratio between the gas and liquid phases and the virtual-mass and the lift coefficients on a spherical bubble, C_V and C_L, respectively, moving at low Reynolds numbers, equal 0.5. The drag coefficient on a spherical bubble is calculated as (Uchiyama and Yoshii, 2015b; Sridhar and Katz, 1995)

$$C_D = \frac{24}{Re_b}\left(1 + 0.15 Re_b^{0.687}\right) \tag{4.7}$$

where $Re_b = d_b|\boldsymbol{u}_g - \boldsymbol{u}_l|/\nu_l$. The Lagrangian trajectory of an individual spherical bubble is calculated as

$$\frac{d\boldsymbol{x}_g}{dt} = \boldsymbol{u}_g \tag{4.8}$$

When a bubble rises in the liquid, its shape can be deformed with time. This deformation is dominated by Reynolds number ($Re_b = u_t d_b/\nu$), Bond number ($Bo = \rho_l g d_b/\sigma_s$), density and viscosity ratios of two phases, and initial bubble shape (Hua and Lou, 2007). Herein, u_t is the terminal velocity of a single bubble rising in the liquid, σ_s is interfacial tension. The trajectory of the bubbles depends on the level of deformation and their shape after deformed. For example, the ellipsoidal bubbles of a mean diameter of d_b = 4.4-5.6 mm move in a zigzag fashion in the investigation by Wang and Socolofsky (2015). Tomiyama et al. (2002) investigated the bubbles of diameters of $d_b = 2-4$ mm and showed that the bubbles move in either from small zigzag to large zigzag or helical fashions or from small to large helical fashions. The above investigations can capture well the bubble deformation with their rising; however, number of bubbles investigated to be limited less than 100. Hua and Lou (2007) reported that with $Re_b < 1$ or $Bo < 1$ the bubbles rise in a steady (not zigzag or helical) fashion and their spherical shape remain unchanged over time evolution.

In the current investigation, Re_b of a single bubble of a diameter of $d_b = 0.054$ mm is calculated as 0.084. Therefore, the bubble is assumed to be maintained in the spherical shape and moves in a steady fashion. In addition, the flow moving at $Re = 0.084 \ll 1$ with uniform at far field is considered as Stokes flow (creeping flow) which has no wake induced behind the sphere. In the case of multiple bubbles, the wake behind each sphere is probably narrow, weak, and steady. The interaction of these wakes is not strong enough to induce turbulence which spreads the bubbles. Therefore, the above-mentioned assumptions are acceptable, and the Eqs. (4.5) and (4.8) are applicable for the current simulation. In Eqs. (4.5) and (4.8), the rotational motion of the bubble around its centerline is also ignored. In the current model, the gas volume fraction is applied; this means that the bubble size must be smaller than the cell size. The flow scale at the bubble diameter is not resolved. The current model is appropriate for the present simulation condition of a continuous release of the extremely small bubbles from the tank bottom and can handle the high computational cost when number of released bubbles reach 10^6.

4.2.2 Vorticity and velocity orthogonal decomposition

Taking the curl of both sides of Eq. (2), the vorticity–velocity equation for the liquid phase is derived as

$$\frac{\partial \boldsymbol{\omega}}{\partial t} + (\boldsymbol{u}_l \cdot \nabla)\boldsymbol{\omega} = (\boldsymbol{\omega} \cdot \nabla)\boldsymbol{u}_l + \frac{\nu_l}{\alpha_l}\nabla^2\boldsymbol{\omega} + \frac{1}{\alpha_l}\nabla\alpha_l \times \left(\boldsymbol{g} - \frac{D\boldsymbol{u}_l}{Dt}\right) \tag{4.9}$$

where the vorticity field is defined as

$$\boldsymbol{\omega} = \nabla \times \boldsymbol{u}_l \tag{4.10}$$

Based on Helmholtz's theorem, the liquid velocity field is resolved into the sum of an irrotational vector field $\nabla\phi$ and a solenoidal vector field $\nabla\boldsymbol{\psi}$ as follows:

$$\boldsymbol{u}_l = \nabla \times \boldsymbol{\psi} + \nabla\phi \tag{4.11}$$

The $\boldsymbol{\psi}$ is a solenoidal vector field, where

$$\nabla \cdot \boldsymbol{\psi} = 0 \tag{4.12}$$

Taking the curl of Eq. (4.11) and substituting Eq. (4.12) into the resultant equation, the vector Poisson equation for $\boldsymbol{\psi}$ is derived as

$$\nabla^2\boldsymbol{\psi} = -\boldsymbol{\omega} \tag{4.13}$$

The Poisson equation for ϕ can then be obtained by substituting Eq. (4.11) into Eq. (4.1) and using the property $\nabla \cdot (\nabla \times \boldsymbol{\psi})$:

$$\frac{\partial \alpha_l}{\partial t} + \alpha_l\nabla^2\phi + (\nabla\phi + \nabla \times \boldsymbol{\psi}) \cdot \nabla\alpha_l = 0 \tag{4.14}$$

4.2.3 Vortex-in-cell method for a bubbly flow

The VIC method discretizes the liquid flow into vortex particles p with location $\boldsymbol{x}_p$ moving at a speed of $\boldsymbol{u}_l(\boldsymbol{x}_p)$ and carrying vorticity of $\boldsymbol{\omega}$. The vorticity–velocity equation, Eq. (4.9), can then be rewritten in the Lagrangian form of vortex particles as follows:

$$\frac{d\boldsymbol{x}_p}{dt} = \boldsymbol{u}_l(\boldsymbol{x}_p) \tag{4.15}$$

$$\frac{d\boldsymbol{\omega}_p}{dt} = \big(\boldsymbol{\omega}(\boldsymbol{x}_p)\cdot\nabla\big)\boldsymbol{u}_l(\boldsymbol{x}_p) + \frac{\nu_l}{\alpha_l}\nabla^2\boldsymbol{\omega}(\boldsymbol{x}_p) + \frac{1}{\alpha_l}\nabla\alpha_l \times \left(\boldsymbol{g} - \frac{D\boldsymbol{u}_l(\boldsymbol{x}_p)}{Dt}\right) \tag{4.16}$$

At the outset, the vortex particles are arranged on the grid nodes. Their velocity, $\boldsymbol{u}_l(\boldsymbol{x}_p)$, is calculated using Eq. (4.11), while $\boldsymbol{\psi}$ and ϕ are obtained through solving Poisson Eqs. (4.13) and (4.14), respectively. The vorticity field, $\boldsymbol{\omega}$, in Eq. (4.13) is obtained by solving Eq. (4.16). The vortex particles carrying their vorticity $\boldsymbol{\omega(x_p)}$ move to a new Lagrangian location, $\boldsymbol{x}_p$, due to the convection term, Eq. (4.15). Subsequently, these vortex particles are redistributed on grid nodes, $\boldsymbol{x}_q$. The vorticity of the vortex particles on the grid node is interpolated from their values at the Lagrangian locations as follows:

$$\boldsymbol{\omega}(\boldsymbol{x}_q) = \sum_{p}^{N_p} \boldsymbol{\omega}_p W\Big(\frac{x_q - x_p}{\Delta x}\Big) W\Big(\frac{y_q - y_p}{\Delta y}\Big) W\Big(\frac{z_q - z_p}{\Delta z}\Big) \tag{4.17}$$

where N_p is the number of vortex particles, Δx, Δy, and Δz are cell widths, and W is a third-order accurate kernel-interpolation function, as shown in detail in Section A.2.2 of Appendix A.

4.2.4 Calculation of gas volume fraction

The gas volume fraction on the grid nodes is calculated as follows:

$$\alpha_g(\boldsymbol{x}_q) = \sum_{b}^{N_b} \frac{V_b}{\Delta x\Delta y\Delta z} W_\alpha\Big(\frac{x_q - x_g}{\Delta x}\Big) W_\alpha\Big(\frac{y_q - y_g}{\Delta y}\Big) W_\alpha\Big(\frac{z_q - z_g}{\Delta z}\Big) \tag{4.18}$$

where N_b is the number of bubbles and W_α is triangular function explained as (Cottet and Koumoutsakos, 2000)

$$W_\alpha(\varepsilon) = \begin{cases} 0 & \text{if } |\varepsilon| > 1 \\ 1 - |\varepsilon| & \text{if } |\varepsilon| \le 1 \end{cases} \tag{4.19}$$

The use of the function has several benefits: (i) the calculated gas volume fraction is in the range of $0 - 1$, (ii) the sum of the volume of bubbles is conserved on the grid nodes, and (iii) the volume impact of a bubble on its position is itself.

4.2.5 The immersed boundary method

To simulate flows through the human heart, Peskin (1972) introduced the IB method for no-slip conditions. Subsequently, Cottet and Poncet (2002) proposed a VIC method combined with the penalization method, a type of IB method, to simulate flow around

a solid body. In the proposed scheme, the penalization method was employed to enforce the no-slip condition upon the liquid phase at the fluid–solid interface. When using the penalization method, the vorticity–velocity equation, Eq. (4.16), is rewritten as

$$\frac{d\boldsymbol{\omega}_p}{dt} = \big(\boldsymbol{\omega}(\boldsymbol{x}_p)\cdot\nabla\big)\boldsymbol{u}_l(\boldsymbol{x}_p) + \frac{\nu_l}{\alpha_l}\nabla^2\boldsymbol{\omega}(\boldsymbol{x}_p) + \frac{1}{\alpha_l}\nabla\alpha_l\times\Big(\boldsymbol{g} - \frac{D\boldsymbol{u}_l(\boldsymbol{x}_p)}{Dt}\Big) + \nabla\times\Big[\lambda\chi_s\Big(\boldsymbol{u}_s - \boldsymbol{u}(\boldsymbol{x}_p)\Big)\Big] \tag{4.20}$$

where λ is the penalization parameter, $\boldsymbol{u}_s$ is the velocity of the solid, and the function χ_s identifies the solid and fluid regions. The penalization velocity and vorticity are calculated as detailed in Section 2.3.4

$$\boldsymbol{u}_\lambda = (1-\chi_s)\boldsymbol{u} + \chi_s\boldsymbol{u}_s \tag{4.21}$$

$$\boldsymbol{\omega}_{\boldsymbol{\lambda}} = \boldsymbol{\omega} + \nabla\times(\chi_s(\boldsymbol{u}_s - \boldsymbol{u}_l)) \tag{4.22}$$

4.2.6 The convective outflow boundary condition for the liquid phase

The convective outflow condition (Yoshida et al., 2003; Xu and Lin, 2007) is enforced for the liquid phase at the far field and outlet. This condition neglects the effects of vortex diffusion and stretching and supposes that the liquid flow only convects at the concerned boundary. A general form of this boundary condition is expressed as

$$\frac{\partial f(\boldsymbol{x},t)}{\partial t} + u_c(\boldsymbol{x},t)\big[\nabla(f(\boldsymbol{x},t))\cdot\hat{n}\big] \tag{4.23}$$

where $f(\boldsymbol{x},t)$ are flow quantities convected at a scalar velocity $u_c(\boldsymbol{x},t)$ on the boundary $\partial\Omega$ and $\hat{n}$ is the unit normal vector of the surface $\partial\Omega$. This condition is applied for the vorticity $\boldsymbol{\omega}$, vector potential $\boldsymbol{\psi}$, scalar potential ϕ, and liquid velocity $\boldsymbol{u}_l$ fields, with which they are boundary conditions of the momentum equation (4.16), Poisson equations (4.13) and (4.14), and equation (4.11), respectively. Applying this boundary condition for the simulation is expressed in a more detail, as shown in Appendix C.

4.2.7 Slip conditions for bubbles on the surface of the cylinder

The slip conditions for the bubbles on the cylinder surface are employed as (Sugiyama et al., 2001). Figure 4.1 shows an analysis of a bubble velocity on the cylinder surface. A gas bubble was considered to be located on the cylinder surface with a position $\boldsymbol{x}_g = (x_g, y_g, z_g)$ and velocity $\boldsymbol{u}_g = (u_g, v_g, w_g)$. When this bubble slips on the cylinder surface, normal component of its velocity u_{g-n} with respect to the cylinder surface is forced to zero, and the tangential components on the $x-z$ plane $u_{g-\tau}$ and along the y-direction v_g remain unchanged. The components of the bubble velocity are recalculated as

$$\begin{cases} u_g = u_g\sin(\alpha_g)\sin(\alpha) + w_g\sin(\alpha)\cos(\alpha) \\ v_g = v_g \\ w_g = w_g\sin(\alpha)\cos(\alpha) + w_g\cos(\alpha)\cos(\alpha) \end{cases} \tag{4.24}$$

where $\alpha = \arctan((h_0 - z_g)/x_g)$

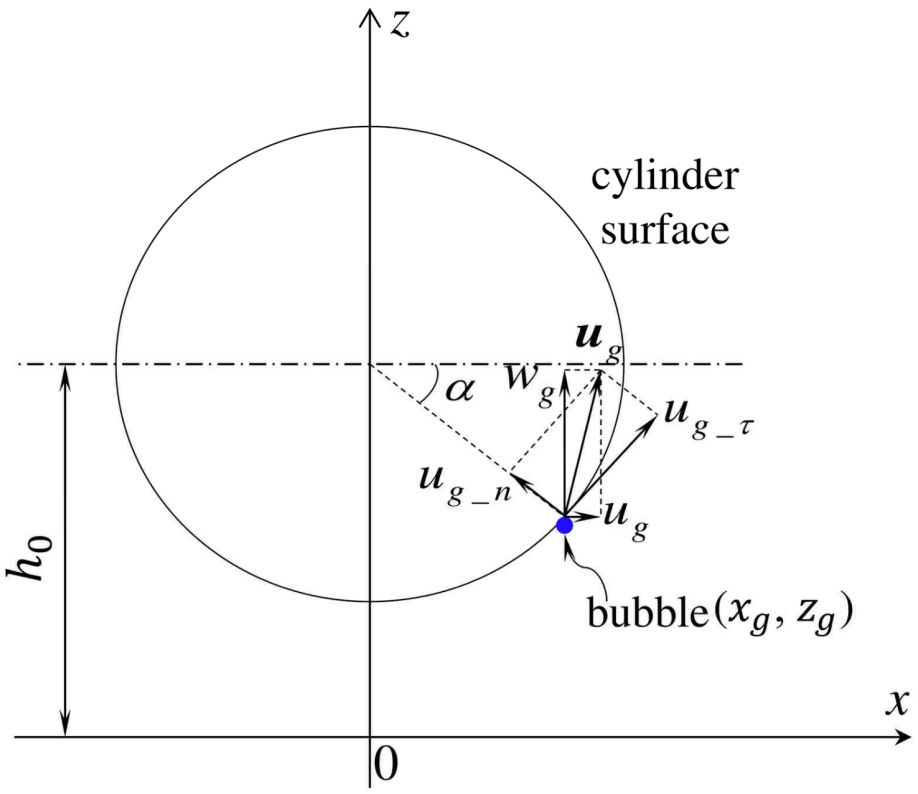

Figure 4.1: Bubble velocity at a random point on the cylinder surface

4.2.8 Numerical procedures

Given a flow at time t, the flow at $t + \Delta t$ was calculated by the following procedure:

(1) Calculate the bubble velocity $\boldsymbol{u}_g$ using the momentum equation of the bubble, Eq. (4.6).

(2) Recalculate the bubble velocity $\boldsymbol{u}_g$ using Eq. (4.24) to implement the slip condition of the bubble on the cylinder surface;

(3) Calculate the Lagrangian trajectory of the bubble $\boldsymbol{x}_g$ using Eq. (4.8).

(4) Calculate the gas and liquid volume fractions, α_g and α_l, using Eqs. (4.18) and (4.4), respectively.

(5) Calculate the vorticity of the vortex particle $\boldsymbol{\omega}(\boldsymbol{x}_p)$ using Eq. (4.16) to account for the vortex stretching, diffusion, and the effect of external sources.

(6) Calculate the vortex-particle convection $\boldsymbol{x}_p$ using Eq. (4.15).

(7) Redistribute the vortex particle $\boldsymbol{\omega}(\boldsymbol{x}_p)$ from the Lagrangian to Eulerian points using Eq. (4.17).

(8) Calculate the vector-potential velocity $\boldsymbol{\psi}$ using Eq. (4.13).

(9) Calculate the scalar-potential velocity ϕ using Eq. (4.14).

(10) Calculate the liquid velocity $\boldsymbol{u}_l$ using Eq. (4.11).

(11) Calculate the corrected vorticity field $\boldsymbol{\omega}_{corrected}$ using Eq. (4.10).

(12) Calculate the penalization velocity $\boldsymbol{u}_\lambda$ using Eq. (4.21) to enforce the no-slip condition of the liquid phase on the cylinder surface.

(13) Calculate the penalization vorticity $\boldsymbol{\omega}_\lambda$ using Eq. (4.22).

4.3 Results and discussions

4.3.1 The evolution of a single vortex ring

The evolution of a vortex ring was simulated to verify the application of the outflow condition of the liquid flow at the outlet. In this case, the momentum equation for the liquid phase, Eq. (4.20), is rewritten as

$$\frac{d\boldsymbol{\omega}_p}{dt} = \big(\boldsymbol{\omega}(\boldsymbol{x}_p)\cdot\nabla\big)\boldsymbol{u}_l(\boldsymbol{x}_p) + \nu_l\nabla^2\boldsymbol{\omega}(\boldsymbol{x}_p) \tag{4.25}$$

At the outlet, $u_c(\boldsymbol{x},t)$ was calculated as

$$u_c(z_{max}) = Max\big(u_z(x,y,z_{max},t)\big) \tag{4.26}$$

The vortex ring at the outset was expressed through a Gaussian function as

$$\omega_\theta = \frac{\Gamma_0}{\pi\sigma^2}e^{-\frac{\rho^2(x,y,z)}{\sigma^2}} \tag{4.27}$$

where $\rho^2(x,y,z) = \big(R-\sqrt{x^2+y^2}\big)^2 + (z-z_0)^2$. The vortex ring had a diameter of $D = 60$ mm, a radius of a core radius of $R = D/2$ and an initial circulation of Γ_0 at initial position of $z_0 = 2D$, moving at a Reynolds number, $Re_\Gamma = \Gamma_0/\nu$, of 8,063. The kinematic viscosity, ν, was 1 mm^2/s. The domain of $(-2D,2D)\times(-2D,2D)\times(0,4D)$ was divided into $160\times160\times160$ cube cells. The non-dimensional time step, $\Delta t^* = \Delta t(\Gamma_0/R^2)$, was set as 0.0089.

In Fig. 4.2, the vortex ring reached the top surface at $t^* = 17.8$ and then continued to move through this surface at $t^* = 18.69$. At $t^* = 22.25$, only the streak of the vortex ring was observed, and it diffused gradually with time. The streamlines of the liquid flow on the x-z plane passing through the ring center at $t^* = 0$, 8.9, and 18.69 were shown in Fig. 4.3. The vortex ring was not deformed as it moved through the top surface. This boundary did not affect the evolution of the vortex ring, thus indicating that the applied convective condition of the proposed method was proper. A comparison of the profiles of the liquid velocity calculated by the proposed simulation and experimental work done by Uchiyama and Kusamichi (2013), shown in Fig. 4.4, indicates good agreement between the two.

Moreover, the translational velocities of the experimental and simulated vortex ring were then compared, where the translational velocity of the experimental vortex ring was given by Weigand and Gharib (2007) as

$$U_T = \frac{\Gamma_0}{4\pi R}\Big(ln\frac{8R}{\sigma} - 0.558\Big) \tag{4.28}$$

The translational velocity of the ring with the above-mentioned parameters obtained through Eq. (4.28) is 65.4 mm/s, whereas that calculated by the simulation is 61.02 mm/s. The relative error between these results is 6.7 %. Therefore, the proposed method was deemed suitable for reproducing the flow characteristics.

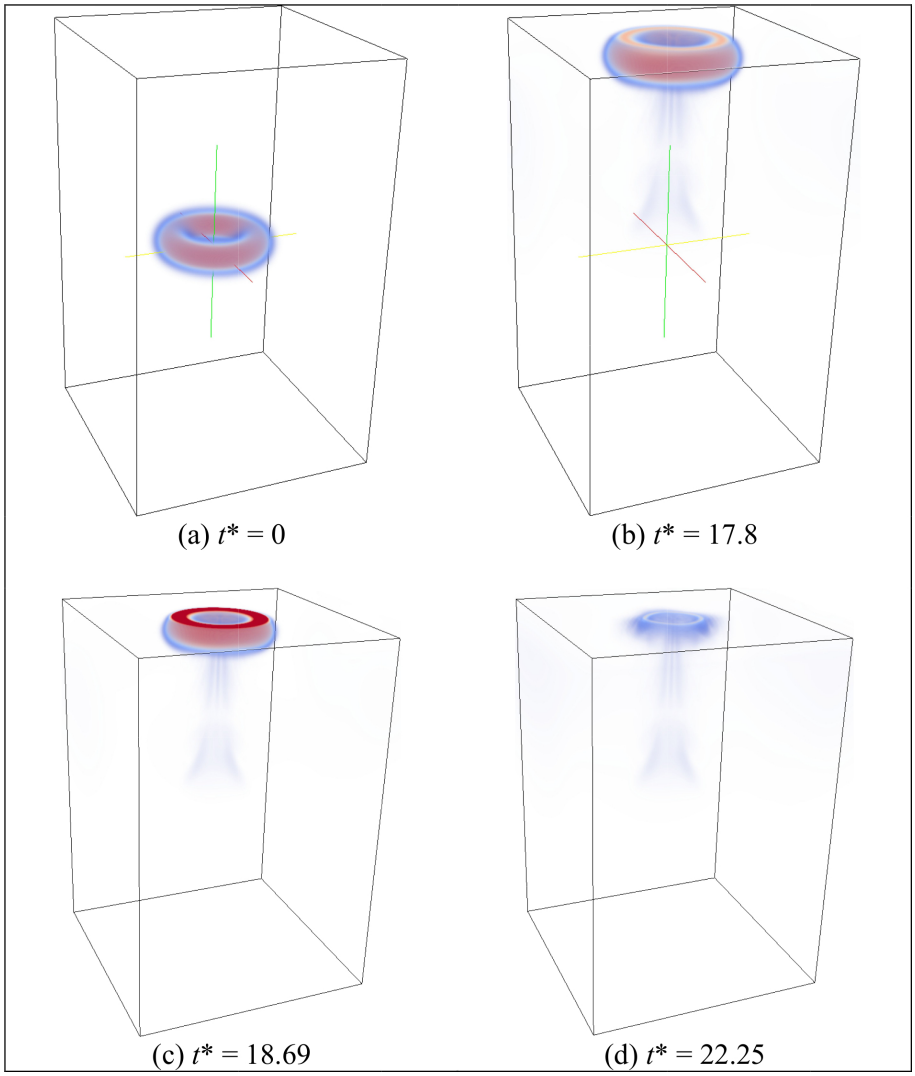

Figure 4.2: Time evolution of a vortex ring at $Re_\Gamma = 8,063$

4.3.2 The collision of a vortex ring with a cylinder

The collision of a vortex ring with a cylinder was then simulated to verify the application of the penalization method for the no-slip condition of the liquid flow at the solid surface. In this case, the vorticity–velocity equation for the liquid phase, Eq. (4.20), is rewritten as

$$\frac{d\boldsymbol{\omega}_p}{dt} = \big(\boldsymbol{\omega}(\boldsymbol{x}_p)\cdot\nabla\big)\boldsymbol{u}_l(\boldsymbol{x}_p) + \nu_l\nabla^2\boldsymbol{\omega}(\boldsymbol{x}_p) + \nabla\times\Big[\lambda\chi_s\big(\boldsymbol{u}_s - \boldsymbol{u}(\boldsymbol{x}_p)\big)\Big] \tag{4.29}$$

The domain of $(-3D, 3D)\times(-3D, 3D)\times(0, 6D)$ was discretized into $90\times90\times90$ cube cells. The cylinder had a diameter of $D = 2$ and a length of $6D$ and was placed at a distance of $3D$ from the bottom. The vortex ring had a radius of $1.4R$ ($R = D/2$), a core radius of $\sigma = 0.5R$, and an initial circulation of $\Gamma_0 = 1$, moving vertically downward at $Re_\Gamma = 400$ to collide with the cylinder. At the outset, the vortex ring was expressed using a Gaussian function (Poncet, 2001) as

$$\omega_\theta = \frac{\Gamma_0}{2\pi\sigma^2}e^{-\frac{\rho^2(x,y,z)}{2\sigma^2}} \tag{4.30}$$

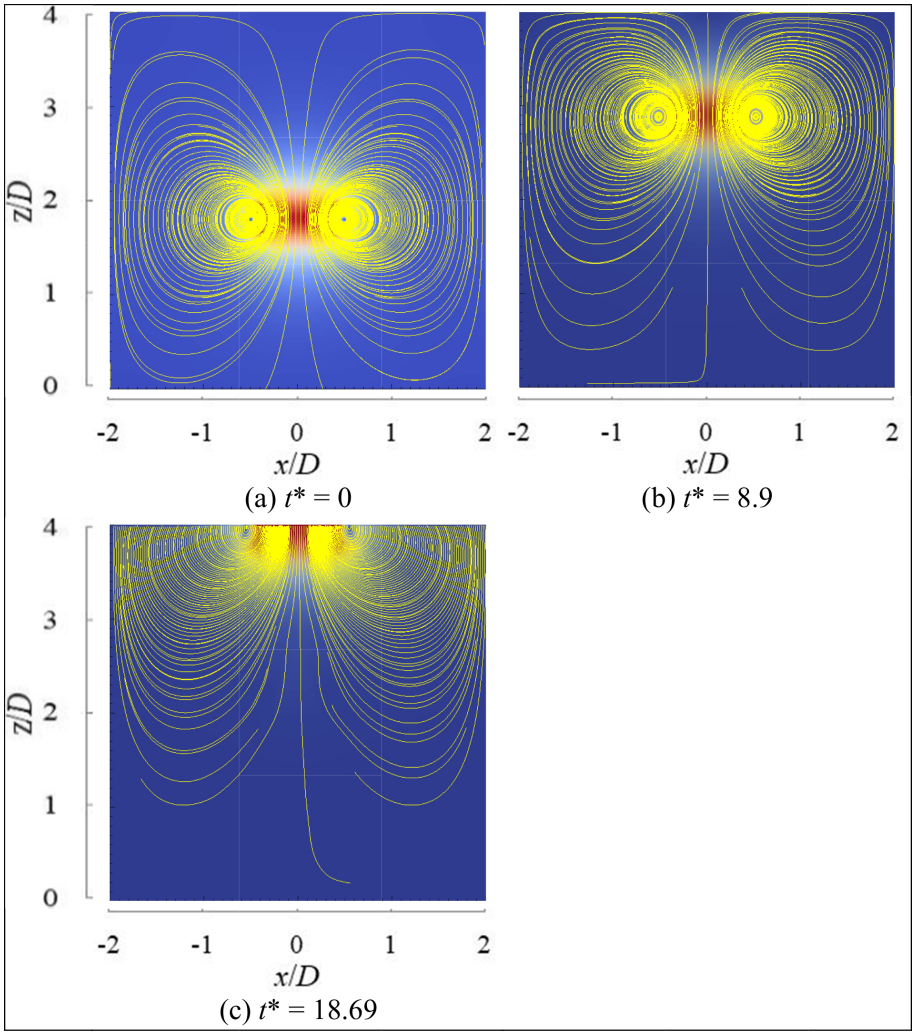

Figure 4.3: Time evolution of the streamline flow on the x-z plane

The initial distance between the vortex ring and the cylinder center was $2.5R$. The non-dimensional time step, $\Delta t^* = \Delta t(\Gamma_0/R^2)$, was set to 0.005.

The time evolution of the collision of the vortex ring with the cylinder is compared with that of numerical work by (Poncet, 2001; Cottet and Poncet, 2002) in Figs. 4.5 and 4.6, respectively. The second vortex was formed as the vortex ring moves forward to the cylinder, and the ring was deformed gradually with time. The results agreed well with the existing results at six time-points. Thus, the employed penalization method was deemed appropriate for simulating flow around the cylinder.

4.3.3 The bubbly flow around a cylinder

The conditions of the simulation were set similar to those of the experiment. Figure 4.7 shows a configuration of the flow condition at the outset. The circular cylinder had a diameter of $D = 30$ mm and a length of $L = 8D$ and was placed at a distance of $5D$

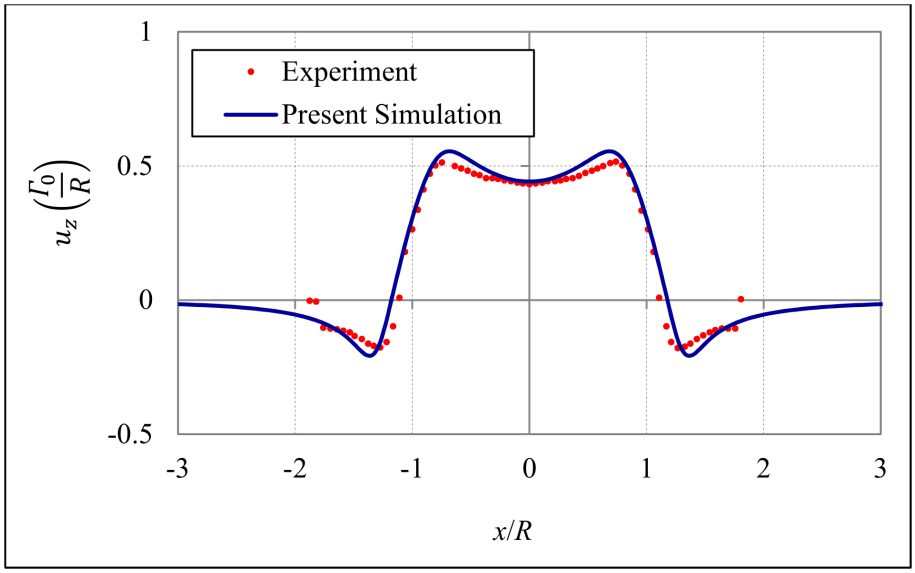

Figure 4.4: Liquid velocity along a horizontal line passing through the ring center at $t^* = 8.9$. The dotted red and solid blue lines show the results obtained by the proposed simulation and Uchiyama and Kusamichi (2013)

from the bottom. The domain of $(-4D, 4D) \times (-4D, 4D) \times (0, 16D)$ was divided into $80 \times 80 \times 160$ cube cells. At the bottom, five bubble injection lines were arranged regularly. The bubble flow rates released from injection lines 1, 3, and 5 $(Q_i, i = 1, 3, 5)$ were $4Q/14$, whereas those released from injection lines 2 and 4 $(Q_i, i = 2, 4)$ were $Q/14$, in which the total bubble flow rate $Q = \sum Q_i$ was 6.4 mm^3/s. When the bubbly flow fully developed, the number of the bubbles reached 3.6×10^6. The bubble diameter was 0.054 mm and the liquid kinematic viscosity ν was 1 mm^2/s. The non-dimensional time step for the liquid was $\Delta t_b u_t / D = 7.75 \times 10^{-4}$, and that for the bubble was $\Delta t_l u_t / D = 7.75 \times 10^{-5}$, which complies with the formula of the bubble time-scale, $\tau_b = d_b^2/(36\nu_l)$. The terminal velocity of a single bubble of diameter of $d_b = 0.054$ mm rising in quiescent water was designated as u_t and was calculated as 1.55 mm/s. The Taylor–Reynolds (T–R) number was utilized to determine the appearance of the turbulence of the liquid flow induced by the bubbles and was 0.084. When the T–R number is smaller than 100, the turbulence of the liquid flow does not exist (Brocchini and Peregrine, 2001). Therefore, no discussion of the turbulent characteristics was performed in this investigation.

The bubbles used in the experiment were hydrogen and oxygen. These bubbles were generated by using electrolysis of water which was composed of the five rods (injection lines) arranged regularly at intervals of $0.7D$ along the x-axis at the tank bottom. Two rods were used as anodes, and the rest was used as cathodes. Small oxygen and hydrogen bubbles at the anodes and cathodes, respectively, were generated by applying a DC voltage between the electrodes. The bubble size could be controlled by changing the electrode curvature or rob diameter. An increase in rob diameter would give an increase in bubble size. The interfacial tension was assumed

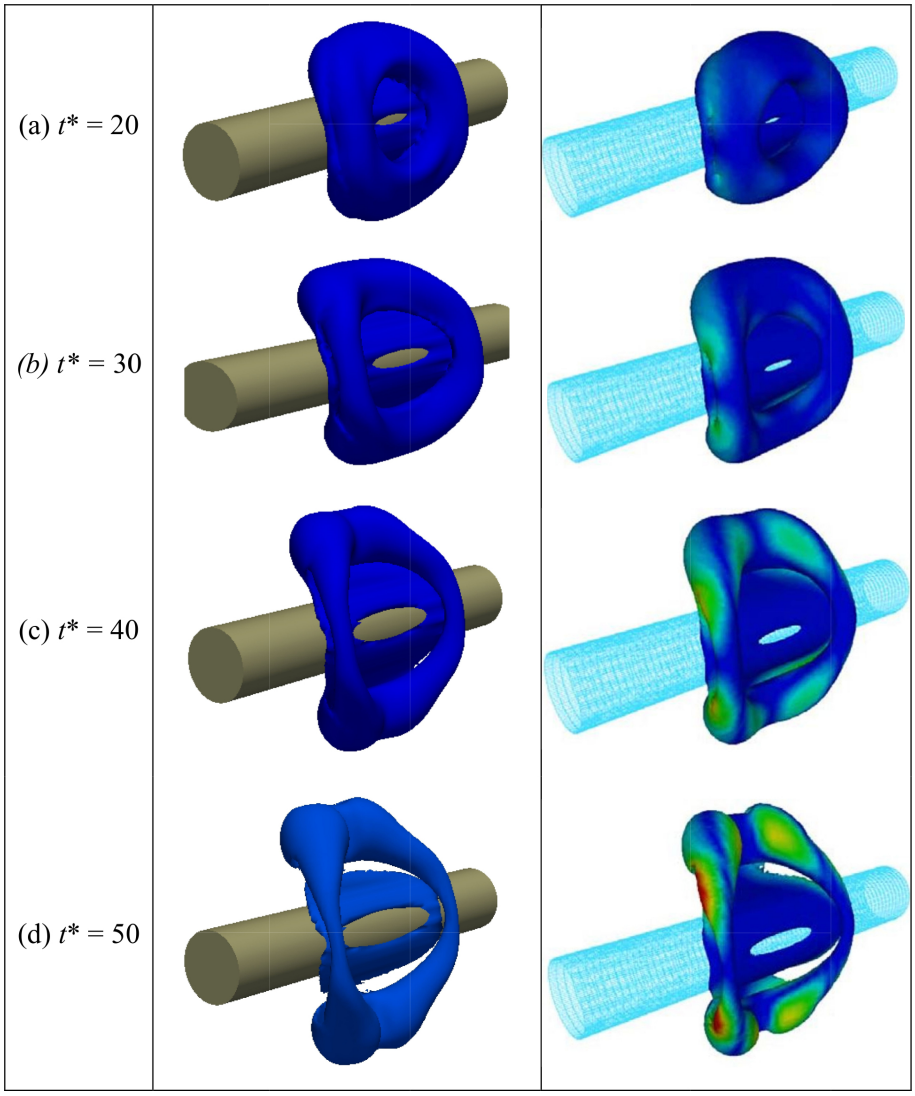

Figure 4.5: Front-side view of the time evolution of the collision of a vortex ring with a cylinder. Plots in upper and lower rows represent the results obtained by the present simulation and Poncet (2001), respectively. An isosurface of the vorticity magnitude, $|\boldsymbol{\omega}|R^2/\Gamma_0 = 0.1$, is plotted

to be high enough to maintain the spherical shape of the bubble of a diameter of $d_b = 0.054$ mm. The simulation of a bubble plume around a cylinder with small entrained bubbles is applicable to improve the design of finned coil and water to air heat exchangers.

The condition of the liquid phase at the bottom wall was a combination of no-slip and non-penetration conditions, as detailed in the investigation of annular bubble plume, whereas that at the sides and top was outflow. The $u_c(\boldsymbol{x}, t)$ at the top was calculated as

$$u_c(z_{max}, t) = \frac{1}{2}\Big[min\big(u_z(x, y, z_{max}, t)\big) + max\big(u_z(x, y, z_{max}, t)\big)\Big] \tag{4.31}$$

The scalar convective velocity at the sides was similarly computed.

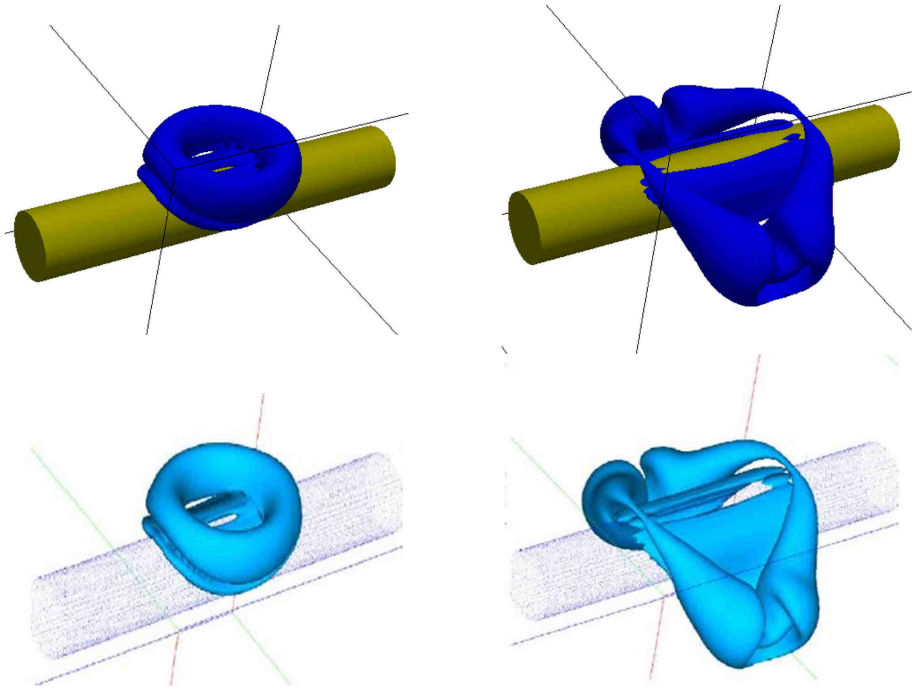

(a) $t^* = 10$ (b) $t^* = 60$

Figure 4.6: Front-top view of the time evolution of the collision of a vortex ring with a cylinder. Plots in upper and lower rows represent the results obtained by the present simulation and Cottet and Poncet (2002), respectively. An isosurface of the vorticity magnitude, $|\boldsymbol{\omega}|R^2/\Gamma_0 = 0.1$, is plotted

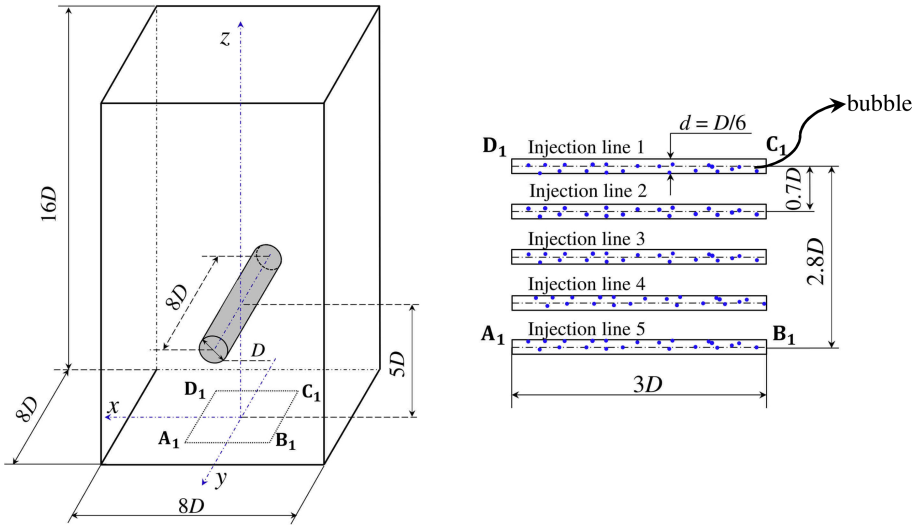

Figure 4.7: A configuration on the flow at the outset, where bubbles of a diameter $d_b = 0.054$ mm represented by blue dots are released randomly from five injection lines of a length $3D$ and a width $d = D/6$

The time evolution of the bubble distribution on the x-z plane captured by the proposed simulation and the experiment was shown in Figs. 4.8 and 4.10, respectively. The bubbles slightly shifted toward the y-z plane due to the effect of the liquid flow,

as shown at $t^* = 0.465$. The liquid flow rapidly reached the cylinder surface, moved around, then separated from both sides of the cylinder. The bubbles were entrained by the liquid flow to distribute around the cylinder surface and also separated from both sides of the cylinder to form bubble layers moving upwards. They were not entrained into the y-z plane, as shown at $t^* = 0.93$ and $t^* = 1.395$. When the flow fully developed, the bubbles were observed on the y-z plane but were not entrained into the region just behind the rear of the cylinder, as shown at $t^* = 1.86$. This region was twice as large as the cylinder's cross-section. Downstream, bubbles distributed into groups due to entrainment in induced vortices and dispersed over a large region of the domain. This phenomenon was also observed in the experimental investigations done by Murai et al. (2005) and Uchiyama and Ishiguro (2016). In general, at four time points, the bubble distribution on the x-z plane by the proposed simulation agreed with that by the experiment. The lateral dispersion of the bubbles by the simulation was higher than that by the experiment at $t^* = 1.395$ and 1.86. The differences can be explained that the concentration of the bubbles in the bubble layers was higher in other regions, leading to combination of some bubbles to form larger bubbles in the experiment, as can be seen at the region $z/D > 8$. However, these bubbles were assumed to be not so large that they could generate their own wakes which induced their motion in zigzag or helical fashions. The buoyancy force on these bubbles was higher than the entrainment by the vortex pair generated behind the cylinder or the weak induced-vortices of the liquid flow downstream of the cylinder. In other words, these bubbles moved in straight upward paths to the top surface. They generated the higher liquid shear layer, and these shear layers entrained the small bubbles to move upward, which resulted in a less spread of the bubbles downstream. In the simulation, the spherical shape of the bubbles was maintained, and no coalescence occurred. The small bubbles were affected significantly by the vortex pair and the weak induced-vortices downstream. Therefore, the spreading of the bubbles by the simulation was higher than that by the experiment.

Time evolution of the bubble distribution, liquid velocity, and induced vortices is shown on the x-z plane in Fig. 4.11. The liquid flow was generated in the form of plane shear layers shown at $t^* = 0.465$. These shear layers rapidly came into contact with the cylinder surface, moved around, and then separated from both sides of the cylinder shown at $t^* = 0.93$. Moreover, large-scale vortices were observed along the sides of the bubble plume in this period, due to an inhomogeneous distribution of the bubbles and the cylinder effects. The separated shear layers lost their stability and then interacted, as shown at $t^* = 1.395$ and 1.86, leading to a downstream formation of vortices of various scales. The observed bubble distribution in the region of high liquid velocity varied with the behavior of these shear layers.

Figure 4.12 shows the time evolution of the bubble distribution, liquid velocity, and induced vortices on the y-z plane. In the beginning, a bubble plume composed of five

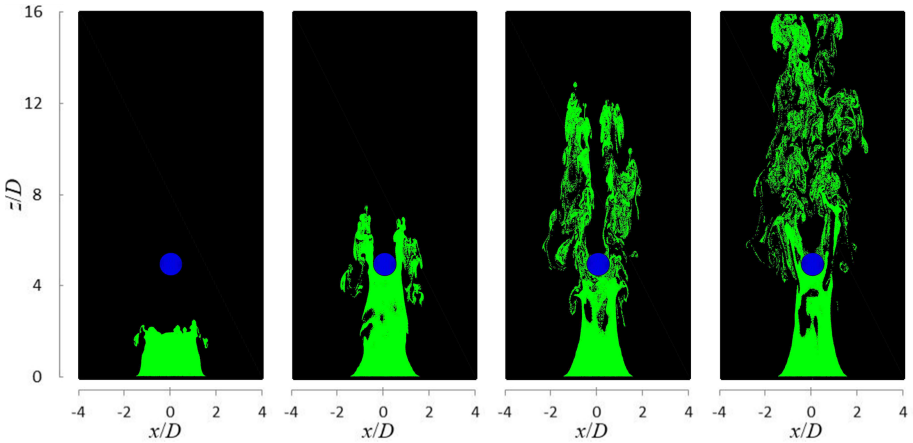

(a) t^* = 0.465 (b) t^* = 0.93 (c) t^* = 1.395 (d) t^* = 1.86

Figure 4.8: Time evolution of the bubble distribution on the x-z plane by the simulation, where bubbles are represented by green dots and the cylinder cross-section is represented by a blue area

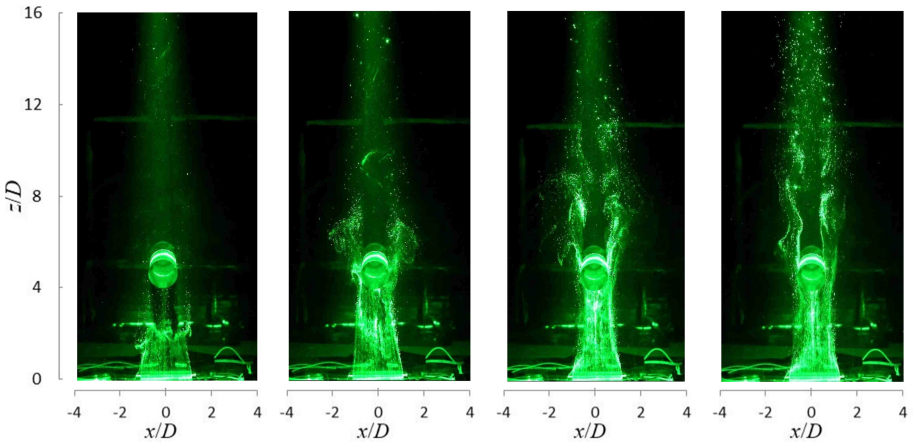

(a) t^* = 0.465 (b) t^* = 0.93 (c) t^* = 1.395 (d) t^* = 1.86

Figure 4.9: Time evolution of the bubble distribution on the x-z plane by the experiment

plane bubble plumes was generated from the five injection lines. The plane bubble plumes released from injection lines 1, 3 and 5 moved faster than those from injection lines 2 and 4 due to the difference in bubble flow rates, as shown at $t^* = 0.465$. These plane bubble plumes generated the plane shear layers with which they interacted. These shear layers rolled up to form vortices of various scales along these plane bubble plumes. Due to the symmetry with respect to the x-z plane, the shear layers formed by the plumes from injection lines 1, 2, 4 and 5 were deformed, while those from injection line 3 remained unchanged, as shown at $t^* = 0.93$. The bubbles were entrained into the shear layer paths. These shear layers combined, as shown at $t^* = 1.395$. In other words, the interaction between vortices leads to a coalescence of some vortices, and which then entrained the surrounding bubbles. From $t^* = 1.86$, the liquid flow was quasi-stable upstream and unstable downstream.

The gas volume fraction time evolution is shown in Fig. 4.12 to clarify the behavior

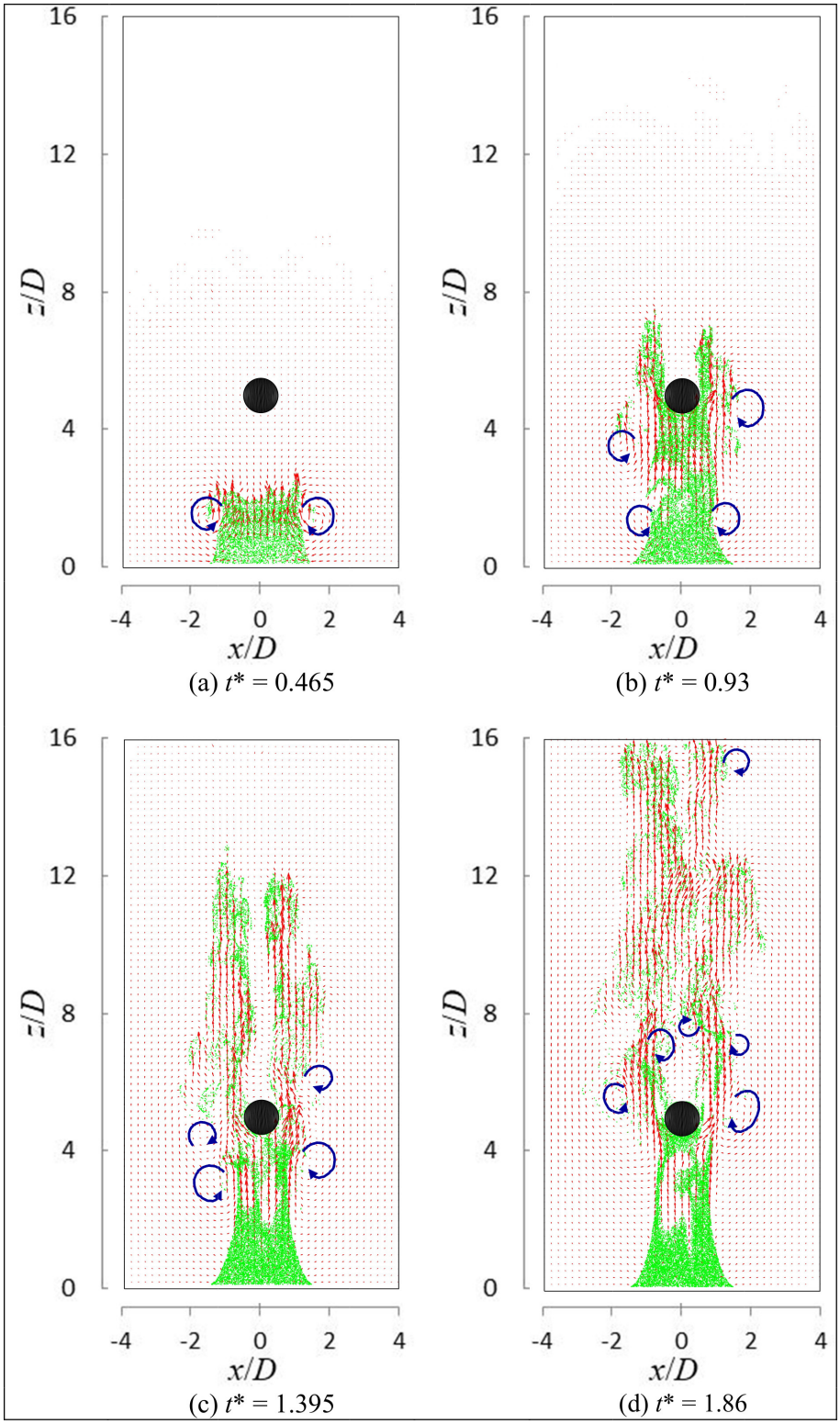

Figure 4.10: Time evolution of bubble distribution and liquid velocity on the x-z plane, where liquid velocity is represented by red vectors

of the bubble plume. The bubble plume was stable in the early stage, as shown at $t^* = 0.465$, followed by an unstable state due to the interaction between the plane shear layers, as shown at $t^* = 0.93$. As the bubbles moved over the cylinder, they were dispersed

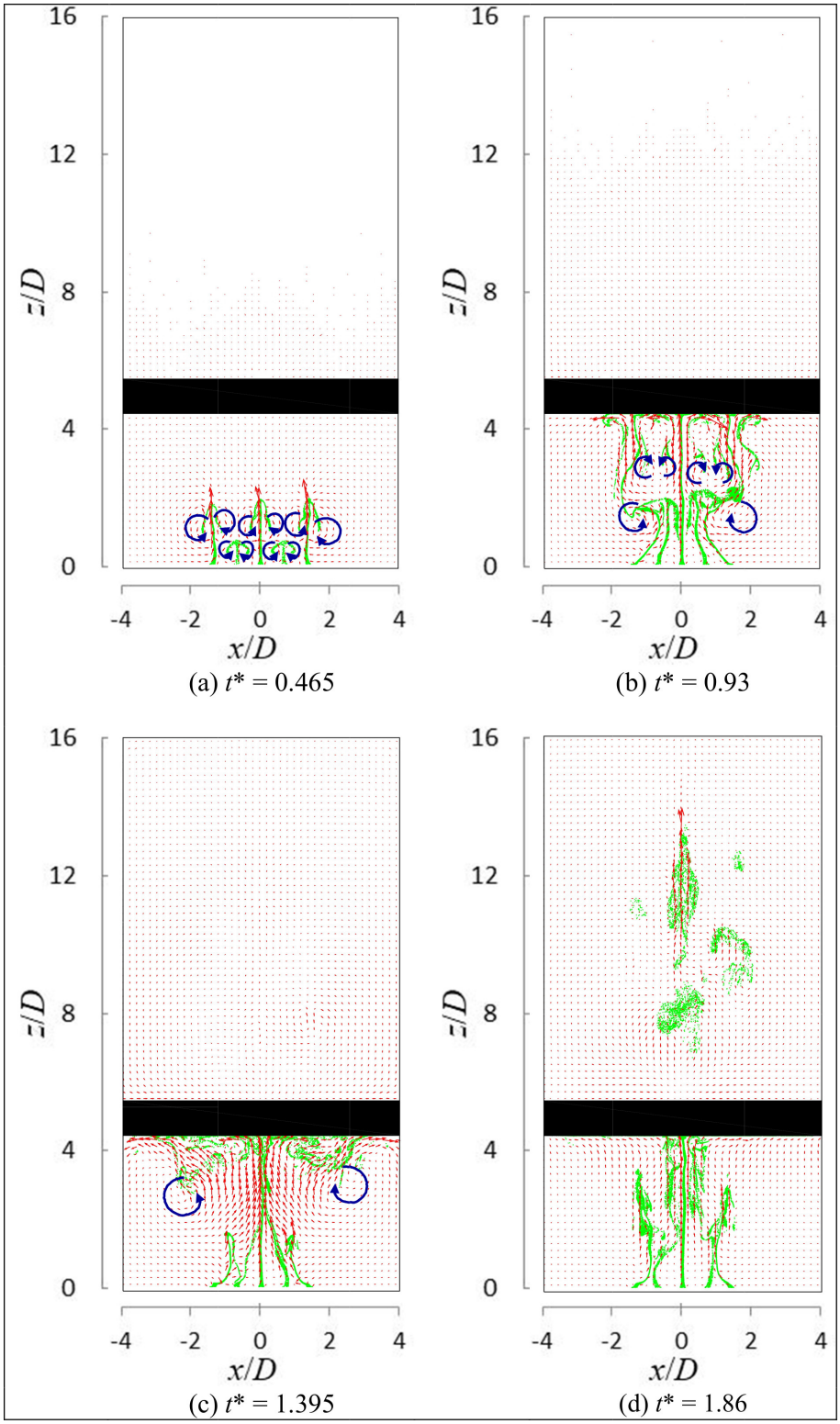

Figure 4.11: Time evolution of bubble distribution and liquid velocity on the y-z plane

downstream, where the gas volume fraction was, on average, about 0.0001, as shown at $t^* = 1.395$ and 1.86. When the flow fully developed, the bubble plume was quasi-stable upstream, but unstable downstream, as shown at $t^* = 1.86$. Moreover, in this stage, the bubbles accumulated in the shear layers separated from both sides of the cylinder to form

the bubble layers.

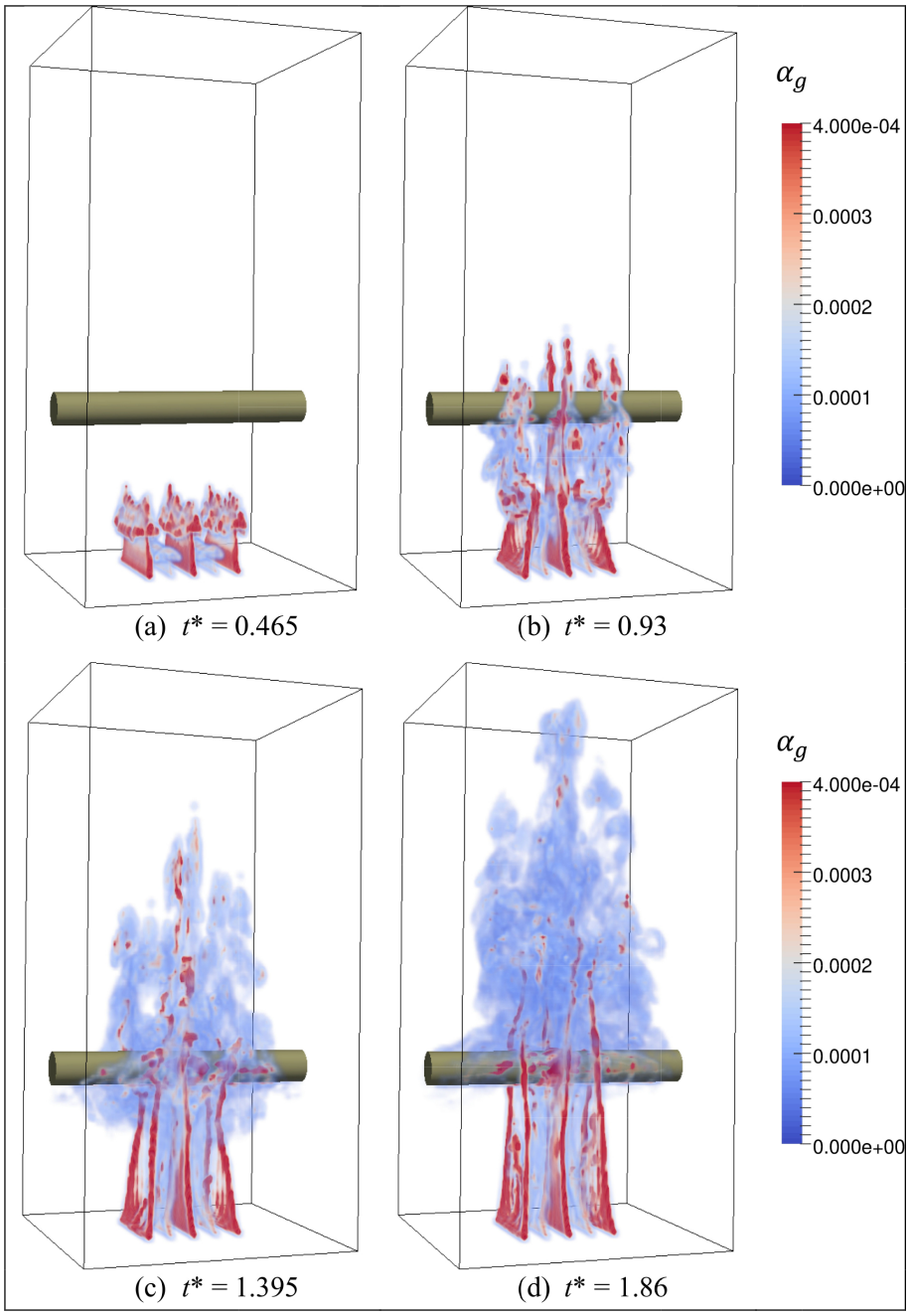

Figure 4.12: Time evolution of gas volume fraction

The time evolution of the vortex structure represented by the vorticity magnitude $|\boldsymbol{\omega}|$ and a vorticity component ω_z are shown in Figs. 4.13 and 4.14, respectively. The three-dimensional vortices, composed of three vorticity components, ω_x, ω_y, and ω_z, were formed when the bubbles were released from the bottom, as shown at $t^* = 0.465$. The interaction between vortices led to the formation of the three-dimensional large-scale vortices, which developed significantly when moved around the cylinder surface, as shown at $t^* = 0.93$. At $t^* = 1.395$ and 1.86, a three-dimensional vortex structure of various scales

was generated downstream. However, this structure disappeared gradually upstream, two-dimensional structure, composed of two vorticity components of ω_x and ω_y, appeared. The flow structure was quasi-stable upstream when the flow fully developed. The vortex structure pattern in this region was similar to the gas volume fraction pattern shown in Fig. 4.12. Moreover, the Karman vortex street did not appear downstream, unlike the case of the bubbly flow around the obstacle with generating a Reynolds number of the liquid flow in the inlet.

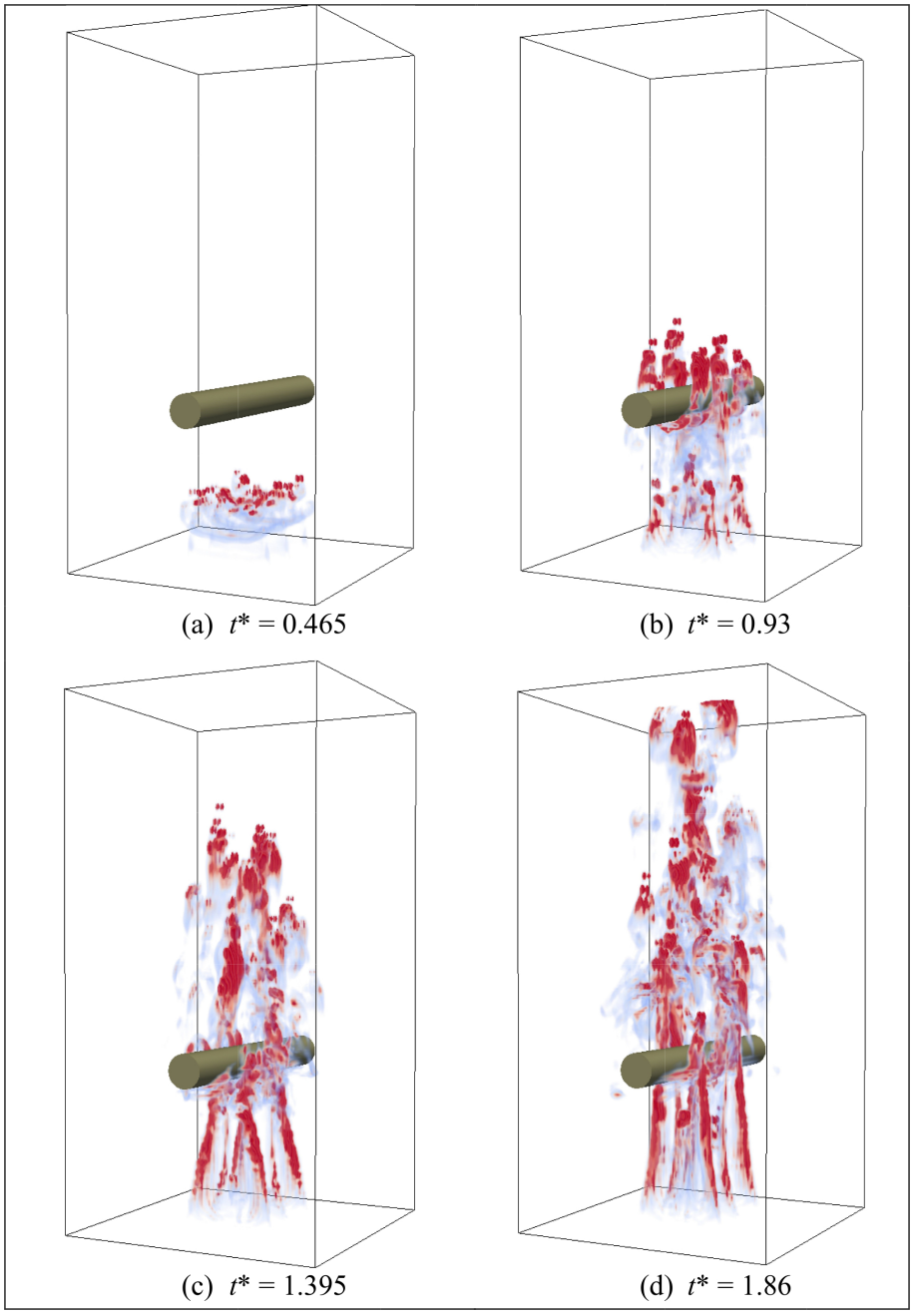

Figure 4.13: Time evolution of vorticity magnitude $|\boldsymbol{\omega}|$, where $|\boldsymbol{\omega}|(D/u_t)$ is plotted in a range of $29 - 58$

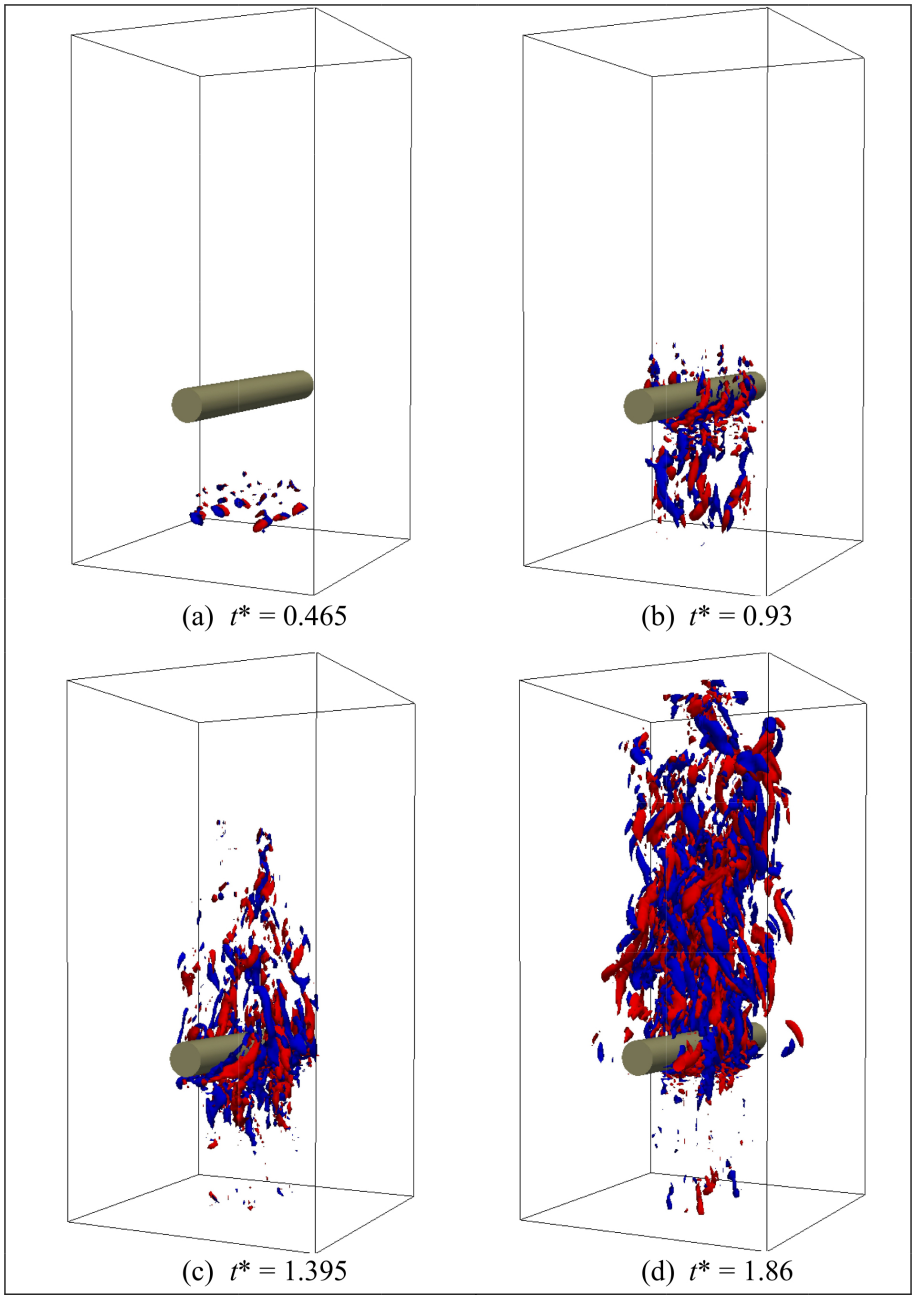

Figure 4.14: Time evolution of vorticity component ω_z, where $\omega_z(D/u_t) = \pm 19.35$ are represented by red and blue surfaces, respectively

The time evolution of the liquid velocity components, u_x, u_y, and u_z, is presented at four spatial points in Fig. 4.15. In general, the component u_z was about five times higher than those of u_x and u_y because of the appearance of an upward liquid flow induced by the bubbles. These velocity components were much higher than the terminal velocity. At point A, the velocity components fluctuated significantly from $t^* = 0.6$ to 1.86 when the bubble plume reached the cylinder and then moved around it. From $t^* = 1.86$, these velocity components were at a quasi-stable state, consistent with the observed characteristics of the vortex structure. At point B, all three components greatly fluctuated over the whole time evolution. This was likely because this point settled the

unstable shear layers that separated from either side of the cylinder. From $t^* = 0.93$ to 1.86, the frequency of oscillations of the components of u_x and u_y were higher than that of u_z due to the strong development of a three-dimensional vortex structure, as shown in Fig. 4.14. At point C, from the outset to $t^* = 2.0$, three velocity components fluctuated slightly due to a small effect of the bubble plume. The gas volume fraction at this point was very small compared with that at point B. However, from $t^* = 2.0$, the velocity components at point C oscillated significantly, caused by the horizontal spread of the shear layers separating from the cylinder. The velocity components at point D were very low compared to those at points A, B, and C, because point D was far from the region of the effects of the bubble plume. Moreover, from $t^* = 1.5$ to 2.7, an appearance of a weak reversed flow was observed at point D, likely caused by the formation of vortices beside the bubble plume due to an inhomogeneous bubble distribution. Additionally, these vortices diffused and stretched into vicinity regions, corresponding to the appearance of the liquid velocity in these regions. In the final stage, the liquid flow at point D moved upward. With the characteristics of the liquid velocity at points A, B, C, and D, the profiles of the time-averaged liquid velocity along horizontal lines passing through these points are not given, because they do not reflect the nature of the flow phenomenon.

Profiles of the gas volume fraction α_g and the vorticity magnitude $|\boldsymbol{\omega}|$ along a horizontal line at heights $z = 5D$ and $7D$ at $t^* = 1.395$ are shown in Fig. 4.16. The pattern of the gas volume fraction was similar to that of the vorticity magnitude. The number of peaks of the profile of α_g was the same with that of $|\boldsymbol{\omega}|$, and the peaks of α_g was near that of $|\boldsymbol{\omega}|$. This was attributable to the preference of the bubbles to accumulate in the region of high vorticity magnitude, generated from both sides of the cylinder, rather than the region of low vorticity magnitude on the vertical center plane of the cylinder. The peaks of the profile of the vorticity magnitude were vortex centers. Therefore, the bubbles tended to move to near the centers of vortices. This characteristic was also observed in the investigation of the interaction between a vortex ring and a bubble plume. They reported that the bubbles prefered to distribute near the core center of the vortex ring where has the highest value of the vorticity magnitude. The bubbles initialized near the core center were rapidly entrained, while the bubbles initialized far away took more time to distribute near the core center. The bubble trajectories were similar to two-dimensional helical shapes.

The time evolution of the ratio of the slip velocity, $|\boldsymbol{u}_l - \boldsymbol{u}_g|$, to the terminal velocity, u_t, of the bubbles on the x-z plane is shown in Fig. 4.17. In general, this ratio was almost in the range of $1 - 1.1$ units. This ratio was higher than 1.1 units when the bubbles were located in the region of high vorticity magnitude. This flow characteristic was also demonstrated in the investigation of the evolution of an annular bubble plume. From Figs. 4.15 and 4.17, the vertical velocities of the bubbles were shown to be greater than the terminal velocity.

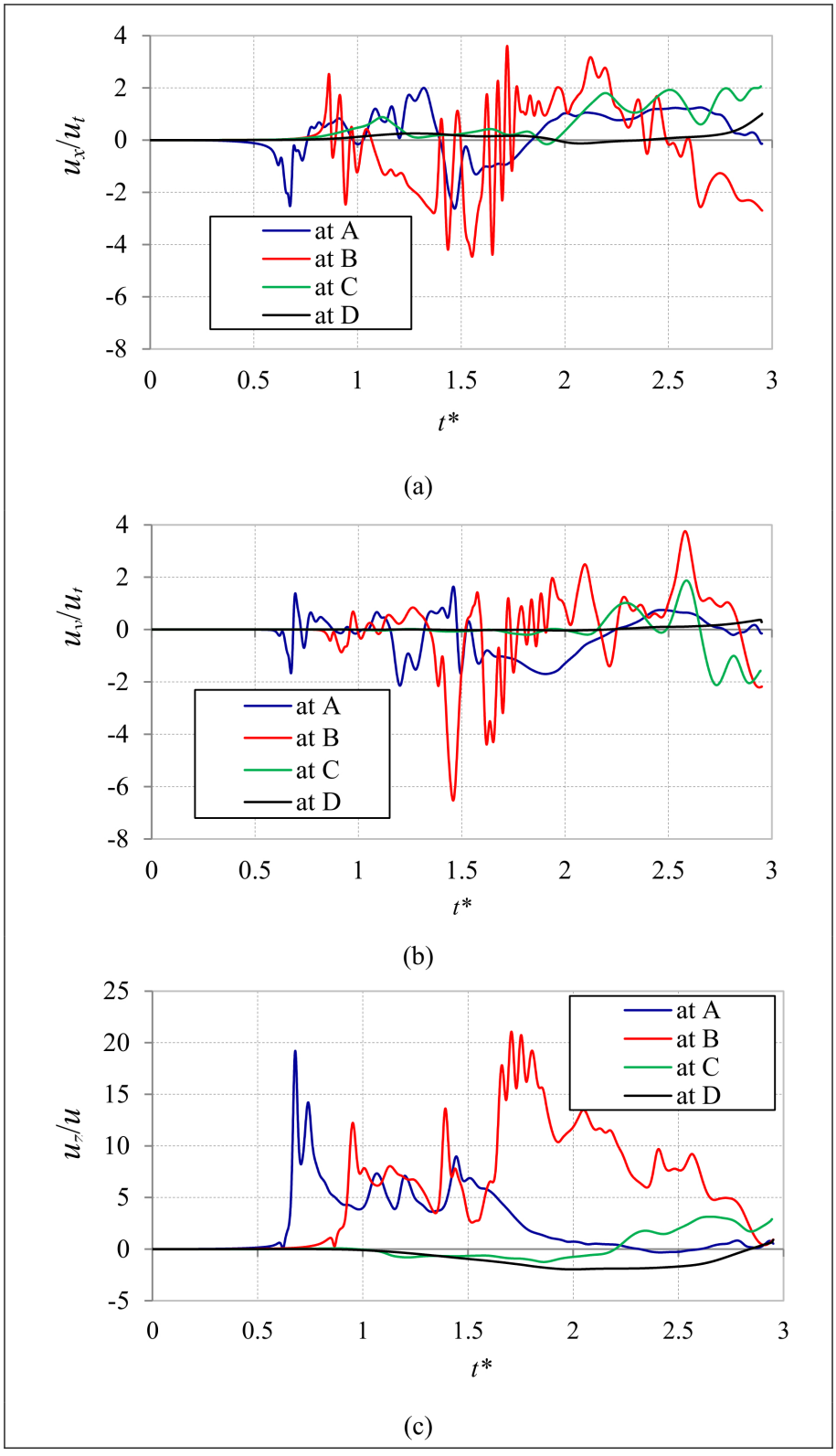

Figure 4.15: Time evolution of the liquid velocity components at four points A = $(-D, 0, 4D)$, B = $(D, 0, 6D)$, C = $(2D, 0, 7D)$, and D = $(3D, 0, 8D)$

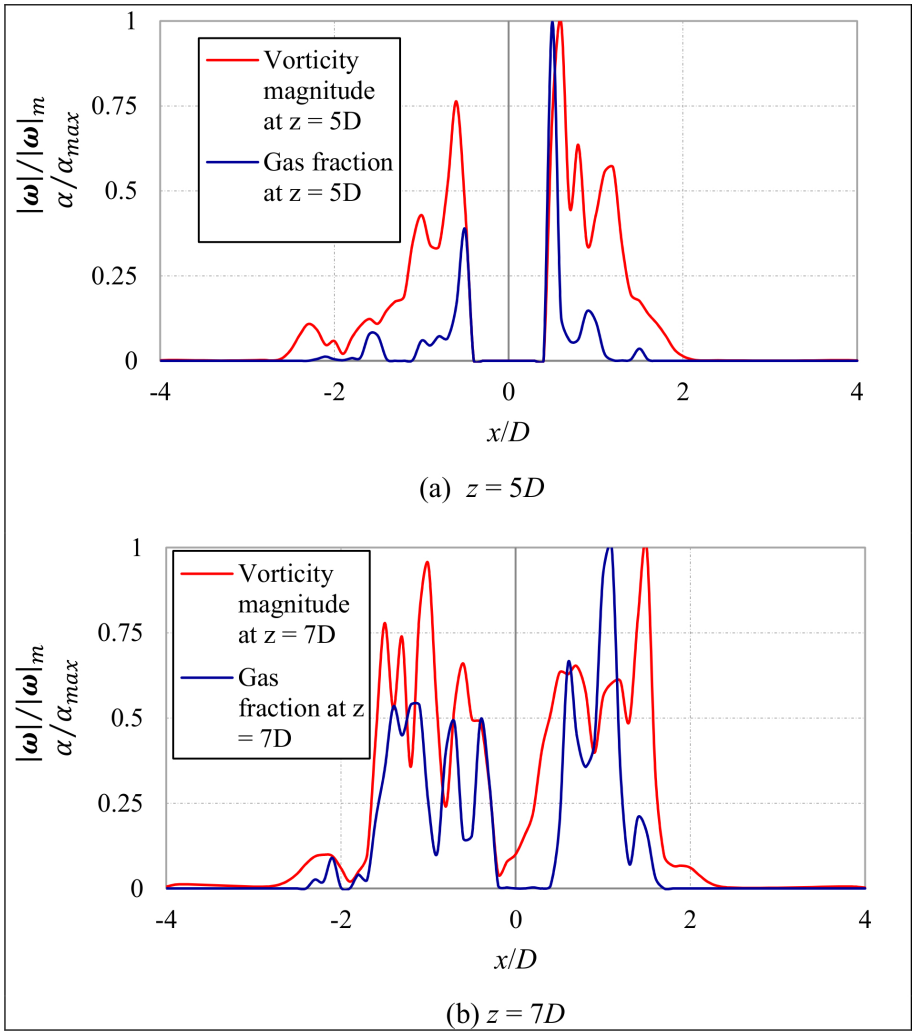

Figure 4.16: Gas volume fraction and vorticity magnitude along a horizontal line passing through the cylinder center at $t^* = 1.395$ at heights $z = 5D$ and $7D$

4.4 Conclusions

A semi-L–L method was developed for the simulation of the bubbly flows around a cylinder, which was verified through a series of simulations, including the evolution of a vortex ring moving through the boundary of the domain, the collision of a vortex ring with a cylinder, and free bubbly flows around a circular cylinder. The simulation results agreed well with prior modeled and experimental results. The characteristics of the bubbly flow around a circular cylinder can thus be summarized as follows:

(i) The bubbles rised and induced liquid flow plane shear layers. These shear layers reached the cylinder surface, moved around, and the separated from both sides of the cylinder. These shear layers entrained the bubbles to move around and also separated from both sides of the cylinder to form bubble layers. When the flow fully developed, the bubble distribution was quasi-stable upstream, whereas unstable downstream. The bubbles were entrained into induced vortices and dispersed over a large region of

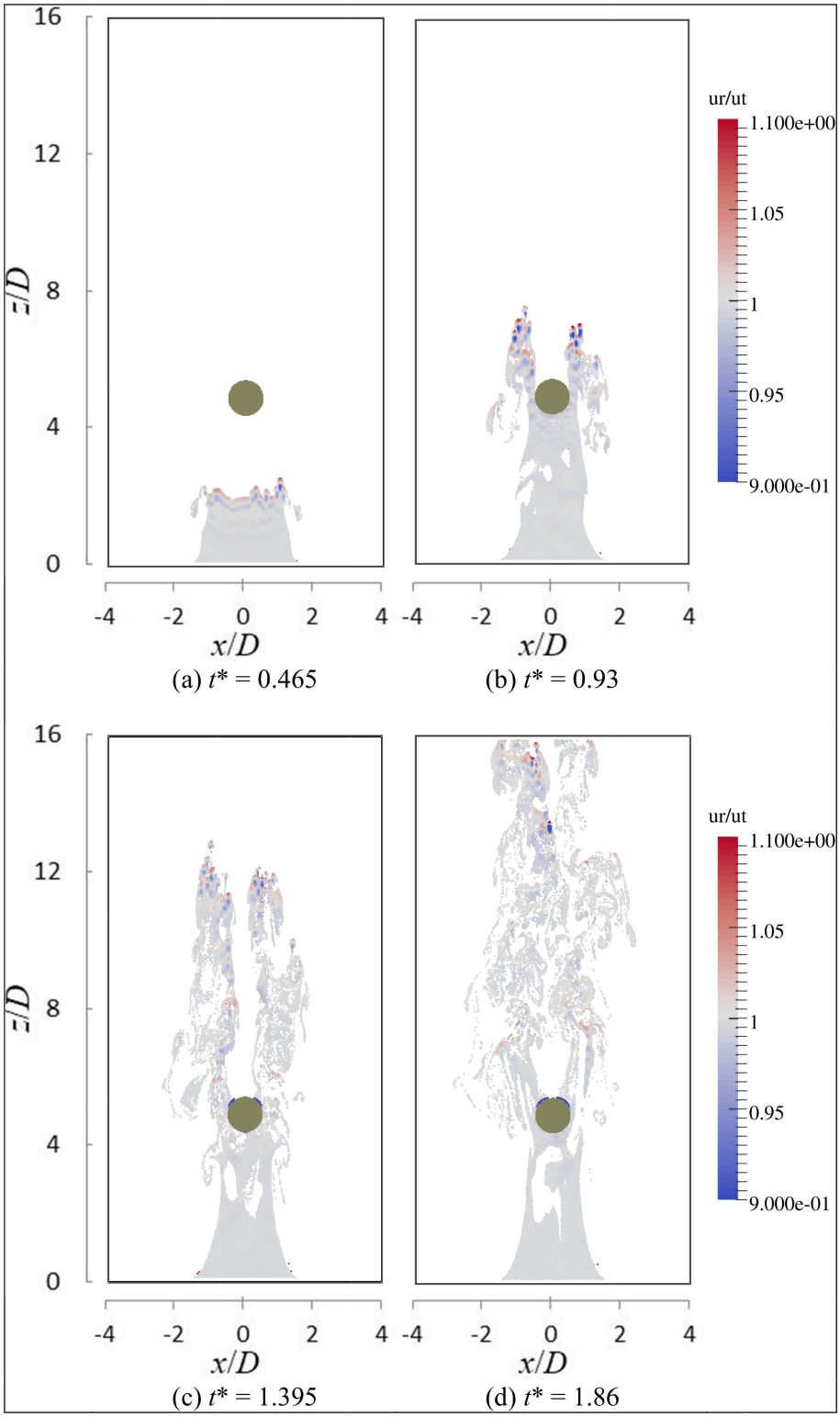

Figure 4.17: Time evolution of slip velocity of bubbles on the x-z plane

downstream.

(ii) The three-dimensional vortex structure of the flow of various scales developed in the early stage, due to the interaction of plane shear layers induced by bubbles. Once the

flow fully developed, this structure developed significantly downstream, but degenerated into a two-dimensional structure and became quasi-stable upstream.

(iii) The bubble distribution pattern was similar to that of the vortex structure. At an instant time point, the number and location of peaks of the gas volume fraction were the same and near those of the vorticity magnitude, respectively.

(iv) The proposed method is well applicable to the simulation of gas–liquid bubbly flows around an obstacle and has abilities to analyze the vortex structure of the flow and supply physical details of bubble dynamics.

Chapter 5

Conclusions

This chapter concludes the research work and proposes some future work that can be developed from this dissertation.

5.1 Conclusions of the study

The semi-Lagrangian–Lagrangian (semi-L–L) composed of a vortex-in-cell method for the liquid phase and a Lagrangian description of the gas phase was successfully developed to simulate the gas-liquid two-phase flows. The highlights of this study are given as follows:

In chapter 2, it was shown that the semi-L–L approach has superior abilities to analysis the vortex structure of the flow and supply physical details of bubble dynamics. The vortex structure of vortex rings of various scales was formed and then deformed with the time evolution of the annular bubble plume. The plume was stable in the early stage of the flow, and then it reached the transition stage with the meandering motion before the full development of three-dimensional vortical flow. The liquid velocity field was shown to depend upon in each stage. Moreover, the characteristics of bubble dynamics such as the location, rise and slip velocities of the bubble in each stage were clarified.

In chapter 3, a vortex ring can transport the bubbles surrounding it over a distance significantly depending on the correlative initial position between the bubbles and the core center. The motion of some bubbles was nearly periodic and gradually extinguished with time. These bubble trajectories were similar to two-dimensional-helix shapes. The vortex was fragmented into multiple regions with high values of Q, the second invariant of velocity gradient tensor, settling at these regional centers. The entrained bubbles excited a growth rate of the vortex rings azimuthal instability with a formation of the second- and third-harmonic oscillations of modes of 16 and 24, respectively.

In chapter 4, a semi-L–L approach continued to be developed to simulate the bubbly flow around a circular cylinder. The bubbles were shown to move around and separate from both sides of the cylinder, due to entrainment by the liquid shear layers. Once the bubbly flow fully developed, the bubbles distributed into groups and were dispersed

downstream of the cylinder. A three-dimensional vortex structure of various scales was also shown to form downstream, whereas a quasi-stable two-dimensional vortex structure was observed upstream. Overall, the proposed method captured the characteristics of a bubbly flow around a cylinder well.

5.2 Remarks for future work

Based on the current study, some future work can be developed to improve the approach as

First, the assumptions in this study were given in section 2.2.1 in which the bubble diameter is small, and the mass and momentum of the gas phase are very small and negligible, respectively, compared to those of the liquid phase. This leaded to a hypothesis mass and momentum equations, Eqs. (2.1) and (2.2), for the liquid phase. In the case of larger bubble and high bubble flow rate, the effects of turbulence induced by the bubbles (bubble-induced turbulence), full effects of the gas volume fraction on the momentum equation of the liquid phase, the effects of momentum source point induced by the bubbles on the liquid phase (the momentum exchange between two phases) should be considered. In addition, in the Lagrangian description of the gas phase, the turbulent dispersion force, Bassett force, and viscous force can be applied in the current model.

Second, the flow quantities were discretized on the regular grid. This leaded to high computational cost when the number of grid increased. The multi-grid resolution technique can be applied to the model for gas–liquid two-phase flow. When using this technique, in the bubble plume case, the high and low grid resolutions can be set to calculate the flow quantities in the inner and outer bubble plume, respectively.

Last, in this study, no turbulence model was employed for the liquid phase. The turbulence model can be applied to the approach to simulate the turbulent bubbly flows.

Appendix A

Numerical simulation of flow around two tandem cylinders by vortex-in-cell method combined with immersed boundary method

A.1 Introduction

Flows around two cylinders in tandem arrangement have attracted the interest of many researchers. This is because the flows are frequently observed in various engineering devices such as heat exchangers, chemical reactors and oil pipelines. The interactions between the wakes of each cylinder, the vortex shedding and the fluid forces acting on the cylinders have been investigated to develop the high-efficiency devices.

A number of experimental researches on incompressible flows around two tandem cylinders have been conducted for the wide range of the Reynolds number (Thomas and Kraus, 1964; Kostic and Oka, 1972; Tanida et al., 1973; Zdravkovich, 1987; Sumner et al., 1999). They clarified that the reattachment of shear layers separated from the front cylinder to the rear one occurs when the distance between the cylinders is small and the vortical flow downstream of the rear cylinder is similar to that downstream of a single cylinder. They also revealed that the vortex formation behind the rear cylinder is affected by the vortical flow formed near the front cylinder when the distance between the cylinders is larger than a threshold value. Numerical simulations have also been performed (Jester and Kallinderis, 2003; Meneghini and Saltara, 2001; Kitagawa and Ohta, 2008; Vakil and Green, 2013; Mittal et al., 1997). They explored the effects of the Reynolds number and distance between the cylinders on the flow and fluid force acting on the cylinders. The simulations were chiefly based on finite element methods and finite volume methods.

Vortex-in-cell (VIC) method is one of the vortex methods to simulate incompressible flows (Christiansen, 1973). It discretizes the vorticity field into vortex elements and computes the time evolution of the flow by tracing the convection of each vortex element using the Lagrangian approach. The Lagrangian calculation markedly reduces numerical-dissipation errors and also improves numerical stability. Thus, the VIC method

is eminently suitable for direct numerical simulation (DNS) of free turbulent flows (Cottet and Poncet, 2003; Winckelmens et al., 2005; Cocle et al., 2008; Chatelain et al., 2008). Uchiyama et al. (2014b) applied a VIC method to the DNS of a turbulent channel flow. The DNS highlighted the successful capture of organized flow structures, such as streaks and streamwise vortices in the near wall region, demonstrating that the VIC method is applicable to DNS of wall turbulent flows. The DNS of a rotating channel flow (Uchiyama et al., 2014a) and that of a jet issued from a rectangular nozzle (Uchiyama et al., 2013) were also performed, and the vortical structures were successfully simulated. Uchiyama (2013) also proposed a VIC method for incompressible gas flows laden with small solid particles. The method was favorably used to investigate the interactions between a vortex pair and solid particles near a horizontal wall in the air (Uchiyama and Shimada, 2014).

In this study, the VIC method is applied to the simulation of incompressible flows around two cylinders in tandem arrangement. In the simulation, the solid wall of the cylinder should be considered or the non-slip condition on the wall should be satisfied. Therefore, this study employs an immersed boundary (IB) method proposed by Peskin (1972). Such simulations by using the VIC and IB methods have been presented, and various flows were successfully analyzed (Rossinelli et al., 2010; Mimeau et al., 2015; Gazzola et al., 2011; Rasmussen et al., 2011). But the applicability of the VIC and IB methods to simulate the flows around two tandem cylinders has not been examined. The present simulation of the flows around two tandem cylinders highlights that the methods can successfully simulate the behavior of the shear layers separated from the cylinders, the vortex shedding and the fluid forces acting on the cylinders. It also demonstrates that the methods can analyze the effects of the Reynolds number and distance between the cylinders on the flow characteristics.

A.2 Numerical method

A.2.1 Vorticity equation and orthogonal decomposition of velocity

The conservation equations for mass and momentum of viscous incompressible flows are written as follows

$$\nabla \cdot \boldsymbol{u} = 0 \tag{A.1}$$

$$\frac{\partial \boldsymbol{\omega}}{\partial t} + \nabla \cdot (\boldsymbol{u}\boldsymbol{\omega}) = \nabla \cdot (\boldsymbol{\omega}\boldsymbol{u}) + \nu \nabla^2 \boldsymbol{\omega} \tag{A.2}$$

where t is the time, $\boldsymbol{u}$ is the velocity, and ν is the kinematic viscosity. The vorticity $\boldsymbol{\omega}$ is defined as:

$$\boldsymbol{\omega} = \nabla \times \boldsymbol{u} \tag{A.3}$$

The second term on the left-hand side of Eq. (A.2) is convection, and the first and second terms on the right-hand side are vortex stretching and diffusion, respectively. In two-dimensional simulation, the stretching term disappears out of the governing equation.

The convective form of Eq. (A.2) and its term are explained in Appendix D.

According to the Helmholtz theorem, the velocity $\boldsymbol{u}$ is represented as the summation of the curl of a vector potential $\boldsymbol{\omega}$ and the gradient of a scalar potential ϕ:

$$\boldsymbol{u} = \nabla \times \boldsymbol{\psi} + \nabla\phi \tag{A.4}$$

The velocity calculated from Eq. (A.4) remains unaltered even when any gradient of scalar-potential function is added to $\boldsymbol{\omega}$. To remove this arbitrariness, a solenoidal condition is imposed on $\boldsymbol{\psi}$:

$$\nabla \cdot \boldsymbol{\psi} = 0 \tag{A.5}$$

Taking the curl of Eq. (A.4) and substituting Eq. (A.5) into the resultant equation, the vector Poisson equation for $\boldsymbol{\psi}$) is derived:

$$\nabla^2\boldsymbol{\psi} = -\boldsymbol{\omega} \tag{A.6}$$

When substituting Eq. (A.4) into the continuity equation, Eq. (A.1), and rewriting the resultant equation by using the relation $\nabla\cdot(\nabla\times\boldsymbol{\psi})$, the Laplace equation for ϕ is obtained:

$$\nabla^2\phi = 0 \tag{A.7}$$

A.2.2 Vortex-in-cell method

The VIC method discretizes the vorticity field $\boldsymbol{\omega}$ into vortex particles p carrying the vorticity $\boldsymbol{\omega}_p$. Vortex particles move at their velocity $\boldsymbol{u}(\boldsymbol{x}_p)$ given by the value of the velocity field at their location, $\boldsymbol{x}_p$. The vorticity–velocity equation, Eq. (A.2), is rewritten based on the Lagrangian description of vortex particles as follows

$$\frac{d\boldsymbol{x}_p}{dt} = \boldsymbol{u}(\boldsymbol{x}_p) \tag{A.8}$$

$$\frac{d\boldsymbol{\omega}_p}{dt} = \nabla \cdot \Big(\boldsymbol{\omega}(\boldsymbol{x}_p)\boldsymbol{u}(\boldsymbol{x}_p)\Big) + \nu\nabla^2\boldsymbol{\omega}(\boldsymbol{x}_p) \tag{A.9}$$

At the beginning, the vortex particles, carrying the vorticity, lay on the regular Eulerian grid nodes. The vortex-particle velocity is obtained from Eq. (A.4), while the vector and scalar potentials, $\boldsymbol{\psi}$ and ϕ , are calculated through Eqs. (A.6) and (A.7), respectively. The vorticity carried by vortex particles is computed from Eq. (A.9). Subsequently, the vortex particles carrying their calculated vorticity move to the Lagrangian location by the convection equation, Eq. (A.8). Finally, the vortex particles with the vorticity $\boldsymbol{\omega}_p$ at their Lagrangian location $\boldsymbol{x}_p$ are redistributed onto the grid location $\boldsymbol{x}_g = (x_g, y_g)$ as follows

$$\boldsymbol{\omega}(\boldsymbol{x}_q) = \sum_{p}^{N_p} \boldsymbol{\omega}_p W\Big(\frac{x_q - x_p}{\Delta x}\Big) W\Big(\frac{y_q - y_p}{\Delta y}\Big) \tag{A.10}$$

where N_p is the number of vortex particles, and Δx and Δy are the grid widths. The W is a third-order accurate kernel-interpolation function which is proposed by Monaghan

(1985) for one-dimensional SPH methods, and by Cottet and Koumoutsakos (2000) for two- and three-dimensional vortex methods, and it is expressed as

$$W(x) = \begin{cases} 1 - \frac{5}{2}|x|^2 + \frac{3}{2}|x|^3 & \text{if } |x| \leq 1 \\ \frac{1}{2}(2 - |x|)^2(1 - |x|) & \text{if } 1 < |x| \leq 2 \\ 0 & \text{if } |x| > 2 \end{cases} \tag{A.11}$$

Herein, the order of accuracy indicates the number of the flow momentum conserved when redistributing vortex elements from Lagrangian to Eulerian locations. With the use of the above kernel-interpolation function, the first three vorticity momentums of the flow, $(\Omega_i, i = 0, 1, 2)$, are conserved as

$$\Omega_0 = \iiint_V \boldsymbol{\omega} dV \tag{A.12}$$

$$\Omega_1 = \frac{1}{2} \iiint_V \boldsymbol{x} \times \boldsymbol{\omega} dV \tag{A.13}$$

$$\Omega_2 = \frac{1}{3} \iiint_V \boldsymbol{x} \times (\boldsymbol{x} \times \boldsymbol{\omega}) dV \tag{A.14}$$

A.2.3 Immersed-boundary method

The IB method was proposed by Peskin (1972) to simulate the flow around a solid body. This study uses the IB method with the VIC method to satisfy the no-slip condition of the flow on the body surface. When using the Brinkman penalization method (Cottet and Poncet, 2003), one type of IB method, the vorticity equation (Eq. (A.2)) is rewritten as

$$\frac{\partial \boldsymbol{\omega}}{\partial t} + \nabla \cdot (\boldsymbol{\omega u}) = \nabla \cdot (\boldsymbol{u\omega}) + \nu \nabla^2 \boldsymbol{\omega} + \nabla \times \left[\lambda \chi_s (\boldsymbol{u}_s - \boldsymbol{u}) \right] \tag{A.15}$$

where $\boldsymbol{u}_s$ is the solid-body velocity and λ is the penalization parameter. χ_s classifies the solid and fluid regions, and it is given as

$$\chi_s(x) = \begin{cases} 1 & \text{if } x \in S \\ 0 & \text{if } x \in F \end{cases} \tag{A.16}$$

where S and F denote the solid and fluid regions, respectively, as shown in Fig. A.1. The χ_s is varied smoothly from 0 to 1 near fluid–solid interface using the following Heaviside function:

$$\chi_s(d) = \begin{cases} 0 & \text{if } d < -\varepsilon \\ \frac{1}{2}\left[1 + \frac{1}{\varepsilon} + \frac{1}{\pi} \sin\left(\pi \frac{d}{\varepsilon}\right)\right] & \text{if } |d| \leq \varepsilon \\ 1 & \text{if } d > \varepsilon \end{cases} \tag{A.17}$$

where ε is set as $2\sqrt{2}\Delta x$ and d is a sign-distance from fluid–solid interface to the grid node. It can image that the fluid is a continuous phase through solid body because of a

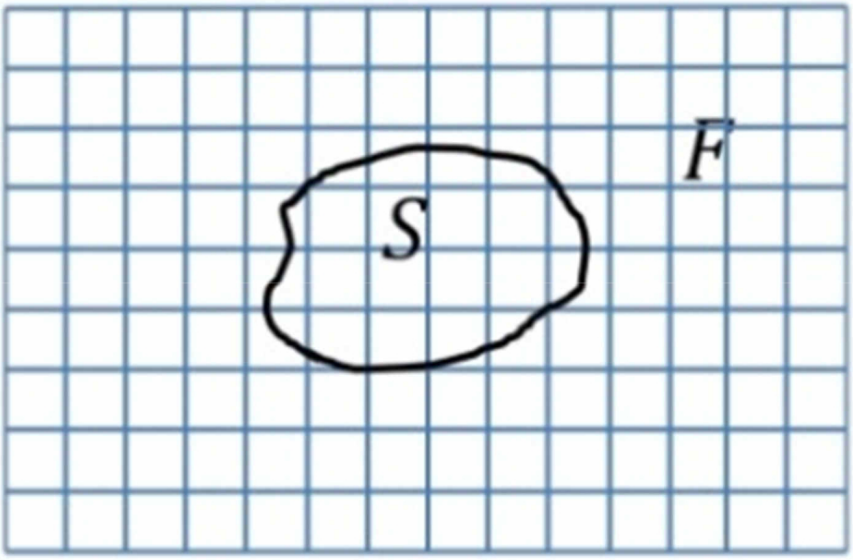

Figure A.1: Configuration of solid and fluid regions S and F, respectively

continuous change of the liquid velocity through fluid–solid interface. By choosing $\lambda = \frac{1}{\Delta t}$ and using first-order finite-difference schemes, the velocity field is obtained as

$$\boldsymbol{u}_\lambda = (1 - \chi_s)\boldsymbol{u} + \chi_s \boldsymbol{u}_s \tag{A.18}$$

The penalization vorticity is calculated from the penalization velocity $\boldsymbol{u}_\lambda$ as follows

$$\boldsymbol{\omega}_\lambda = \boldsymbol{\omega} + \nabla \times (\boldsymbol{u}_\lambda - \boldsymbol{u}) \tag{A.19}$$

A.2.4 Numerical procedure

Given a flow at time t, the flow at $t + \Delta t$ is calculated by the following procedure:

(1) calculate the vorticity $\boldsymbol{\omega}_p$ from Eq. (A.9) to account for vortex diffusion;

(2) calculate the Lagrangian location of vortex particles $\boldsymbol{x}_p$ from Eq. (A.8);

(3) calculate $\boldsymbol{\omega}$ from Eq. (A.10) to redistribute vortex particles onto the grid;

(4) calculate the vector potential $\boldsymbol{\psi}$ from Eq. (A.6);

(5) calculate the scalar potential ϕ from Eq. (A.7);

(6) calculate the velocity field $\boldsymbol{u}$ from Eq. (A.4);

(7) calculate the penalization velocity $\boldsymbol{u}_\lambda$ from Eq. (A.18) to satisfy the no-slip condition of the flow at the fluid–solid interface;

(8) calculate the penalization vorticity $\boldsymbol{\omega}_\lambda$ from Eq. (A.19).

A.3 Results and discussions

First, the VIC method combined with the IB method is applied to the simulation of flows around a single circular cylinder so as to examine the applicability. The Reynolds number, $Re = U_0 D/\nu$, ranges from 40 to 9500, where U_0 is the velocity upstream of the cylinder

and D is the cylinder diameter. The cylinder is located at the coordinate origin as shown in Fig. A.2. The drag and lift coefficients of the cylinder are defined $Cd = 2F_x/(\rho U_0^2 D)$, $Cl = 2F_y/(\rho U_0^2 D)$, where ρ is the fluid density and the fluid forces F_x and F_y are calculated according to the formula proposed by Noca et al. (1999) and deployed by Mimeau et al. (2015).

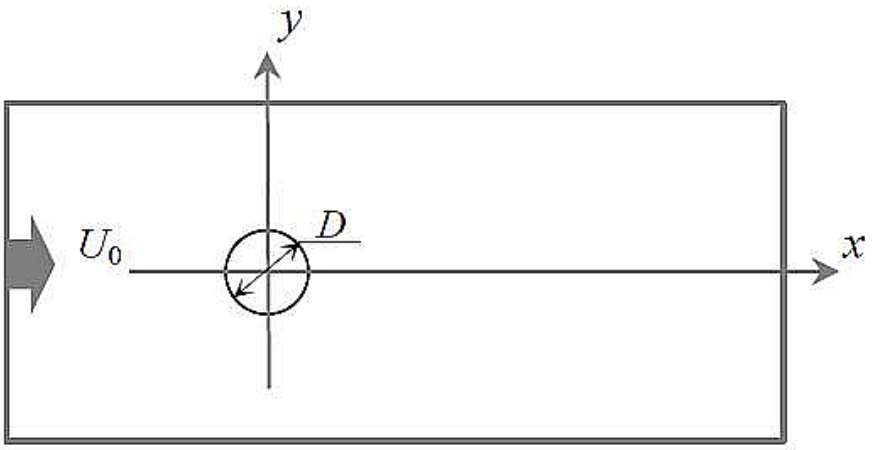

Figure A.2: Configuration of solid and fluid regions S and F, respectively

Flows at $Re = 100$ and 200 are simulated by using a computational domain $(-7D, 68D) \times (-7.5D, 7.5D)$. The number of computational grids is 7500×1500, and therefore the grid width in the x and y directions is $0.01D$. The time increment Δt^* is set at $\Delta t U_0/D = 0.0025$. Vortex shedding from the cylinder is successfully simulated at $Re = 100$ and 200. Figure A.3 shows the vorticity distribution of the fully-developed flow at $Re = 200$.

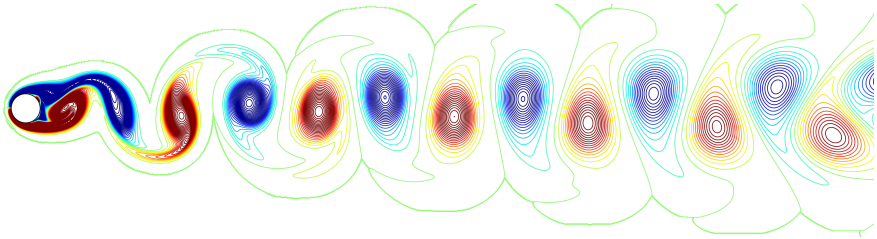

Figure A.3: Instantaneous vorticity distribution around a single cylinder at $Re = 200$

The time-averaged drag coefficient $\bar{C}d$ and the Strouhal number St at $Re = 100$ and 200 are listed in Table A.1. The present results are favorably compared to the existing numerical simulations (Meneghini and Saltara, 2001; Mimeau et al., 2015; Braza et al., 1986).

To validate the present simulation method at other Reynolds numbers, the simulations of the flow around a single circular cylinder at $Re = 40, 550, 1000, 3000$ and 9500 are performed. The simulation conditions are listed in Table A.2. The time variation of the

Table A.1: Time-averaged drag coefficient and Strouhal number of single cylinder at $Re = 100, 200$

Authors	$Re = 100$		$Re = 200$	
	$\bar{C}_d$	St	$\bar{C}_d$	St
Present authors	1.35	0.162	1.40	0.191
Meneghini and Saltara (2001)	1.37	0.165	1.30	0.196
Mimeau et al. (2015)	1.40	0.165	1.44	0.200
Braza et al. (1986)	1.36	0.160	1.40	0.190

Table A.2: Simulation parameters of flow around a single cylinder at $Re = 40, 550, 1000, 3000, 9500$

Case	Computational Domain	Number of grid nodes	$U_0\Delta t/D$
$Re = 40$	(-5D, 15D)×(-5D, 5D)	1000×500	0.001
$Re = 550$	(-4D, 12D)×(-4D, 4D)	3200×1600	0.001
$Re = 1000$	(-4D, 12D)×(-4D, 4D)	3200×1600	0.001
$Re = 3000$	(-4D, 12D)×(-4D, 4D)	4800×2400	0.0005
$Re = 9500$	(-4D, 12D)×(-4D, 4D)	9600×6400	0.00025

drag coefficient Cd in the starting period are shown in Fig. A.4. They agree well with the simulation results of Koumoutsakos and Leonard (1995). The time evolution of the vorticity distribution around the cylinder at $Re = 9500$ is shown by the plots in the right column of Fig. A.5. The vorticity near the cylinder is clearly resolved, and it agrees well with the simulation results of Rasmussen et al. (2011) shown by the plots in the lower column of Fig. A.5. Figure A.6 shows other results to detail the evolution of vorticity around the cylinder at this Reynolds number.

In order to observe a long wake behind the rear cylinder and to obtain the time-averaged drag and lift coefficients of the cylinders at $Re = 1000$, a simulation with a computational domain $(-4D, 26D) \times (-5D, 5D)$ is also conducted. The number of grids is 6000 × 2000, and the simulation is performed in a time period $U_0t/(D/2) \leq 400$. The domain and the time period are larger and longer, respectively, than those of the simulation obtaining the time variation of Cd shown in Fig. A.4. Figure A.7 shows the vorticity distribution at $U_0t/(D/2) = 400$. Vortices are periodically shed from the cylinder, producing the Karman vortices downstream of the cylinder. Such periodical shed is reconfirmed from the time variations of the drag and lift coefficients Cd and Cl respectively plotted in Fig. A.8. The time-averaged drag coefficient $\bar{C}d$ and the Strouhal number St are favorably compared to the existing numerical results (Mimeau et al., 2015;

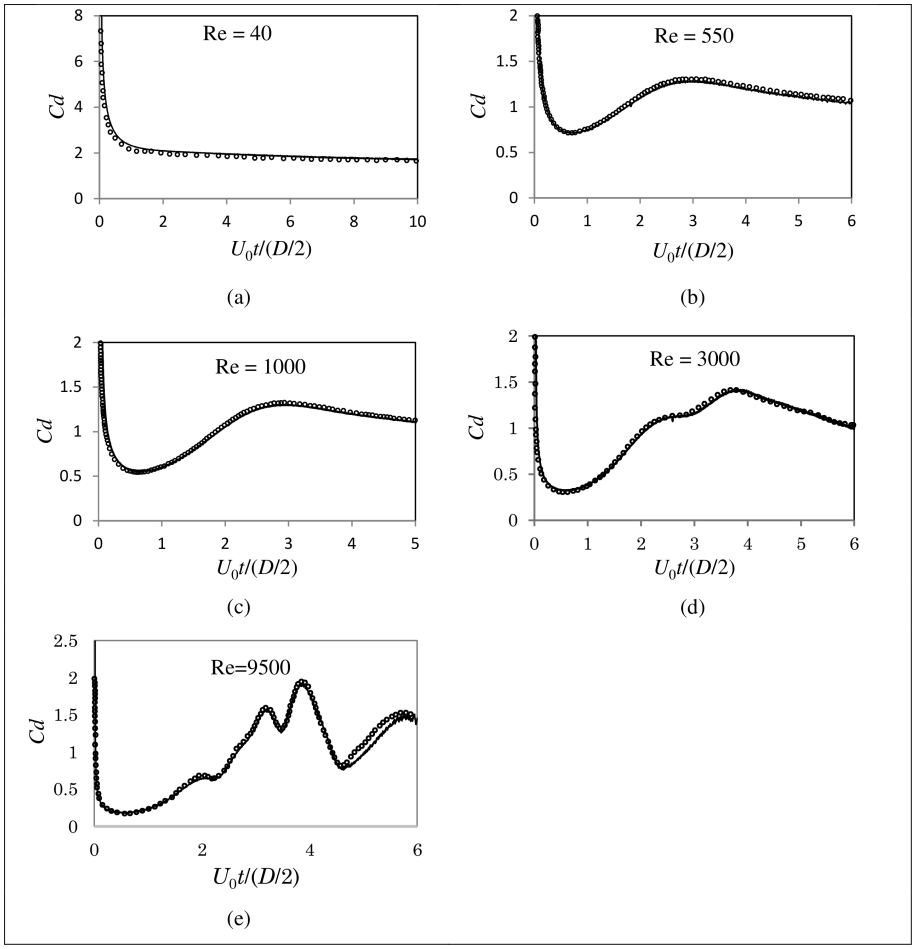

Figure A.4: Time variation of drag coefficient of single cylinder at $Re = 40, 550, 1000, 3000,$ and 9500. The dotted lines are results using vortex methods by Koumoutsakos and Leonard (1995), while the solid lines are present results

Ape et al., 2009; Mittal and Kumar, 2001) as shown in Table A.3.

A.3.1 Flow around two tandem cylinders at $Re = 200$

Flows around two cylinders in tandem arrangement are simulated at $Re = 200$, where Re is defined by the diameter of each cylinder D and the uniform velocity U_0 upstream of the front cylinder. The distance between the front and rear cylinders, L, ranges from $1.5D$ to $8D$. The front cylinder is located at $(x, y) = (0, 0)$ in the computational domain shown in Fig. A.2. The computational domain $(-7D, 68D) \times (-7.5D, 7.5D)$ is discretized into 7500×1500 grid nodes.

Figure A.9 shows the instantaneous vorticity distribution of the fully-developed flow. When the distance L is small as $L = 1.5D, 2D$ and $3D$, the vortical flows downstream of the rear cylinder are almost similar to the flow downstream of a single cylinder shown in Fig. A.3. Such flows were also reported by Zdravkovich (1987). This is explained by the fact that the tandem arrangement of cylinders affects the flow as a single cylinder. In the

Table A.3: Time-averaged drag coefficient and Strouhal number of a single cylinder at $Re = 1000$

Authors	$\bar{C}_d$	St
Present authors	1.56	0.236
Mimeau et al. (2015)	1.51	0.245
Ape et al. (2009)	1.50	0.238
Mittal and Kumar (2001)	1.48	0.250

case of $L = 4D$, the shear layers separated from the front cylinder roll up between the cylinders and change into vortices. Such vortices collide with the rear cylinder. When L increases to $6D$ and $8D$, the vortices shed from each cylinder interact. The vortical flows downstream of the rear cylinder seem to be different from Karman vortices.

The drag and lift coefficients, Cd and Cl respectively, vary with the lapse of time as shown in Fig. A.10, where the subscripts 1 and 2 denote the front and rear cylinders, respectively. When the distance L is small as $1.5D, 2D$ and $3D$, the drag coefficient of the front cylinder Cd_1 remains almost unaltered and positive. The time-averaged value is about 1, which is smaller than that of a single cylinder ($\bar{C}d = 1.4$ shown in Table A.1). The drag coefficient of the rear cylinder Cd_2 is negative. The lift coefficients Cl_1 and Cl_2 fluctuate. The fluctuation amplitude of Cl_2 is larger than that of Cl_1. This is ascribed to the fact that the flow around the rear cylinder is more affected by the shear layers separated from the front cylinder. In the case that L is greater than $4D$, Cd_1 fluctuates, though the amplitude is not necessarily large. This is attributable to the periodical vortex shedding from the front cylinder, as shown in Fig. A.9. With increasing L, Cd_1 becomes larger and approaches the value of a single cylinder. Because the rear cylinder less affects the flow around the front cylinder. But Cd_2 is still small. The amplitudes of Cl_1 and Cl_2 are larger than those at $L \leq 4D$. The amplitude of Cl_2 is not constant. This is due to the fact that the vortex shedding from the rear cylinder is not periodic owing to the interactions of the vortices produced at the front and rear cylinders.

The time-averaged drag coefficients of the front and rear cylinders, $\bar{C}d_1$ and $\bar{C}d_2$, respectively, are shown in Table A.4. The Strouhal numbers of the front and rear cylinders, St_1 and St_2 respectively, are also shown. They are in good agreement with the simulation results of Meneghini and Saltara (2001) at $L \leq 4D$.

A.3.2 Flow around two tandem cylinders at $Re = 1000$

The flow around two tandem cylinders at $Re = 1000$ are simulated. The distance L between the cylinders is varied from $2D$ to $4D$. To simulate accurately the vortical flow downstream of the rear cylinder, the computation domain is set as

Table A.4: Time-averaged drag coefficients and Strouhal numbers of two tandem cylinders at $Re = 200$

Case	Coefficients	Present simulation	Meneghini and Saltara (2001)
$L = 1.5D$	$\bar{C}d_1$	1.07	1.060
	$\bar{C}d_2$	-0.20	-0.187
	$St_1 = St_2$	0.15	0.167
$L = 2.0D$	$\bar{C}d_1$	1.05	1.03
	$\bar{C}d_2$	-0.21	-0.195
	$St_1 = St_2$	0.127	0.13
$L = 3.0D$	$\bar{C}d_1$	1.0	1.0
	$\bar{C}d_2$	-0.13	-0.08
	$St_1 = St_2$	0.12	0.125
$L = 4.0D$	$\bar{C}d_1$	1.12	1.18
	$\bar{C}d_2$	0.31	0.38
	$St_1 = St_2$	0.168	0.174
$L = 6.0D$	$\bar{C}d_1$	1.30	–
	$\bar{C}d_2$	0.37	–
$L = 8.0D$	$\bar{C}d_1$	1.36	–
	$\bar{C}d_2$	0.34	–

$(-7D, 30D) \times (-7.5D, 7.5D)$ divided into 7400×3000 grid nodes.

Figure A.11 shows the vorticity distribution for the fully-developed stage of the flow. When the distance L is small as $2D$, the vortical flow downstream of the rear cylinder is similar to that downstream of a single cylinder. This is caused by the fact that the free shear layers separated from the front cylinder reattach to the rear one. Such vortical flow is also simulated at $Re = 200$ with $L \leq 3D$ as shown in Fig. A.9. When $L = 2.5D$, vortices are periodically produced between the cylinders by the roll up of the shear layers separated from the front cylinder, and they interact with the vortices shed from the rear cylinder. The vortical flow downstream of the rear cylinder is composed of such vortices. When $L = 3D$ and $4D$, the vortex sheddings from the cylinders do not synchronize, and therefore the flow downstream of the rear cylinder is not periodic.

The time variation of the drag and lift coefficients is shown in Fig. A.12. When $L = 2D$, the drag coefficient of the front cylinder Cd_1 remains almost unaltered and it is smaller than the value for a single cylinder ($\bar{Cd} = 1.56$ shown in Table A.3). However, the drag coefficient of the rear cylinder Cd_2 slightly fluctuates and it is negative. The time-averaged values of Cd_1 and Cd_2 are 0.94 and -0.2 respectively. The amplitudes of the lift coefficients Cl_1 and Cl_2 are smaller than that of the single cylinder shown in Fig A.8. In the case of $L = 2.5D, Cd_1$ fluctuates. Though the time-averaged value is larger than that at $L = 2D$, it is still lower than that for the single cylinder. The amplitude of Cl_1 is also larger than that at $L = 2D$. For the rear cylinder, the drag coefficient Cd_2 varies around zero, and the amplitude of Cl_2 is larger than that for the single cylinder. The variations of the drag and lift coefficients are nearly periodical. When $L = 3D$ and $4D$, the time-averaged value of Cd_1 is slightly lower than that for the single cylinder. But the lift coefficient Cl_1 is almost parallel with that for the single cylinder. It should be noted that the amplitude of Cl_2 is not constant. This is owing to the passage of the vortices shed from the front cylinder, as found from Fig. A.9. The lift coefficients Cl_2 fluctuates markedly owing to the vortex shedding from the rear cylinder shown in Fig. A.11.

A.3.3 Flow around two tandem cylinders at $Re = 9500$

The flow at $Re = 9500$ with $L = 1.5D$ and $2D$ are simulated by a computational domain $(-4D, 8D) \times (-4D, 4D)$ divided into 9600×6400 grid nodes. The simulation is performed in a period of $U_0 t/(D/2) \leq 35$.

Figure A.13 shows the time evolution of the vorticity distribution in the case of $L = 1.5D$. The shear layers separated from the front cylinder roll up between the two cylinders and flow down with colliding at the rear cylinder. When $U_0 t/(D/2) \leq 10$, the flow is symmetric with respect to a centerline passing through the cylinder centers. Such the symmetry collapses greatly at $U_0 t/(D/2) = 15$. The vortex shedding occurs behind

both the cylinders during $U_0t/(D/2) \geq 25$.

The time evolution of the vorticity distribution in the case of $L = 2D$ is shown in Fig. A.14. The flow characteristics are almost parallel with those in the case of $L = 1.5D$ shown in Fig. A.13.

The time variations of the drag and lift coefficients are shown in Fig. A.15. The drag coefficient of the front cylinder Cd_1 is always positive irrespective of the L value. It begins to fluctuate markedly at $U_0t/D = 25$.

This is owing to the vortex shedding from both cylinders as depicted in Figs. A.13 and A.14. The drag coefficient of the rear cylinder Cd_2 is positive at the beginning of the flow. But it is negative when the rear cylinder is immersed in the symmetrically vortical flow. After the symmetry collapses, Cd_2 fluctuates markedly. The lift coefficients Cl_1 and Cl_2 fluctuate slightly when the flow remains symmetric. But they fluctuate markedly when the vortex shedding occurs.

A.4 Conclusions

The numerical simulation of incompressible flows around two circular cylinders in tandem arrangement is performed by the VIC method combined with an IB method. The vorticity fields are discretized into vortex particles by the VIC method, and the Brinkman penalization method is employed to guarantee the no-slip condition of the fluid flow implemented at the fluid-solid interface. The Reynolds number Re based on the cylinder diameter D and the velocity upstream of the front cylinder ranges from 200 to 9500, and the distance L between the cylinders is varied from $1.5D$ to $8D$.

The simulation shows that the flow characteristics, such as the behavior of the shear layers separated from the cylinders, the vortex shedding and the fluid forces acting on the cylinders, are favorably compared to the existing simulation results and experimental measurements. It also indicates that the effects of Re and L on the flow characteristics are successfully analyzed. These demonstrate the applicability of the VIC and IB methods for the simulation of incompressible flows around two tandem cylinders.

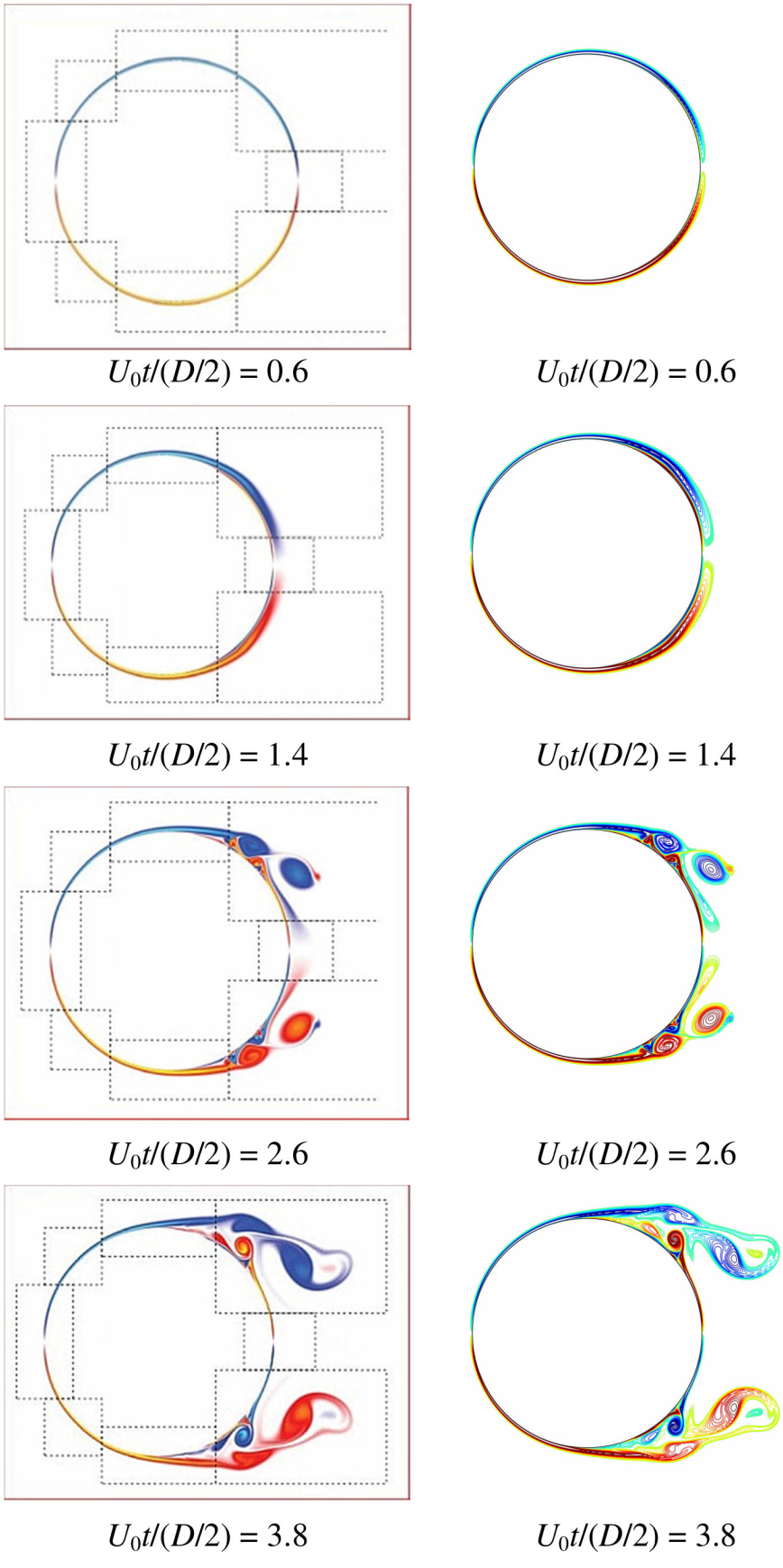

Figure A.5: Time evolution of vorticity field near a single cylinder at $Re = 9500$. The plots in the right column represent the present simulation. The plots in the left column represent the results by Rasmussen et al. (2011)

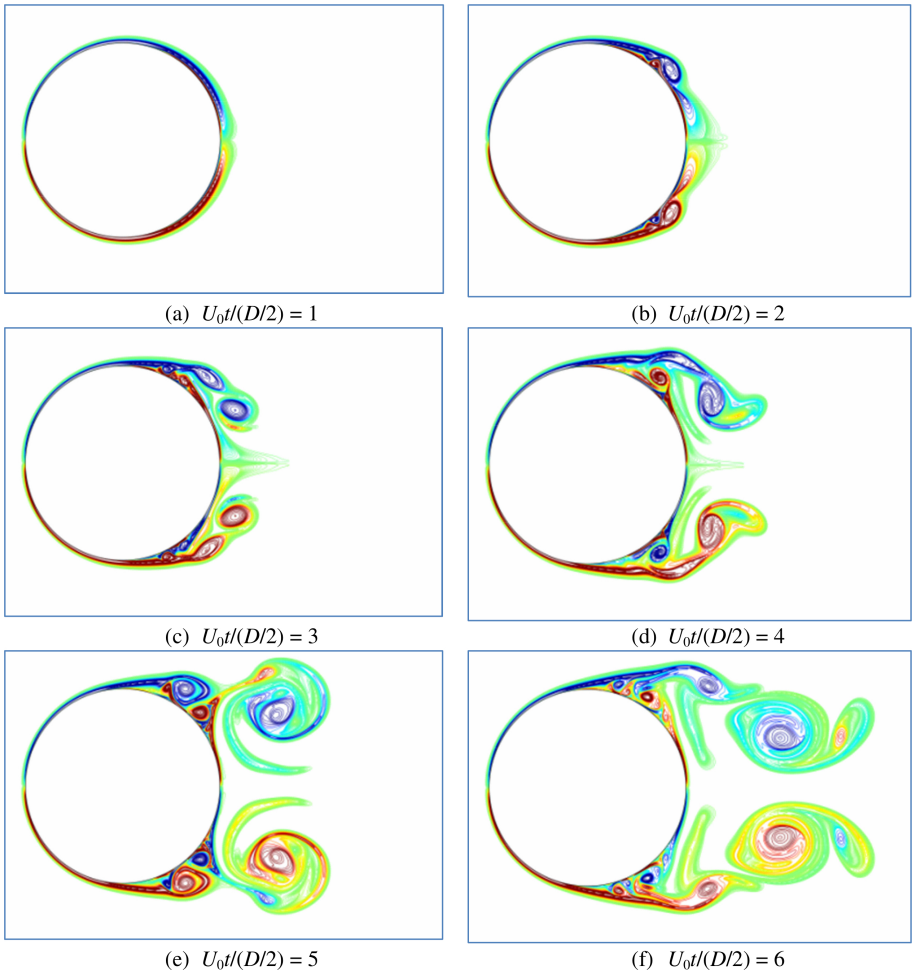

Figure A.6: Time evolution of vorticity field near a single cylinder at $Re = 9500$.

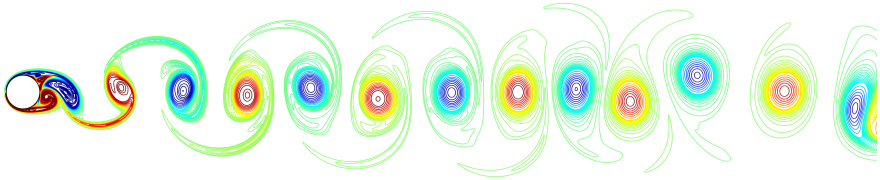

Figure A.7: Instantaneous vorticity distribution of the flow around a single cylinder at $Re = 1000$

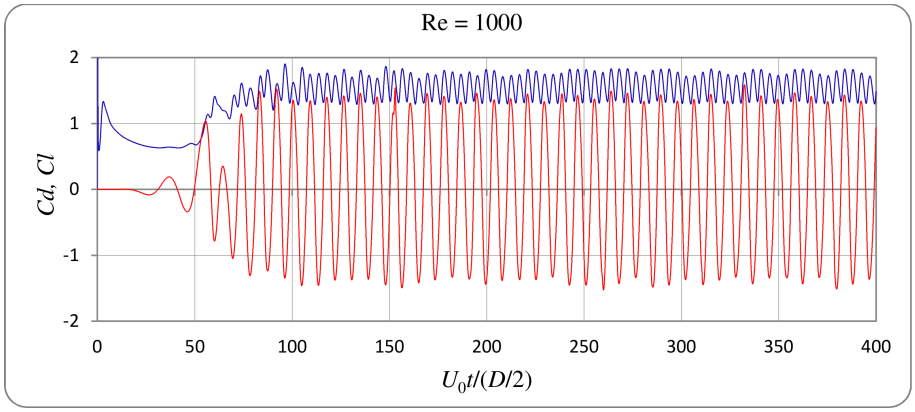

Figure A.8: Time variation of drag and lift coefficients of a single cylinder at $Re = 1000$

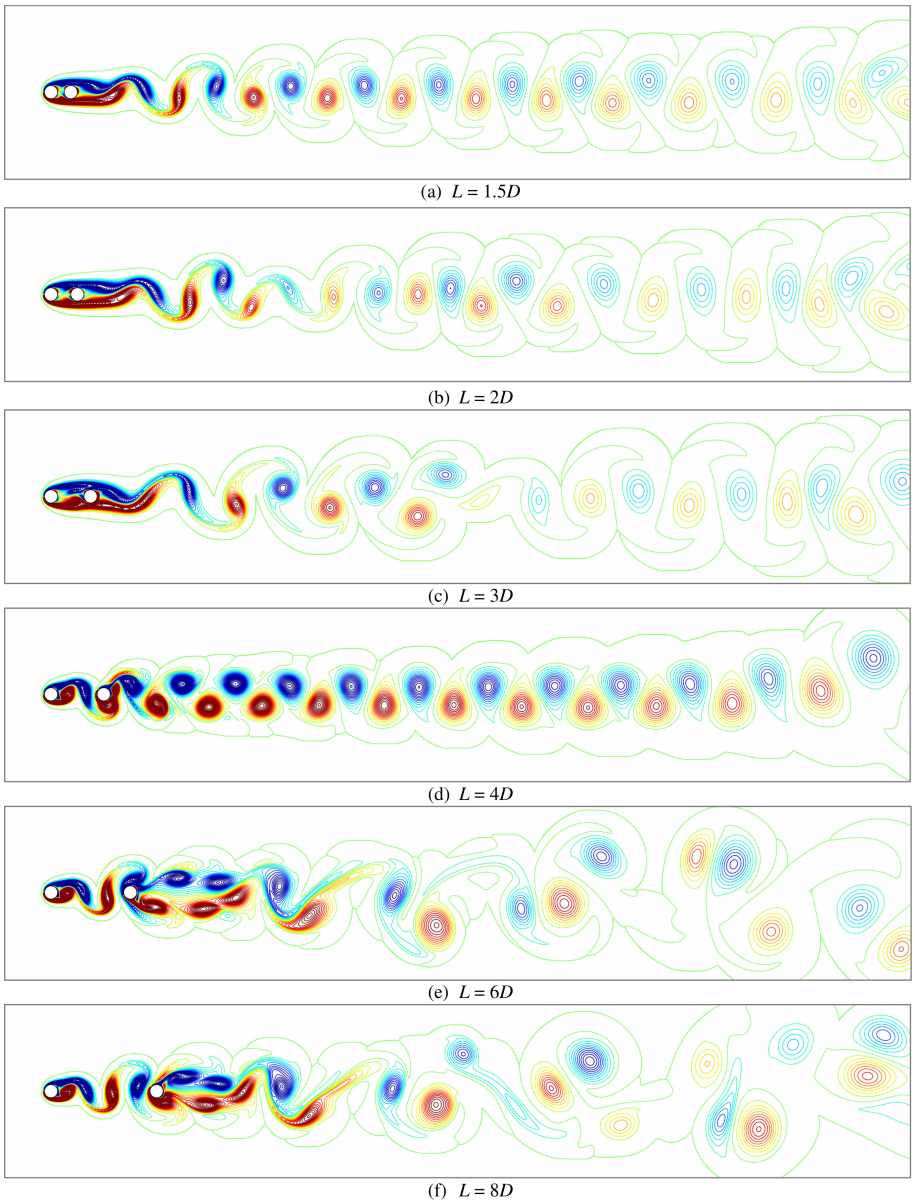

Figure A.9: Instantaneous vorticity distribution at $Re = 200$

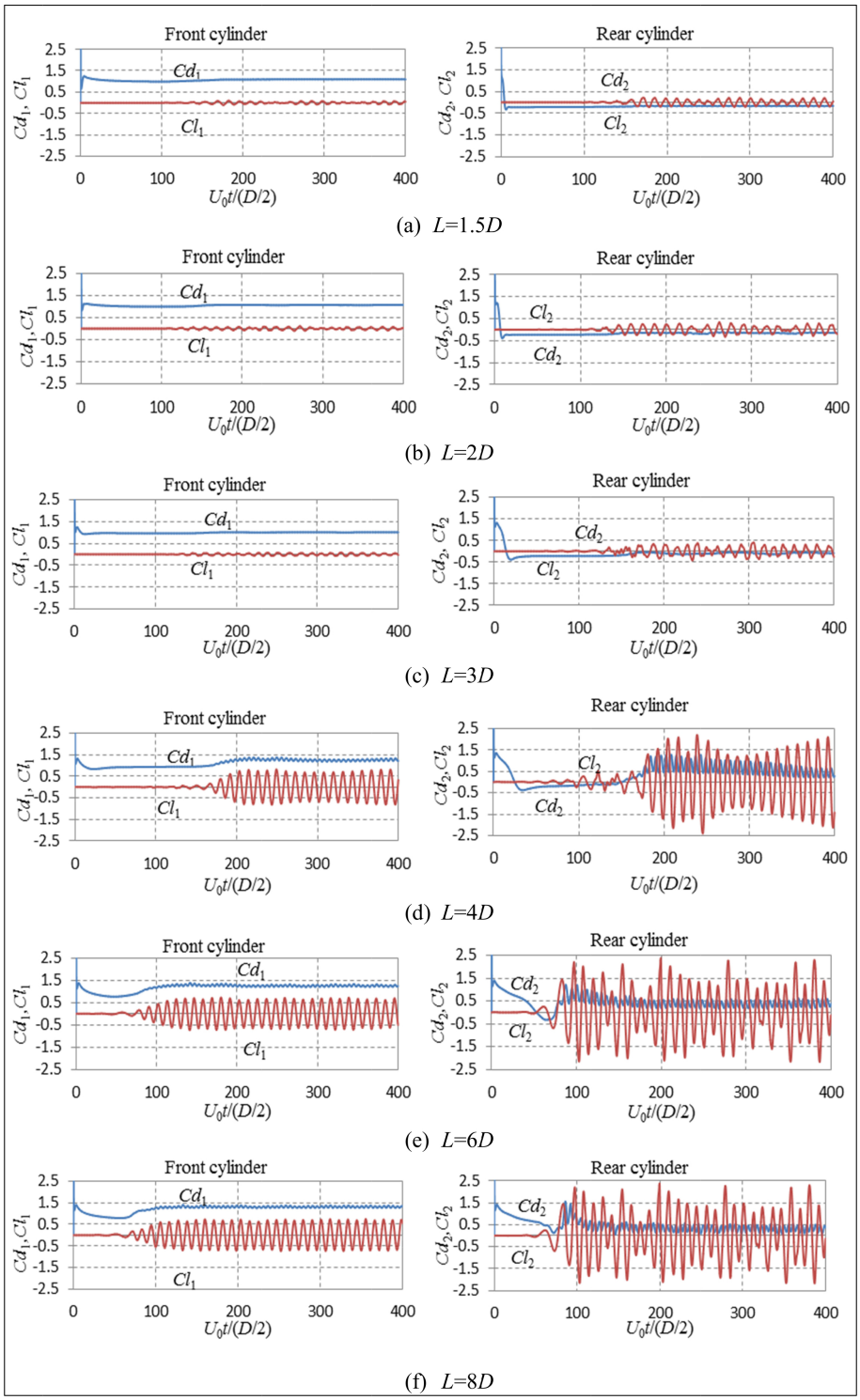

Figure A.10: Time variation of the drag and lift coefficients of each cylinder at $Re = 200$

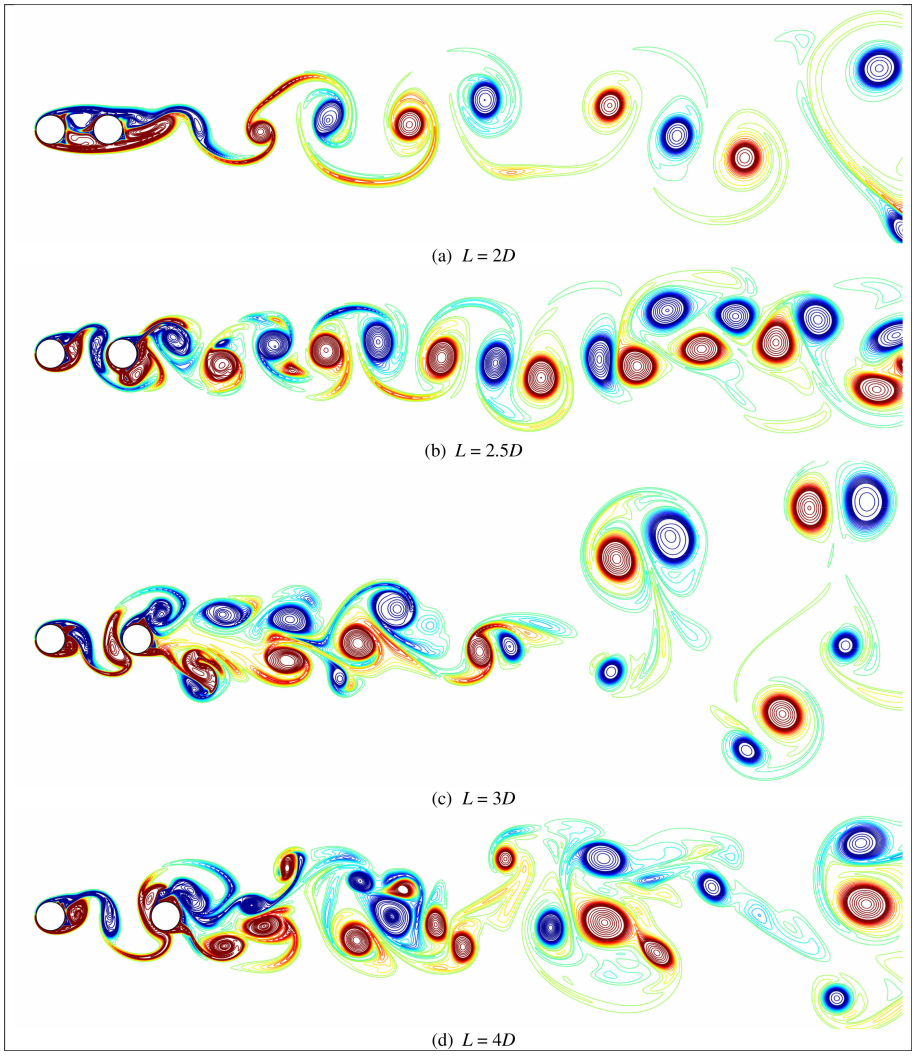

Figure A.11: Instantaneous vorticity distribution at $Re = 1000$

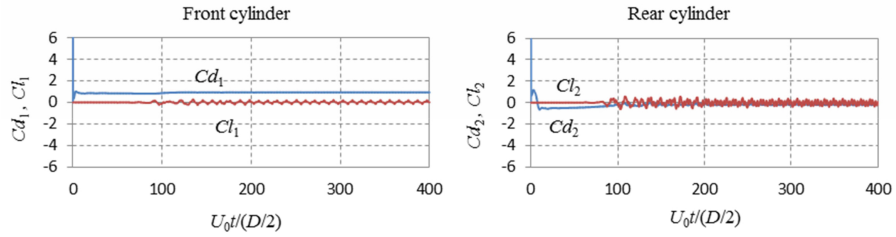

(a) L=2D

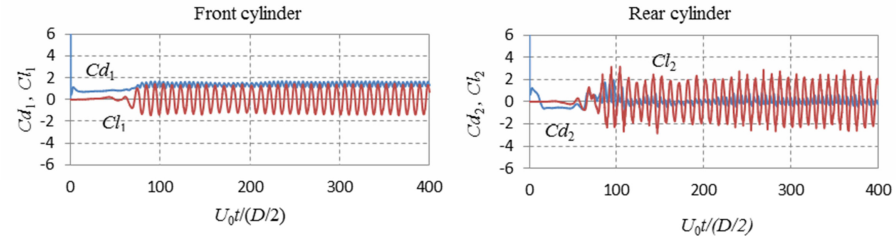

(b) L = 2.5D

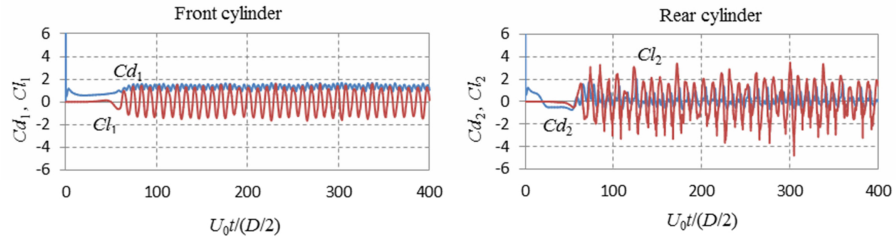

(c) L = 3D

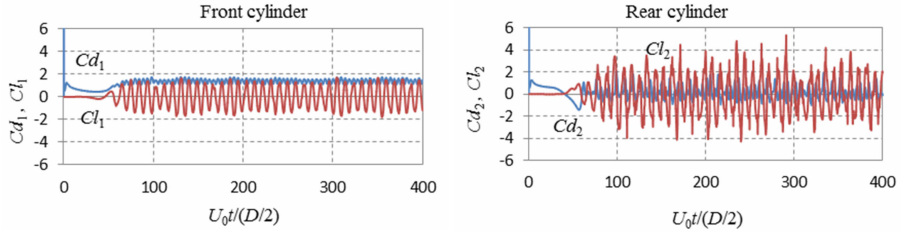

(d) L=4D

Figure A.12: Time variation of drag and lift coefficients of two tandem cylinders at Re = 1000

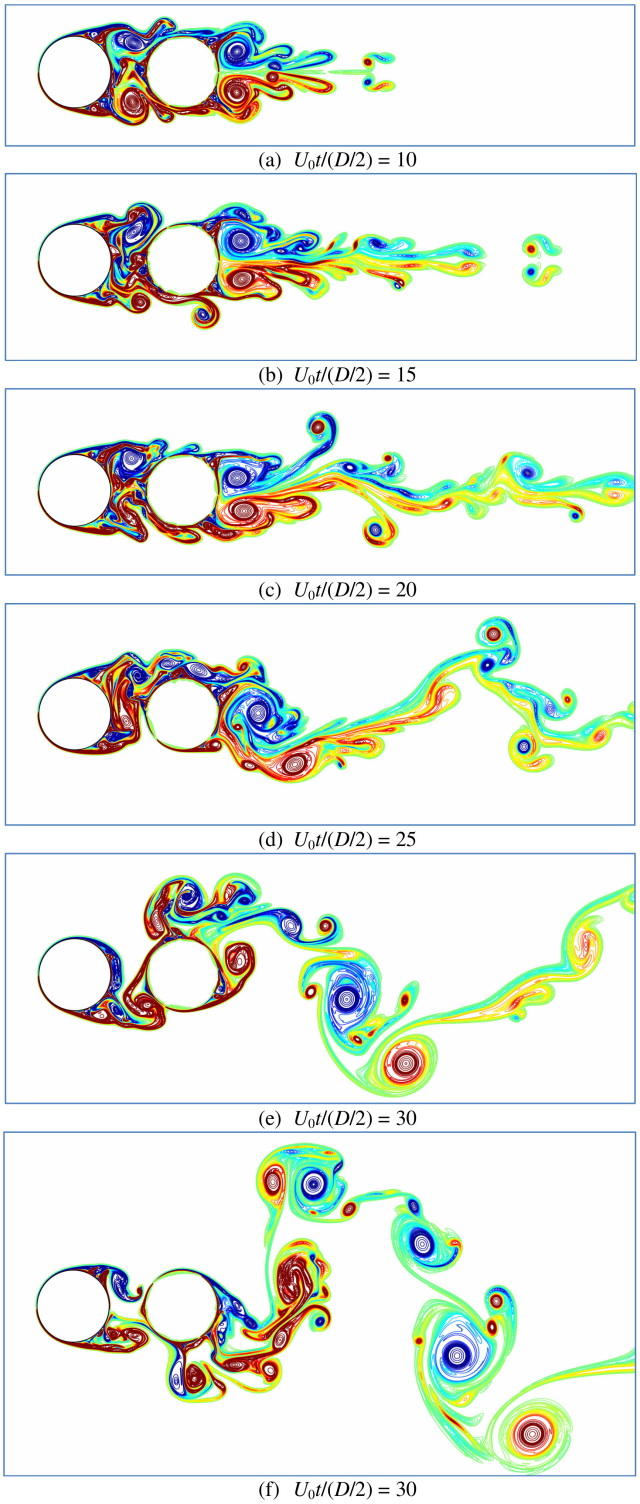

(a) $U_0t/(D/2) = 10$

(b) $U_0t/(D/2) = 15$

(c) $U_0t/(D/2) = 20$

(d) $U_0t/(D/2) = 25$

(e) $U_0t/(D/2) = 30$

(f) $U_0t/(D/2) = 30$

Figure A.13: Time evolution of vorticity distribution at $Re = 9500$ with the distance of $L = 1.5D$

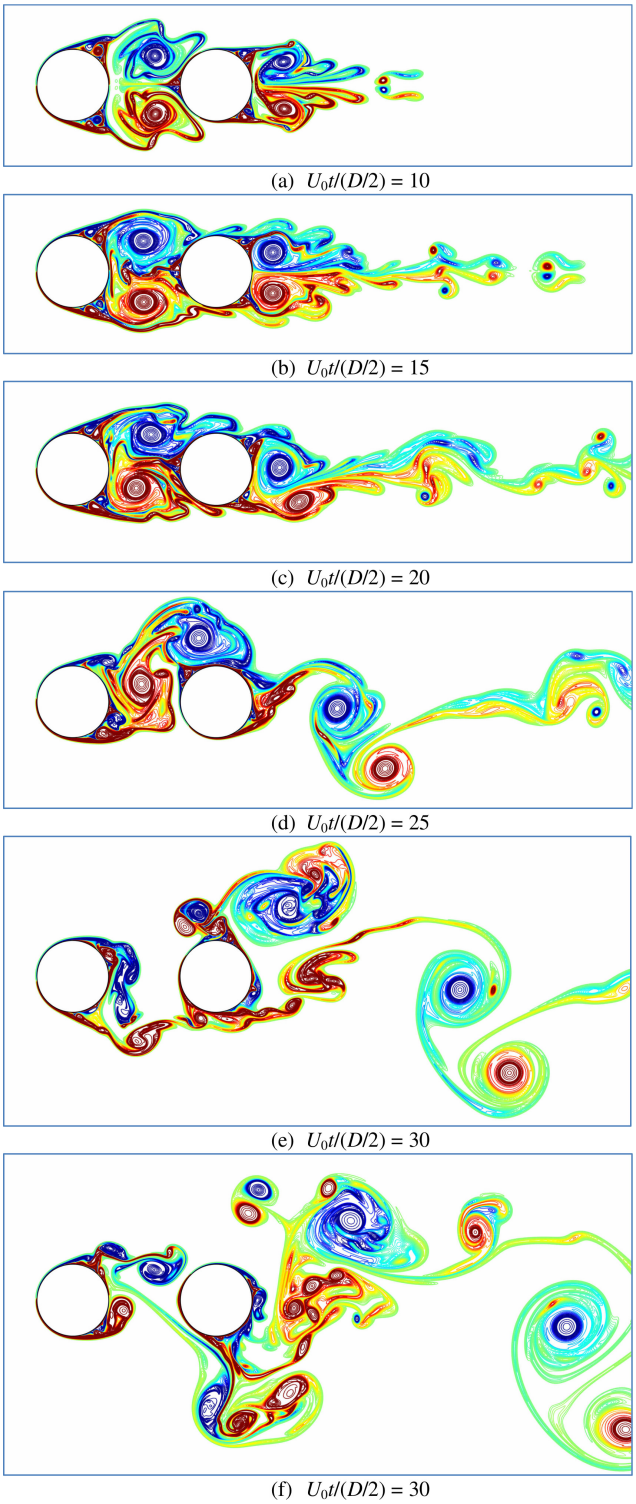

(a) $U_0t/(D/2) = 10$

(b) $U_0t/(D/2) = 15$

(c) $U_0t/(D/2) = 20$

(d) $U_0t/(D/2) = 25$

(e) $U_0t/(D/2) = 30$

(f) $U_0t/(D/2) = 30$

Figure A.14: Time evolution of vorticity distribution at $Re = 9500$ with the distance of $L = 2D$

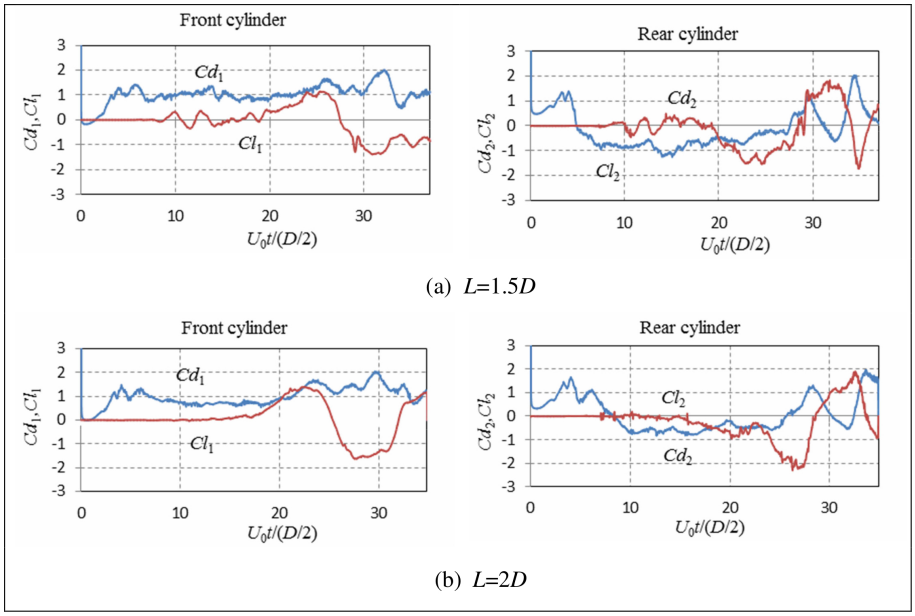

Figure A.15: Time variation of drag and lift coefficients of two tandem cylinders at $Re = 9500$

Appendix B

The momentum equation of the bubbly flow in the velocity–vorticity form

Considering the following equations

$$\alpha_l \frac{D\boldsymbol{u}_l}{Dt} = -\frac{1}{\rho_l}\nabla p + \nu_l \nabla^2 \boldsymbol{u}_l + \alpha_l \boldsymbol{g} \tag{B.1}$$

$$\frac{\partial \boldsymbol{\omega}}{\partial t} + (\boldsymbol{u}_l \cdot \nabla)\boldsymbol{\omega} = (\boldsymbol{\omega} \cdot \nabla)\boldsymbol{u}_l + \frac{\nu_l}{\alpha_l}\nabla^2 \boldsymbol{\omega} + \frac{1}{\alpha_l}\nabla \alpha_l \times \left(\boldsymbol{g} - \frac{D\boldsymbol{u}_l}{Dt}\right) \tag{B.2}$$

where

$$\boldsymbol{\omega} = \nabla \times \boldsymbol{u}_l \tag{B.3}$$

$$\nabla \cdot \boldsymbol{\omega} = 0 \tag{B.4}$$

it is stated that the Eq. (B.2) is obtained by taking the curl operation of the Eq. (B.1).

Proof:

The following properties of the vector calculus identities are used for the expression:

$$\nabla \times \varphi = 0 \tag{B.5}$$

$$\nabla \times (\varphi \mathbf{A}) = \varphi(\nabla \times \mathbf{A}) + \nabla\varphi \times \mathbf{A} \tag{B.6}$$

$$\nabla(\mathbf{A} \cdot \mathbf{B}) = (\mathbf{A} \cdot \nabla)\mathbf{B} + (\mathbf{B} \cdot \nabla)\mathbf{A} + \mathbf{A} \times (\nabla \times \mathbf{B}) + \mathbf{B} \times (\nabla \times \mathbf{A}) \tag{B.7}$$

$$\nabla \times (\mathbf{A} \times \mathbf{B}) = \mathbf{A}(\nabla \cdot \mathbf{B}) - \mathbf{B}(\nabla \cdot \mathbf{A}) + (\mathbf{B} \cdot \nabla)\mathbf{A} - (\mathbf{A} \cdot \nabla)\mathbf{B} \tag{B.8}$$

where φ is a scalar field, and $\mathbf{A}$ and $\mathbf{B}$ are vector fields. When $\mathbf{A} = \mathbf{B}$, the Eq. (B.7) are rewritten as

$$(\mathbf{A} \cdot \nabla)\mathbf{A} = \frac{1}{2}\nabla(\mathbf{A} \cdot \mathbf{A}) - \mathbf{A} \times (\nabla \times \mathbf{A}) = \frac{1}{2}\nabla(\mathbf{A}^2) - \mathbf{A} \times (\nabla \times \mathbf{A}) \tag{B.9}$$

Taking the curl of both sides of the Eq. (B.1), the following equation is obtained

$$\nabla \times \left(\alpha_l \frac{D\boldsymbol{u}_l}{Dt}\right) = \nabla \times \left(-\frac{1}{\rho_l}\nabla p\right) + \nabla \times (\nu_l \nabla^2 \boldsymbol{u}_l) + \nabla \times (\alpha_l \boldsymbol{g}) \tag{B.10}$$

The terms on the right-hand side of the Eq. (B.10) are expressed as

$$\nabla \times \left(-\frac{1}{\rho_l}\nabla p\right) = -\frac{1}{\rho_l}\nabla(\nabla \times p) \overset{\text{Eq. (B.5)}}{=} 0 \tag{B.11}$$

$$\nabla \times (\nu_l \nabla^2 \boldsymbol{u}_l) = \nu_l \nabla^2 (\nabla \times \boldsymbol{u}_l) \overset{\text{Eq.(B.3)}}{=} \nu_l \nabla^2 \boldsymbol{\omega} \tag{B.12}$$

$$\nabla \times \Big(\alpha_l \boldsymbol{g} \Big) \overset{\text{(B.6)}}{=} \alpha_l (\nabla \times \boldsymbol{g}) + \nabla \alpha_l \times \boldsymbol{g} \overset{\text{Eq.(B.5)}}{=} \nabla \alpha_l \times \boldsymbol{g} \tag{B.13}$$

The term on the left-hand side of the Eq. (B.10) is explained as

$$\nabla \times \left(\alpha_l \frac{D\boldsymbol{u}_l}{Dt} \right) \overset{\text{Eq.(B.6)}}{=} \alpha_l \left(\nabla \times \frac{D\boldsymbol{u}_l}{Dt} \right) + \nabla \alpha_l \times \frac{D\boldsymbol{u}_l}{Dt} \tag{B.14}$$

where

$$\frac{D\boldsymbol{u}_l}{Dt} = \frac{\partial \boldsymbol{u}_l}{\partial t} + (\boldsymbol{u}_l \cdot \nabla)\boldsymbol{u}_l \tag{B.15}$$

The Eq. (B.14) is rewritten as

$$\nabla \times \left(\alpha_l \frac{D\boldsymbol{u}_l}{Dt} \right) \overset{\text{Eq.(B.3)}}{=} \alpha_l \left\{ \frac{\partial \boldsymbol{\omega}}{\partial t} + \nabla \times \Big[(\boldsymbol{u}_l \cdot \nabla)\boldsymbol{u}_l \Big] \right\} + \nabla \alpha_l \times \frac{D\boldsymbol{u}_l}{Dt} \tag{B.16}$$

where

$$\nabla \times \Big[(\boldsymbol{u}_l \cdot \nabla)\boldsymbol{u}_l \Big] \overset{\text{Eq.(B.9)}}{=} \nabla \times \Big[\frac{1}{2} \nabla (\boldsymbol{u}_l^2) - \boldsymbol{u}_l \times (\nabla \times \boldsymbol{u}_l) \Big] \overset{\text{Eqs.(B.5),(B.3)}}{=} -\nabla \times (\boldsymbol{u}_l \times \boldsymbol{\omega}) \tag{B.17}$$

Applying the property of vector calculus identity, Eq. (B.8), the Eq. (B.17) is obtained as

$$\nabla \times \Big[(\boldsymbol{u}_l \cdot \nabla)\boldsymbol{u}_l \Big] = -\Big[\boldsymbol{u}_l (\nabla \cdot \boldsymbol{\omega}) - \boldsymbol{\omega} (\nabla \cdot \boldsymbol{u}_l) + (\boldsymbol{\omega} \cdot \nabla)\boldsymbol{u}_l - (\boldsymbol{u}_l \cdot \nabla)\boldsymbol{\omega} \Big] \tag{B.18}$$

The term $\boldsymbol{\omega}(\nabla \cdot \boldsymbol{u}_l)$ is ignored because its value is very small compared to the terms of $(\boldsymbol{\omega} \cdot \nabla)\boldsymbol{u}_l$ and $(\boldsymbol{u}_l \cdot \nabla)\boldsymbol{\omega}$. Therefore, the Eq. (B.18) is rewritten as

$$\nabla \times \Big[(\boldsymbol{u}_l \cdot \nabla)\boldsymbol{u}_l \Big] \overset{\text{Eq.(B.4)}}{=} -\Big[(\boldsymbol{\omega} \cdot \nabla)\boldsymbol{u}_l - (\boldsymbol{u}_l \cdot \nabla)\boldsymbol{\omega} \Big] \tag{B.19}$$

When substituting the Eq. (B.19) into the Eq. (B.16), the left-hand side of the Eq. (B.10) is expressed as

$$\nabla \times \left(\alpha_l \frac{D\boldsymbol{u}_l}{Dt} \right) = \alpha_l \left(\frac{\partial \boldsymbol{\omega}}{\partial t} - (\boldsymbol{\omega} \cdot \nabla)\boldsymbol{u}_l + (\boldsymbol{u}_l \cdot \nabla)\boldsymbol{\omega} \right) + \nabla \alpha_l \times \frac{D\boldsymbol{u}_l}{Dt} \tag{B.20}$$

When substituting the Eqs. (B.11), (B.12), (B.13), and (B.20) into the Eq. (B.10), a result is obtained as follows:

$$\alpha_l \left(\frac{\partial \boldsymbol{\omega}}{\partial t} - (\boldsymbol{\omega} \cdot \nabla)\boldsymbol{u}_l + (\boldsymbol{u}_l \cdot \nabla)\boldsymbol{\omega} \right) + \nabla \alpha_l \times \frac{D\boldsymbol{u}_l}{Dt} = \nu_l \nabla^2 \boldsymbol{\omega} + \nabla \alpha_l \times \boldsymbol{g} \tag{B.21}$$

The Eq. (B.21) is rearranged as

$$\frac{\partial \boldsymbol{\omega}}{\partial t} + (\boldsymbol{u}_l \cdot \nabla)\boldsymbol{\omega} = (\boldsymbol{\omega} \cdot \nabla)\boldsymbol{u}_l + \frac{\nu_l}{\alpha_l} \nabla^2 \boldsymbol{\omega} + \frac{1}{\alpha_l} \nabla \alpha_l \times \left(\boldsymbol{g} - \frac{D\boldsymbol{u}_l}{Dt} \right) \tag{B.22}$$

Therefore, the statement is proved.

Appendix C

Convective outflow boundary condition

The general form of convective outflow boundary condition is rewritten as

$$\frac{\partial f(\boldsymbol{x},t)}{\partial t} + u_c(\boldsymbol{x},t)\big[\nabla(f(\boldsymbol{x},t))\cdot\hat{n}\big] \tag{C.1}$$

where $u_c(\boldsymbol{x},t)$ is the scalar convective velocity and $\hat{n}$ is the unit normal vector of the surface $\partial\Omega$. Considering this boundary condition for the liquid phase at the top domain ($z = z_{max}$), the following equations are expressed as

$$\frac{\partial \boldsymbol{\omega}}{\partial t} + u_c(z_{max},t)\frac{\partial \boldsymbol{\omega}}{\partial z} = 0 \tag{C.2}$$

$$\frac{\partial \boldsymbol{\psi}}{\partial t} + u_c(z_{max},t)\frac{\partial \boldsymbol{\psi}}{\partial z} = 0 \tag{C.3}$$

$$\frac{\partial \phi}{\partial t} + u_c(z_{max},t)\frac{\partial \phi}{\partial z} = 0 \tag{C.4}$$

$$\frac{\partial \boldsymbol{u}_l}{\partial t} + u_c(z_{max},t)\frac{\partial \boldsymbol{u}_l}{\partial z} = 0 \tag{C.5}$$

Eq. (C.2), the condition of the vorticity field, is discretized using the staggered-grid finite-difference schemes as

$$\frac{\omega^{n+1}_{x,(i,j,k_{max})} - \omega^{n}_{x,(i,j,k_{max})}}{\Delta t} + u_c(z_{max},t) + \frac{\omega^{n}_{x,(i,j,k_{max})} - \omega^{n}_{x,(i,j,k_{max}-1)}}{\Delta z} = 0 \tag{C.6}$$

$$\frac{\omega^{n+1}_{y,(i,j,k_{max})} - \omega^{n}_{y,(i,j,k_{max})}}{\Delta t} + u_c(z_{max},t) + \frac{\omega^{n}_{y,(i,j,k_{max})} - \omega^{n}_{y,(i,j,k_{max}-1)}}{\Delta z} = 0 \tag{C.7}$$

$$\frac{\omega^{n+1}_{z,(i,j,k_{max})} - \omega^{n}_{z,(i,j,k_{max})}}{\Delta t} + u_c(z_{max},t) + \frac{3\omega^{n}_{z,(i,j,k_{max})} - 4\omega^{n}_{z,(i,j,k_{max}-1)} + \omega^{n}_{z,(i,j,k_{max}-2)}}{\Delta z} = 0 \tag{C.8}$$

The discretization of Eq. (C.3) is the same as that of Eq. (C.2) because the arrangement of components of $\boldsymbol{\omega}$ and $\boldsymbol{\psi}$ on the staggered grid is the same. Eqs. (C.4) and (C.5), the conditions of the scalar potential velocity and the velocity field, respectively, are discretized as

$$\frac{\phi^{n+1}_{(i,j,k_{max})} - \phi^{n}_{(i,j,k_{max})}}{\Delta t} + u_c(z_{max},t) + \frac{3\phi^{n}_{(i,j,k_{max})} - 4\phi^{n}_{(i,j,k_{max}-1)} + \phi^{n}_{(i,j,k_{max}-2)}}{\Delta z} = 0 \tag{C.9}$$

$$\frac{u^{n+1}_{x,(i,j,k_{max})} - u^{n}_{x,(i,j,k_{max})}}{\Delta t} + u_c(z_{max},t) + \frac{3u^{n}_{x,(i,j,k_{max})} - 4u^{n}_{x,(i,j,k_{max}-1)} + u^{n}_{x,(i,j,k_{max}-2)}}{\Delta z} = 0 \tag{C.10}$$

$$\frac{u^{n+1}_{y,(i,j,k_{max})} - u^{n}_{y,(i,j,k_{max})}}{\Delta t} + u_c(z_{max}, t) + \frac{3u^{n}_{y,(i,j,k_{max})} - 4u^{n}_{y,(i,j,k_{max}-1)} + u^{n}_{y,(i,j,k_{max}-2)}}{\Delta z} = 0 \tag{C.11}$$

$$\frac{u^{n+1}_{z,(i,j,k_{max})} - u^{n}_{z,(i,j,k_{max})}}{\Delta t} + u_c(z_{max}, t) + \frac{u^{n}_{z,(i,j,k_{max})} - u^{n}_{z,(i,j,k_{max}-1)}}{\Delta z} = 0 \tag{C.12}$$

The scalar convective velocity $u_c(z_{max}, t)$ is calculated based on each simulation case.

Appendix D

Discretization of Navier–Stokes equation

D.1 Expression of forms and terms of Navier–Stokes equation

The Navier–Stokes momentum equation for the fluid is written in the velocity–vorticity form as

$$\frac{\partial \boldsymbol{\omega}}{\partial t} + \nabla \cdot (\boldsymbol{u}\boldsymbol{\omega}) = \nabla \cdot (\boldsymbol{\omega}\boldsymbol{u}) + \nu \nabla^2 \boldsymbol{\omega} \tag{D.1}$$

Applying the following property of vector calculus identities:

$$\nabla \cdot (\boldsymbol{b}\,\boldsymbol{a}) = \nabla \cdot (\boldsymbol{b}\boldsymbol{a}^T) = \boldsymbol{a}(\nabla \cdot \boldsymbol{b}) + (\boldsymbol{b} \cdot \nabla)\boldsymbol{a} \tag{D.2}$$

where $\boldsymbol{a}$ and $\boldsymbol{b}$ are vectors, the second term on the left-hand side and first term on the right-hand side of Eq. D.1 can be expressed as:

$$\nabla \cdot (\boldsymbol{u}\boldsymbol{\omega}) = \boldsymbol{\omega}(\nabla \cdot \boldsymbol{u}) + (\boldsymbol{u} \cdot \nabla)\boldsymbol{\omega} = (\boldsymbol{u} \cdot \nabla)\boldsymbol{\omega} \tag{D.3}$$

$$\nabla \cdot (\boldsymbol{\omega}\boldsymbol{u}) = \boldsymbol{u}(\nabla \cdot \boldsymbol{\omega}) + (\boldsymbol{\omega} \cdot \nabla)\boldsymbol{u} = (\boldsymbol{\omega} \cdot \nabla)\boldsymbol{u} \tag{D.4}$$

because of $\nabla \cdot \boldsymbol{u} = 0$ (incompressible flow) and $\nabla \cdot \boldsymbol{\omega} = 0$ ($\boldsymbol{\omega}$ is a solenoidal vector). Substituting Eqs. (D.3) and (D.4) into Eq. (D.1), the Navier–Stokes momentum equation is written in convective form as

$$\frac{\partial \boldsymbol{\omega}}{\partial t} + (\boldsymbol{u} \cdot \nabla)\boldsymbol{\omega} = (\boldsymbol{\omega} \cdot \nabla)\boldsymbol{u} + \nu \nabla^2 \boldsymbol{\omega} \tag{D.5}$$

In Eq. (D.1), the $\boldsymbol{\omega}\boldsymbol{u}$ is dyadic product of two vectors, also expressed as outer product or tensor dot product of two vectors, $(\boldsymbol{\omega} \otimes \boldsymbol{u})$, and they have a relation as

$$\boldsymbol{\omega}\boldsymbol{u} \equiv \boldsymbol{\omega} \otimes \boldsymbol{u} \equiv \boldsymbol{\omega}\boldsymbol{u}^T = \begin{pmatrix} \omega_x & \omega_y & \omega_z \end{pmatrix} \begin{pmatrix} u \\ v \\ w \end{pmatrix} = \begin{pmatrix} \omega_x u & \omega_x v & \omega_x w \\ \omega_y u & \omega_y v & \omega_y w \\ \omega_z u & \omega_z v & \omega_z w \end{pmatrix} \tag{D.6}$$

The i-th component of vortex stretching term $\nabla \cdot (\boldsymbol{\omega}\boldsymbol{u})$ is calculated as:

$$\big(\nabla \cdot (\boldsymbol{\omega}\boldsymbol{u})\big)_i = \nabla \cdot (\boldsymbol{\omega} u_i) = (\nabla \cdot \boldsymbol{\omega})u_i + (\boldsymbol{\omega} \cdot \nabla)u_i = (\boldsymbol{\omega} \cdot \nabla)u_i \tag{D.7}$$

Eq. D.7 is further expressed as

$$\begin{cases} \big(\nabla\cdot(\boldsymbol{\omega u})\big)_x &= \omega_x\dfrac{\partial u}{\partial x}+\omega_y\dfrac{\partial u}{\partial y}+\omega_z\dfrac{\partial u}{\partial z} \\ \big(\nabla\cdot(\boldsymbol{\omega u})\big)_y &= \omega_x\dfrac{\partial v}{\partial x}+\omega_y\dfrac{\partial v}{\partial y}+\omega_z\dfrac{\partial v}{\partial z} \\ \big(\nabla\cdot(\boldsymbol{\omega u})\big)_z &= \omega_x\dfrac{\partial w}{\partial x}+\omega_y\dfrac{\partial w}{\partial y}+\omega_z\dfrac{\partial w}{\partial z} \end{cases} \tag{D.8}$$

where $\big(\nabla\cdot(\boldsymbol{\omega u})\big)_x$, $\big(\nabla\cdot(\boldsymbol{\omega u})\big)_y$ and $\big(\nabla\cdot(\boldsymbol{\omega u})\big)_z$ indicate the components of $\big(\nabla\cdot(\boldsymbol{\omega u})\big)$ in x, y and z directions, respectively. Three components of the diffusion term in Eq. (D.1), are expressed as

$$\begin{cases} \big(\nu\nabla^2\boldsymbol{\omega}\big)_x &= \nu\Big(\dfrac{\partial^2\omega_x}{\partial x^2}+\dfrac{\partial^2\omega_x}{\partial y^2}+\dfrac{\partial^2\omega_x}{\partial z^2}\Big) \\ \big(\nu\nabla^2\boldsymbol{\omega}\big)_y &= \nu\Big(\dfrac{\partial^2\omega_y}{\partial x^2}+\dfrac{\partial^2\omega_y}{\partial y^2}+\dfrac{\partial^2\omega_y}{\partial z^2}\Big) \\ \big(\nu\nabla^2\boldsymbol{\omega}\big)_z &= \nu\Big(\dfrac{\partial^2\omega_z}{\partial x^2}+\dfrac{\partial^2\omega_z}{\partial y^2}+\dfrac{\partial^2\omega_z}{\partial z^2}\Big) \end{cases} \tag{D.9}$$

D.2 Regular- and staggered-grid finite difference schemes

Considering a point A at middle of the point $n-1$ and and n, i.e., $x_A=(x_{n-1}+x_n)/2$, the value of a function f at x_A is interpolated by using formulas with second and fourth orders of accuracy, respectively, as follows:

$$f(x_A)=\frac{f_{n-1}+f_n}{2}+\mathcal{O}(\Delta^2) \tag{D.10}$$

$$f(x_A)=\frac{-f_{n-2}+9f_{n-1}+9f_n-f_{n+1}}{16}+\mathcal{O}(\Delta^4) \tag{D.11}$$

where Δ is width of a grid cell. The first derivatives of f according to x at x_A at x_A are expressed as

$$f^{'}(x_A)=\frac{f_n-f_{n-1}}{\Delta}+\mathcal{O}(\Delta^2) \tag{D.12}$$

$$f^{'}(x_A)=\frac{f_{n-2}-27f_{n-1}+27f_n-f_{n+1}}{24\Delta}+\mathcal{O}(\Delta^4) \tag{D.13}$$

In current method, the stretching term is approximated by using fourth-order accuracy, Eqs. (D.11) and (D.13). In the diffusion term, the second derivative is calculated on the regular grid as

$$f_n^{''}=\frac{-f_{n-2}+16f_{n-1}-30f_n+16f_{n+1}-f_{n+2}}{12\Delta^2}+\mathcal{O}(\Delta^4) \tag{D.14}$$

Bibliography

M. Alam and V. Arakeri. Observations on transition in plane bubble plume. *J. Fluid Mech.*, 254:363–374, 1993.

S. V. Ape, M. Martin, and N. A. Patankar. A numerical method for fully resolved simulation (FRS) of grid body particle-flow interactions in complex flows. *J. Comput. Phys.*, 228(8):2712–2738, 2009.

T. Auton, J. C. R. Hunt, and M. Prund'home. The force exerted on a body in inviscid unsteady non-uniform rotational flow. *J. Fluid Mech.*, 197:241–257, 1988.

K. Bamardouf and D. A. McNeil. Experimental and numerical investigation of two-phase pressure drop in vertical cross-flow over a horizontal tube bundle. *Applied Thermal Engineering*, 29(7):1356–1365, 2009.

L. A. Barba, A. Leonard, and C. B. Allen. Numerical investigations of the accuracy of the vortex method with and without remeshing. *16th AIAA Computational Fluid Dynamics Conference, Floria*, p. 11 pages, 2003.

M. Bergdorf, P. Koumoutsakos, and A. Leonard. Direct numerical simulations of vortex rings at Re = 7500. *J. Fluid Mech.*, 581:495–505, 2007.

C. K. Birdsall and D. Fuss. Clouds-in-clouds, clouds-in-cells physics for many-body plasma simulation. *J. Comput. Phys.*, 3(4):494–511, 1969.

M. Braza, P. Chassaing, and H. Ha Minh. Numerical study and physical analysis of the pressure and velocity fields in the near wake of a circular cylinder. *J. Fluid Mech.*, 165: 79–130, 1986.

M. Brocchini and D. H. Peregrine. The dynamics of strong turbulence at free surfaces. part 1. description. *J. Fluid Mech.*, 449:225–254, 2001.

O. Caballina, E. Climent, and J. Dusek. Two-way coupling simulations of instabilities in a plane bubble plume. *J. Physics of Fluids*, 15(6):1535–1544, 2003.

P. Chatelain, A. Curioni, M. Bergdorf, D. Rossinelli, W. Andreoni, and P. Koumoutsakos. Billion vortex particle direct numerical simulations of aircraft wakes. *Comput. Method Applied Mechanics*, 197(13-16):1296–1304, 2008.

B. Chen, Z. Wang, and T. Uchiyama. Numerical simulation of bubble cluster induced flow by three-dimensional vortex-in-cell method. *J. Fluid Engineering*, 136(13-16):0813011–8130116, 2014.

A. Chouippe, E. Climent, D. Legendre, and C. Gabillet. Numerical simulation of bubble dispersion in turbulent Taylor-Couette flow. *Phys. Fluids*, 26:043304–043326, 2014.

J. P. Christiansen. Numerical simulation of hydrodynamics by the method of point vortices. *J. Comput. Phys.*, 13(3):363–379, 1973.

A. J. Cihonski, J. R. Finn, and S. V. Apte. Volume displacement effects during bubble entrainment in a travelling vortex ring. *J. Fluid Mech.*, 721:225–267, 2013.

R. Cocle, G. Winckelmens, and G. Daeninck. Combining the vortex-in-cell and parallel fast multipole methods for efficient domain decomposition simulations. *J. Comput. Phys.*, 227(21):9091–9120, 2008.

G.-H. Cottet and P. D. Koumoutsakos. *Vortex Methods: Theory and Practice*. Cambridge University Press, 2000.

G.-H. Cottet and P. Poncet. Particle methods for direct numerical simulations of three-dimensional wakes. *J. Turbulence*, 3(38):1–9, 2002.

G.-H. Cottet and P. Poncet. Advances in direct numerical simulations of 3D wall-bounded flows by vortex-in-cell methods. *J. Comput. Phys.*, 193(1):136–158, 2003.

E. Daniel, R. Saurel, M. Larini, and J. C. Loraud. A multiphase formulation for two phase flows. *Int. J. Numerical Methods for Heat and Fluid Flow*, 4(3):269–280, 1994.

A. K. Das and P. K. Das. Bubble evolution through submerged orifice smoothed particle hydrodynamics: Basic formulation and model validation. *Chem. Eng. Sci.*, 64(10): 2281–2290, 2009.

T. Degawa and T. Uchiyama. Numerical simulation of bubbly flow around two tandem square-section cylinders by vortex method. *J. Mechanical Eng. Sci., IMechE*, 222(2): 225–234, 2008.

E. Delnoij, F. A. Lammers, J. A. M. Kuipers, and W. P. M. van Swaaij. Dynamic simulation of dispersed gas-liquid two-phase flow using a discrete bubble model. *Chem. Eng. Sci.*, 52(9):1429–1458, 1997a.

E. Delnoij, J. A. M. Kuipers, and W. P. M. van Swaaij. Dynamic simulation of gas-liquid two-phase flow: effect of column aspect ratio on the flow structure. *Chem. Eng. Sci.*, 52(21–22):3759–3772, 1997b.

E. Delnoij, J. A. M. Kuipers, and W. P. M. van Swaaij. A three-dimensional CFD model for gas-liquid bubble columns. *Chem. Eng. Sci.*, 54(13–14):2217–2226, 1999.

R. Deng, C. H. Wang, and K. A. Smith. Bubble behavior in a Taylor vortex. *Phys. Rev. E.*, 73:036306–036310, 2006.

M. T. Dhotre, N. G. Deen, B. Niceno, Z. Khan, and J. B. Joshi4. Large eddy simulation for dispersed bubbly flows: A review. *Int. J. Chemical Eng.*, 2013(Article ID 343276): 22 pages, 2013.

K. Domon, O. Ishihara, and S. Watanabe. Mass transport by a vortex ring. *J. Phys. Soc. Jpn.*, 69:120–123, 2000.

O. A. Druzhinin and S. E. Elghobashi. Direct numerical simulations of bubble-laden turbulent flows using the two-fluid formulation. *Phys. Fluids*, 10(3):685–697, 1998.

K. A. Elrais, W. Eckerle, G. Ahmadi, and A. H. Eraslan. Simulation of transient three-dimensional natural convection and saturated pool boiling. *Int. J. Numerical Methods for Heat and Fluid Flow*, 2(2):139–154, 1992.

A. Ferrante and S. E. Elghobashi. On the effects of microbubbles on taylor-green vortex flow. *J. Fluid Mech.*, 572:145–177, 2007.

J. Finn, E. Shams, and S. V. Apte. Modeling and simulation of multiple bubble entrainment and interactions with two dimensional vortical flows. *Phys. Fluids*, 23:023301–023321, 2011.

B. Fraga, T. Stoesser, C. C. Lai, and S. A. Socolofky. A LES-based Eulerian-Lagrangian approach to predict the dynamics of bubble plumes. *J. Ocean Modelling*, 97:27–36, 2016.

M. Gazzola, P. Chatelain, W. M. van Rees, and P. Koumoutsakos. Simulation of single and multiple swimmers with non-divergence free deforming geometries. *J. Comput. Phys.*, 230(19):7093–7114, 2011.

J. Hua and J. Lou. Numerical simulation of bubble rising in viscous liquid. *J. Comput. Physics*, 222(2):769–795, 2007.

Y. Huang, W. Wu, and H. Zhang. Numerical study of particle dispersion in the wake of gas-particle flows past a circular cylinder using discrete vortex method. *Powder Technology*, 162(1):73–81, 2006.

M. Ihmsen, J. Bader, G. Akinci, and M. Teschner. Animation of air bubbles with sph. *Proc. of the Int. Conf. on Computer Graphics Theory and Applications*, p. 9 pages, 2011.

A. Inoue, Y. Kozawa, M. Yokosawa, and S. Aoki. Studies on two-phase cross flow. part i: Flow characteristics around a cylinder. *Int. J. Multiphase Flow*, 12(2):149–167, 1986.

J. Jeong and F. Hussanin. On the identification of a vortex. *J. Fluid Mech.*, 285:69–94, 1995.

W. Jester and Y. Kallinderis. Numerical study of incompressible flow about fixed cylinder pairs. *Journal of Fluids and Structures*, 17(4):561–577, 2003.

S. T. Johansen and F. Boysan. Fluid dynamics in bubble stirred ladles: Part ii. *Mathematical modelling*, 19(5):755–764, 1988.

T. Kitagawa and H. Ohta. Numerical investigation on flow around circular cylinders in tandem arrangement at a subcritical Reynolds numbers. *J. Fluids and Structures*, 24 (5):680–699, 2008.

Z. G. Kostic and S. N. Oka. Fluid flow and heat transfer with two cylinders in cross flow. *Int. J. Heat Mass Transfer*, 15(2):279–299, 1972.

P. Koumoutsakos and A. Leonard. High-resolution simulations of the flow around an impulsively started cylinder using vortex methods. *J. Fluid Mech.*, 296(10):1–38, 1995.

F. Krause, S. Schttenberg, and U. Fritsching. Modelling and simulation of flow boiling heat transfer. *Int. J. Numerical Methods for Heat and Fluid Flow*, 20(3):312–331, 2010.

T. C. Kuo, C. Pan, and C. C. Chieng. Eulerian-Lagrangian computations on phase distribution of two-phase bubbly flows. *Int. J. Numerical methods in fluids*, 24(6):579–593, 1997.

S. Lan and J. Garca. Study of four-way coupling on turbulent particle-laden jet flows. *Chem. Eng. Sci.*, 61(20):6775–6785, 2006.

H. Y. Lian, G. Noghrehkar, A. M. C. Chan, and M. Kawaji. Effect of void fraction on vibrational behavior of tubes in tube bundle under two-phase cross flow. *J. Vibration and Acoustics*, 119(3):457–463, 1999.

L. Lucy. A numerical approach to the testing of the fission hypothesis. *Astronomical Journal*, 82:1013–1024, 1977.

I. M. Mazzitelli, D. Lohse, and F. Toschi. On the relevance of the lift force in bubbly turbulence. *J. Fluid Mech.*, 488(2):283–313, 2003.

M. Meister and W. Rauch. Modelling aerated flows with smoothed particle hydrodynamics. *J. Hydoinformatics*, 17(4):493–504, 2015.

J. R. Meneghini and F. Saltara. Numerical simulation of flow interference between two circular cylinders in tandem and side-by-side arrangements. *J. Fluids and Structures*, 15(2):327–350, 2001.

J. H. Milgram. Mean flow in round bubble plumes. *J. Fluid Mech.*, 133:345–376, 1983.

C. Mimeau, F. Gallizio, G.-H. Cottet, and I. Mortazavi. Vortex penalization method for bluff body flows. *Int. J. Numerical Methods in Fluids*, 79(2):55–83, 2015.

S. Mittal and V. Kumar. Flow-induced vibrations of a light circular cylinder at Reynolds numbers 10^3 to 10^4. *J. Sound and vibration*, 245(5):923–946, 2001.

S. Mittal, V. Kumar, and A. Raghuvanshi. Unsteady incompressible flows past two cylinders in tandem and staggered arrangements. *Int. J. Numerical Methods in Fluids*, 25 (11):1315–1344, 1997.

J. J. Monaghan. Extrapolating B splines for interpolation. *J. Comput. Phys.*, 60(2): 253–262, 1985.

Y. Murai and Y. Matsumoto. Numerical simulation of the three-dimensional structure of a bubble plume. *J. Fluids Eng.*, 122:754–760, 2000.

Y. Murai, T. Sasaki, M. Ishikawa, and F. Yamamoto. Bubble-driven convection around cylinders confined in a channel. *J. Fluids Eng.*, 127(1):117–123, 2005.

F. Noca, D. Shiels, and D. Jeon. A comparison of methods for evaluating time-dependent fluid dynamic forces on bodies, using only velocity fields and their derivatives. *J. Fluids and Structures*, 13(15):551–578, 1999.

G. F. Oweis, I. E. van der Hout, G. Tryggvason, and S. L. Ceccio. Capture and inception of bubbles near line vortices. *Phys. Fluids*, 17(2):022105–022119, 2005.

R. Pasquetti and R. Bwemba. A spectral algorithm for the stokes problem in vorticity-vector potential formulation and cylindrical geometry. *Computer Methods in Applied Mechanics and Engineering*, 117(1–2):71–90, 1994.

C. S. Peskin. Flow patterns around heart valves: a numerical method. *J. Comput. Phys.*, 10(2):252–271, 1972.

P. Poncet. *Mthodes particulaires pour la simulation des sillages tridimensionnels, Ph.D. Thesis*. University Joseph Fourier, Grenoble, France, 2001.

J. T. Rasmussen, G.-H. Cottet, and J. H. Walther. A multiresolution remeshed vortex-in-cell algorithm using patches. *J. Comput. Phys.*, 230(17):6742–6755, 2011.

R. Raul, P. S. Bernard, and F. T. Buckley. An application of the vorticityvector potential method to laminar cube flow. *Int. J. Numerical Methods in Fluids*, 10:875–888, 1990.

D. Rossinelli, M. Bergdorf, G.-H. Cottet, and P. Koumoutsakos. Gpu accelerated simulations of bluff body flows using vortex particle methods. *J. Comput. Phys.*, 229(9): 3316–3333, 2010.

Y. Sato and K. Sekoguchi. Liquid velocity distribution in two-phase bubble flow. *Int. J. Multiphase flow*, 2(1):79–95, 1975.

M. P. Schwarz and W. Turner. Applicability of the standard $k - \epsilon$ turbulence model to gas-stirred baths. *Appl. Math. Modell.*, 12:273–279, 1988.

S. A. Socolofsky, M.ASCE, and D. G. S. T. Bhaumik. Double-plume integral models for near-field mixing in multiphase plumes. *J. Hydraulic Engineering*, 134(6):772–783, 2008.

A. Sokolichin and G. Eigenberger. Dynamic numerical simulation of gas-liquid two-phase flows Euler/Euler versus Euler/Lagrange. *Chem. Eng. Sci.*, 52(4):611–626, 1997.

A. Sokolichin and G. Eigenberger. Applicability of the standard $k - \epsilon$ turbulence model to the dynamic simulation of bubble columns: Part i. detailed numerical simulations. *Chem. Eng. Sci.*, 45:2273–2284, 1999.

G. Sridhar and J. Katz. Drag and lift forces on microscopic bubbles entrained by a vortex. *J. Physics of Fluids*, 7(2):389–399, 1995.

G. Sridhar and J. Katz. Effect of entrained bubbles on the structure of vortex ring. *J. Fluid Mech.*, 397:171–202, 1999.

K. Sugiyama, S. Takagi, and Y. Matsumoto. Three-dimensional numerical analysis of bubbly flow around a circular cylinder. *JSME Int. J. Series B Fluids and Thermal Eng.*, 44(3):319–327, 2000.

K. Sugiyama, S. Takagi, and Y. Matsumoto. Three-dimensional numerical analysis of bubbly flow around a circular cylinder. *Int. J. Series B Fluids and Thermal Engineering*, 44(3):319–327, 2001.

D. Sumner, S. J. Price, and M. P. Paig Doussis. Tandem cylinders in impulsively started flow. *J. Fluids and Structures*, 13(7–8):955–965, 1999.

C. Swan and A. Moros. The hydrodynamics of a subsea blowout. *Appl. Ocean*, 15(5): 269–280, 1993.

M. V. Tabi, S. A. Roy, and J. B.Joshi. CFD simulation of bubble columnan analysis of interphase forces and turbulence models. *J. Chem. Eng.*, 139(3):589–614, 2008.

M. V. Tabib, S. A. Roy, and J. B. Joshi. CFD simulation of bubble column-an analysis of interphase forces and turbulence models. *J. Chemical Eng.*, 139(3):589–614, 2008.

Y. Tanida, A. Okajima, and Y. Watanabe. Stability of a circular cylinder oscillating in uniform flow or in a wake. *J. Fluid Mech.*, 61(4):769–784, 1973.

D. G. Thomas and K. A. Kraus. Interaction of vortex streets. *J. Appl. Phys.*, 35:3458–3459, 1964.

A. Tomiyama, G. P. Celata, S. Hosokawa, and S. Yoshida. Terminal velocity of single bubbles in surface tension force dominant regime. *Int. J. Multiphase Flow*, 28(9):1497–1519, 2002.

R. Torvik and H. Svendsen. Modelling of slurry reactors. a fundamental approach. *Chem. Eng. Sci.*, 45:2325–2332, 1990.

A. A. Troshko and Y. A. Hassan. A two-equation turbulence model of turbulent bubbly flows. *Int. J. Multiphase Flow*, 27(11):1965–2000, 2001.

T. Uchiyama. Numerical prediction of added mass and damping for a cylinder oscillating in confined incompressible gas-liquid two-phase mixture. *Nuclear Engineering and Design*, 217(2003):68–78, 2003a.

T. Uchiyama. Numerical study on the bubbly flow around a hydrofoil in pitching and heaving motions. *J. Mechanical Eng. Sci.*, 222(1):811–820, 2003b.

T. Uchiyama. Three-dimensional vortex simulation of bubble dispersion in excited round jet. *Chem. Eng. Sci.*, 59(7):1403–1413, 2004.

T. Uchiyama. Numerical simulation of particle-laden gas flow by vortex in cell method. *Powder Technology*, 235:376–385, 2013.

T. Uchiyama and T. Degawa. Vortex simulation of the bubbly flow around a hydrofoil. *Int. J. Rotating Machinery*, Article ID 72697:9 pages, 2007.

T. Uchiyama and T. Degawa. Numerical simulation of plane bubble plume by vortex method. *J. Mechanical Eng. Sci.*, 222(7):1193–1201, 2008.

T. Uchiyama and Y. Ishiguro. Experimental study of flow around a circular cylinder inside a bubble plume. *Advances in Chemical Eng. and Sci.*, 6(3):269–280, 2016.

T. Uchiyama and S. Kusamichi. Interaction of bubbles with vortex ring launched into bubble plume. *Advances in Chemical Eng. and Sci.*, 3(4):207–217, 2013.

T. Uchiyama and S. Matsumura. Three-dimensional vortex method for the simulation of bubbly flow. *J. Fluids Eng.*, 132(10):101402–101410, 2010.

T. Uchiyama and M. Naruse. Vortex simulation of slit nozzle gas-particle two-phase jet. *Powder Technology*, 131(2–3):156–165, 2003.

T. Uchiyama and S. Shimada. Numerical simulation of the interactions between a vortex pair and solid particles near a wall. *Powder Technology*, 257:55–67, 2014.

T. Uchiyama and H. Yagami. Numerical analysis of gas-particle two-phase wake flow by vortex method. *Powder Technology*, 149:112–120, 2005.

T. Uchiyama and Y. Yoshii. Numerical study of the entrainment and transport of gas bubbles by a vortex ring. *J. Chem. Eng. Process Technol.*, 6(4):1000245–1000253, 2015a.

T. Uchiyama and Y. Yoshii. Numerical simulation of bubbly flow by vortex in cell method. *Procedia IUTAM*, 18:138–147, 2015b.

T. Uchiyama, M. Kobayashi, S. Iio, and T. Ikeda. Direct numerical simulation of a jet issuing from rectangular nozzle by the vortex in cell method. *Open J. Fluid Dynamics*, 3(4):321–330, 2013.

T. Uchiyama, H. Hamada, and T. Degawa. Numerical simulation of rotating turbulent channel flow by vortex in cell method. *The Open Transport Phenomena Journal*, 5: 30–41, 2014a.

T. Uchiyama, Y. Yoshii, and H. Hamada. Direct numerical simulation of a turbulent channel flow by an improved vortex in cell method. *Int. J. Numerical Methods for Heat and Fluid Flow*, 24(1):103–123, 2014b.

T. Uchiyama, Y. Yoshii, B. Chen, and Z. Wang. Numerical simulation of bubbly flow by an improved vortex in cell method. *Advances and Applications in Fluid Mechanics*, 17 (1):91–114, 2015.

A. Vakil and S. I. Green. Numerical study of two-dimensional circular cylinders in tandem at moderate reynolds numbers. *J. Fluids Eng.*, 135(7):071204–071213, 2013.

B. Wang and S. A. Socolofsky. On the bubble rise velocity of a continually released bubble chain in still water and with crossflow. *Phys. Fluids*, 27(10):103301 (20 pages), 2015.

Z. Wang, T. Uchiyama, and B. Chen. Numerical simulation of the interaction between vortex ring and bubble plume. *Applied Mathematical Modelling*, 37(24):10007–10026, 2013.

A. Weigand and M. Gharib. On the evolution of laminar vortex rings. *J. Experiments in Fluids*, 22:447–457, 2007.

G. Winckelmens, R. Cocle, L. Dufresne, and R. Capart. Vortex methods and their application to trailing vortex simulations. *Comptes Rendus Physique*, 6(4–5):467–486, 2005.

A. K. Wong and J. A. Reizes. An effective vorticity-vector potential formulation for the numerical solution of three-dimensional duct flow problems. *J. Comput. Phys.*, 55(1): 98–114, 1984.

C. J. Xu and Y. M. Lin. A numerical comparison of outflow boundary conditions for spectral element simulations of incompressible flows. *Commun. Comput. Phys.*, 2(3): 477–500, 2007.

H. Yagami and T. Uchiyama. Numerical simulation of plane mixing layer by three-dimensional vortex method. *Int. J. Turbo and Jet Engines*, 49(4):93–101, 2007.

H. Yagami and T. Uchiyama. Numerical simulation for the transport of solid particles with a vortex ring. *Adv. Powder Technol.*, 22(1):115–123, 2011.

Y. Yanagida, S. Kawato, H. Noma, A. Tomono, and N. Tetsutani. Projection-based olfactory display with nose tracking. *IEEE Virtual Reality*, pp. 43–50, 2004.

X. Yang, N. H. Thomas, L. J. Guo, and Y. Hou. Two-way coupled bubble laden mixing layer. *Chem. Eng. Sci.*, 57(4):555–564, 2002.

M. Yokosawa, Y. Kozawa, A. Inoue, and S. Aoki. Studies on two-phase cross flow. part ii: Transition reynolds number and drag coefficient. part ii: Transition reynolds number and drag coefficient. *Int. J. Multiphase Flow*, 12(2):169–184, 1986.

T. Yoshida, T. Watanabe, and T. Ikeda. Numerical study on the convective velocity of the sommerfeld radiation condition. *Transactions of JSCES*, 2003(20030017):8 pages, 2003.

M. M. Zdravkovich. The effects of interference between circular cylinders in cross flow review paper. *J. of Fluids and Structures*, 1(2):239–261, 1987.